Friction modeling on multiple scales for Deep drawing processes

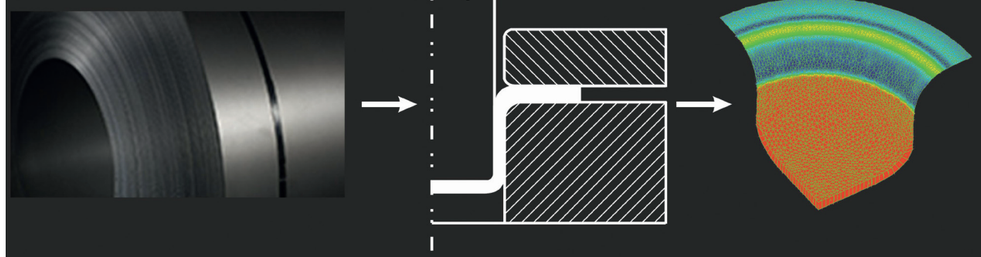

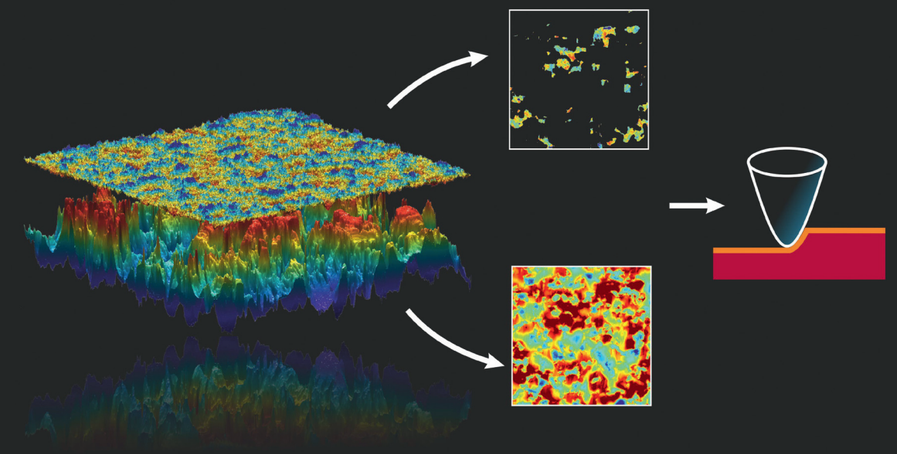

Dinesh Kumar Karupannasamy

M2i Materials innovation institute

TATA STEEL

ISBN: 978-94-91909-01-6

Friction modeling on multiple scales for deep drawing processes - D.K. Karupannasamy

FRICTION MODELING
ON
MULTIPLE SCALES
FOR
DEEP DRAWING PROCESSES

Dinesh Kumar Karupannasamy

This research was carried out under project number MC 1.07289 in the framework of the Research Program of the Materials innovation institute (M2i) in The Netherlands (www.m2i.nl).

De promotiecommissie is als volgt opgesteld:

prof.dr. G.P.M.R. Dewulf	Universiteit Twente	Voorzitter en secretaris
prof.dr.ir. D.J. Schipper	Universiteit Twente	promotor
dr.ir. M.B. de Rooij	Universiteit Twente	assistent promotor
prof. dr. ir. J.E. ten Elshof	Universiteit Twente	
prof. dr. ir. A.H. van den Boogaard	Universiteit Twente	
prof. dr. ir. P. De Baets	Universiteit Gent	
prof. dr. ir. R. Akkerman	Universiteit Twente	

Karupannasamy, Dinesh Kumar
Friction modeling on multiple scales for deep drawing processes
Ph.D. Thesis, University of Twente, Enschede, The Netherlands
November 2013

ISBN: 978-94-91909-01-6

Keywords: tribology, friction modeling, deep drawing processes, multi-asperity contact, boundary lubrication, mixed lubrication, asperity flattening and ploughing.

Printed by Ipskamp Drukkers

Cover design by Dinesh Kumar Karupannasamy.

FRICTION MODELING ON MULTIPLE SCALES FOR DEEP DRAWING PROCESSES

PROEFSCHRIFT

ter verkrijging van
de graad van doctor aan de Universiteit Twente,
op gezag van de rector magnificus,
prof.dr. H. Brinksma,
volgens besluit van het College voor Promoties
in het openbaar te verdedigen
op woensdag 13 november 2013 om 14.45 uur

door

Dinesh Kumar Karupannasamy

geboren op 18 october 1982
te Erode, India

Dit proefschrift is goedgekeurd door:
de promotor: prof.dr.ir. D.J. Schipper
de assistent promotor: dr.ir. M.B. de Rooij

TABLE OF CONTENTS

Samenvatting v

Summary vii

Nomenclature ix

Chapter 1 Introduction 1

1.1 Background 1
1.2 Friction 1
1.3 Deep drawing processes in automotive industry 2
1.4 Surface roughness 3
1.5 Contact between rough surfaces 4
1.6 Tribological system in deep drawing processes 4
1.7 Influence of friction in deep drawing FE simulations 5
1.8 Objectives of the research 6
1.9 Overview of the thesis 6

Chapter 2 Contact and friction in deep drawing processes 7

2.1 Introduction 7
2.2 Contact in deep drawing processes 7
2.3 Friction in deep drawing processes 8
2.3.1 Adhesion 9
2.3.2 Ploughing 9
2.3.3 Shearing of lubricant film 10
2.3.4 Influence of asperity deformation process 10
2.4 Contact model 11
2.4.1 Asperity flattening due to normal loading 11
2.4.2 Asperity flattening due to bulk deformation 13
2.5 Lubrication in deep drawing processes 15
2.5.1 Boundary layer lubrication 16
2.5.2 Hydrodynamic lubrication 18
2.5.3 Mixed lubrication 18
2.6 Ploughing model 22
2.7 Surface Roughening 23
2.7.1 Overview 23
2.7.2 Surface roughening model 24
2.8 Overview of friction modelling in deep drawing processes 27
2.8.1 Asperity flattening 27
2.8.2 Hydrodynamic lubrication 27

2.8.3 Calculation of the coefficient of friction 27
2.9 Analysis of surface properties for DC06 sheet material and deep drawing tool surface 28
2.10 Summary 30

Chapter 3 Determination of the boundary layer shear strength 31

3.1 Introduction 31
3.2 Boundary layer lubrication models 31
3.3 Influence of interfacial friction factor 33
3.4 Experimental determination of friction factor for the BL model 34
3.5 Influence of real contact area on interfacial shear strength 39
3.6 Summary 43

Chapter 4 Modelling mixed lubrication for deep drawing processes 45

4.1 Introduction 45
4.2 Asperity deformation model 45
4.2.1 Asperity flattening due to normal loading 46
4.2.2 Asperity flattening due to bulk deformation 47
4.3 Mixed lubrication modelling 49
4.4 Friction calculation 52
4.5 Results and Discussion 53
4.6 Lubricant starvation 59
4.7 Surface roughness effects on lubricant flow using flow factors 61
4.8 Summary 63

Chapter 5 Deterministic contact and friction model – fully plastic deformation mode 65

5.1 Introduction 65
5.2 Contact of rough surfaces 66
5.3 Asperity characterization process 67
5.4 Deterministic approach 69
5.5 Deterministic flattening model 71
5.6 Deterministic ploughing model 73
5.7 Surface roughness parameters 75
5.8 Friction model 78
5.9 Friction calculations with asperity deformation and ploughing model 78
5.10 Influence of interfacial friction factor 82
5.11 Summary 83

Chapter 6 Loading / reloading of contacting surfaces 85

6.1 Introduction 85
6.2 Elastic-plastic single asperity contact model 86
6.2.1 Elastic contact 86
6.2.2 Full plastic contact 88
6.2.3 Elastic-plastic contact 89
6.3 Unloading of single asperity contact 90
6.3.1 Elastic unloading 91

6.3.2 Elastic-plastic unloading 92
6.3.3 Fully plastic unloading 92
6.4 Reloading of single asperity contact 92
6.5 Reloading of surfaces 95
6.6 Elastic plastic ploughing contact model 98
6.7 Contact analysis of rough surfaces 99
6.8 Interfacial friction factor 101
6.9 Evolution of friction conditions during reloading of surfaces 102
6.10 Summary 103

Chapter 7 Results and validation of the friction model 105

7.1 Introduction 105
7.2 Experimental Setup 105
7.2.1 Sheet material specimen 106
7.2.2 Tool Specimen 106
7.2.3 Testing procedure 107
7.3 Results 107
7.4 Application of the friction model to a cup drawing process 108
7.4.1 Comparison of statistical and deterministic model 108
7.4.2 Influence of hydrodynamic lubrication 110
7.5 Summary 112

Chapter 8 Conclusions and recommendations 113

8.1 Introduction 113
8.2 Overview of the developed model 113
8.3 Conclusions 113
8.4 Recommendations 115

Appendices 119

Appendix A 119
Appendix B 121
Appendix C 123
Appendix D 127
Appendix E 129
Appendix F 133

References 135

SAMENVATTING

Het dieptrekproces is een van de meest gebruikte productietechnieken in de automobielindustrie vanwege het vermogen om complexe vormen te produceren uit plaatmateriaal, waarbij vaak gebruik wordt gemaakt van smeermiddelen om het omvormproces goed te laten verlopen. Eindige Elementen simulaties van omvormprocessen worden in de ontwerpfase van een product vaak gebruikt om de vervormbaarheid van het product en de terugvering van het product na het omvormen te voorspellen. Verder kunnen analyses uitgevoerd worden naar lokale verdunning / verdikking van plaatmateriaal en het falen van de plaat tijdens het omvormen. De prestaties van FEM simulaties zijn in sterke mate afhankelijk van de nauwkeurigheid van de gebruikte numerieke technieken, maar ook van de materiaalmodellen, contact en wrijving condities. In de afgelopen decennia hebben er met name ontwikkelingen plaatsgevonden op het gebied van numerieke technieken, materiaal en contact algoritmen. Echter, bij het definiëren van de wrijving wordt nog veelvuldig gebruik gemaakt van een constante wrijvingscoëfficiënt op basis van Coulombse wrijving. In werkelijkheid is de wrijvingscoëfficiënt echter afhankelijk van de aard van de oppervlakken en de materiaaleigenschappen, maar ook van de operationele- en omgevingsomstandigheden.

In dit onderzoek is een wrijvingsmodel ontwikkeld. Dit model kan worden gekoppeld aan FEM simulaties en worden gebruikt om de lokale wrijvingscoëfficiënt in een dieptrekproces te voorspellen. De relevante wrijvingsmechanismen op de ruwheidsschaal welke meegenomen zijn in het model, zijn het afschuiven van grenslagen, het ploegeffect en het afschuiven van de smeerfilm in het contact. Daarnaast is er een contactmodel ontwikkeld om het plastisch vervormen van het plaatoppervlak beschrijven op basis van een gegeven oppervlakte topografie, de belasting op de micro – schaal en de bulkrek. In de contactmodellen wordt de ruwheid van zowel het plaatmateriaal als de ruwheid van het oppervlak van het gereedschap meegenomen. De ruwheid van het plaatmateriaal is belangrijk voor het bepalen van de gedeformeerde geometrie van de plaat. De ruwheid van het gereedschap is belangrijk voor het bepalen van het ploegeffect. Verder is er een smeringsmodel ontwikkeld om de hydrodynamische effecten in de smeerfilm tussen de oppervlakken te beschrijven. Hierbij wordt rekening gehouden met de vervorming van het oppervlak van het plaatmateriaal en de operationele condities zoals de glijsnelheid. Het effect van het type oppervlakteruwheid en de hoeveelheid smeermiddel die is aangebracht op het oppervlak wordt ook meegenomen in het model. Verder is er een deterministische benadering voor de karakterisering van de micro-contacten gebruikt. Deze benadering is beter dan de meer klassieke statistische methoden, omdat het in staat is de geometrie van deze microcontacten nauwkeuriger en gedetailleerder te beschrijven. Het contactmodel is verder uitgebreid met elastoplastisch contactgedrag om elastische terugvering van de ruwheidstoppen op plaatoppervlak te modelleren. Dit effect treedt op als het plaatmateriaal onderhevig is aan een afnemende normaalbelasting. Daarnaast zijn er experimenten

uitgevoerd om de afschuifsterkte van de gevormde grenslagen te bepalen. Uit de experimenten blijkt dat de afschuifsterkte van grenslagen bij benadering constant is als het juiste contactoppervlak wordt gebruikt in de analyse van de experimentele data.
In een dieptrekproces zal de wrijvingscoëfficiënt afnemen als de operationele condities het toelaten dat er hydrodynamische drukopbouw optreedt en als de aangebrachte hoeveelheid smeermiddel hiervoor voldoende is. De resultaten van het model laten zien dat de wrijvingscoëfficiënt afneemt als de contactdruk toeneemt, hetgeen in overeenstemming is met de uitgevoerde experimenten. Verder laat het ontwikkelde model zien dat de wrijvingscoëfficiënt afhankelijk is van de oppervlakteruwheid, een ruwheidsbandbreedteparameter en de oriëntatie van de ruwheid ten opzichte van de snelheidsvector. De wrijvingscoëfficiënt is hoog voor ruwe oppervlakken, oppervlakken met een lage waarde van de bandbreedteparameter en een transversale ruwheid. De wrijvingscoëfficiënt is laag voor oppervlakken met een lage ruwheid, een hoge waarde van de bandbreedteparameter en een longitudinale oriëntatie van de oppervlakteruwheid. Het wrijvingsmodel is gevalideerd met behulp van experimenten die zijn uitgevoerd op een roterende wrijvingstester.
De resultaten van het wrijvingsmodel vertonen een goede overeenkomst met de experimentele resultaten. Tenslotte is de toepasbaarheid van de wrijvingsmodel aangetoond met een FEM -simulatie van een rotatiesymmetrisch product. Deze simulatie laat het verwachte verloop van de wrijvingscoëfficiënt gedurende het dieptrekproces zien.

SUMMARY

A deep drawing process is one of the widely used manufacturing techniques in the automotive industry because of its capability to produce complex shapes with sheet material, often performed using lubricants to ease the forming. Finite Element Methods (FEM) are popularly used at the design stage to predict the formability of the product, the spring-back of the sheet metal product after forming, local thinning/thickening of sheet material and failure of the sheet metal during forming. The performance of the FEM simulations relies on the accuracy of the numerical techniques, material models, contact and friction conditions. Over the past decades, FEM has been largely developed on the aspects of numerical techniques, material and contact algorithms. The coefficient of friction used in the contact formulations is often still the Coulomb friction model, i.e. constant coefficient of friction. The coefficient of friction, however, is generally dependent on the nature of surfaces, material properties as well as the operational and environmental conditions.

A friction model has been developed in this research work. This model can be coupled with the FEM simulations in predicting the local coefficient of friction for a deep drawing process. The basic friction mechanisms at the asperity scale taken into account in the model are shearing of the boundary layers, ploughing and shearing of the lubricant film. A contact model has been developed to describe the fully plastic deformation of the surface from a given surface topography, the load at the micro-scale as well as the uniaxial bulk strain. The contact models include the roughness of both the sheet material (for surface deformation) and tool surfaces (for ploughing). A lubrication model has been developed to describe the hydrodynamic flow of the lubricant between the surfaces, taking into account the surface deformation of the sheet as well as the operational conditions like the sliding velocity. The effect of surface lay and lubricant amount applied on the surface is also considered in the model. Further, a deterministic approach for the characterisation of the micro-contacts has been used. This approach is better than traditional statistical methods in terms of geometrical description. The contact model has been further extended to elastic-plastic contact conditions to account for the elastic recovery of the asperities if the sheet surface is subjected to unloading. Experiments have also been carried out to study the shear strength of the boundary layers formed due to the lubricant. It is shown that the shear strength of boundary layers is almost constant if the appropriate contact area is used in the analysis of the experimental data.

The coefficient of friction is shown to reduce during the deep drawing processes due to the lubricant pressure generation if the operation conditions and the applied lubricant amount favour hydrodynamic effects. The model shows that the coefficient of friction decreases as the contact pressure increases, which is in accordance with the experiments. The contact model shows that the coefficient of friction is dependent on the surface roughness, bandwidth parameter and surface lay. The coefficient of friction is high for rough, low

bandwidth and transversal anisotropic surfaces. The coefficient of friction is low for smooth, high bandwidth and longitudinal anisotropic surfaces. The friction model has been subjected to a validation process with a rotational friction tester.
The results of the friction model shows good comparison with the experimental results. The applicability of the developed friction model in a FEM simulation has been demonstrated with a cup drawing FEM simulation which shows the expected evolution of friction conditions during the progression of a deep drawing process.

NOMENCLATURE

List of Roman Symbols

Symbols	Description	Units
A	Contact area of the asperity	[m^2]
A_{nom}	Nominal contact area	[m^2]
A_{real}	Real contact area	[m^2]
B	Parameter in Challen and Oxley's model	[-]
C	Hardening parameter in Nadai's model	[Pa]
C_A	Critical contact area ratio at the onset of plasticity	[-]
D_P	Degree of penetration of the asperity	[-]
E	Asperity non dimensional strain rate	[-]
$E_{1,2}$	Elastic modulus of the contacting body 1 and 2	[Pa]
E^*	Combined elastic modulus of the contacting bodies	[Pa]
$E(m)$	Elliptic integral of the second kind for the elliptic paraboloid asperity	[-]
F_N	Applied normal force	[N]
F_W	Frictional force	[N]
H	Hardness of the sheet material	[Pa]
H_{eff}	Effective hardness of the sheet material	[Pa]
H_{lub}	Non-dimensional lubricant film thickness, h_{lub}/S_q	[-]
H^c_{lub}	Non-dimensional lubricant threshold film thickness	[-]
K	Kurtosis of the surface	[-]
H_{ind}	Indentation hardness	[Pa]
K_v	Contact pressure factor for the hardness of the deforming material	[-]
$K(m)$	Elliptic integral of the first kind for the elliptic paraboloid asperity	[-]
L	Non-dimensional lubrication number	[-]
M	Schmid factor	[-]
P_m	Mean contact pressure carried by an asperity	[Pa]
P_{max}	Maximum contact pressure carried by an asperity	[Pa]
P_{nom}	Nominal contact pressure	[Pa]
P_{real}	Real contact pressure	[Pa]
Q	Flow rate of the lubricant	[m^3s^{-1}]
R	Effective radius of the paraboloid/summit	[m]
R_a	Arthimetic average roughness of surface	[m]
R_{avg}	Average effective radius of the summits	[m]

R_{ul}	Effective radius of the paraboloid/summit after unloading	[m]
$R_{x,y}$	Radius of the elliptical paraboloid in major and minor axis direction	[m]
S_{κ}	Skewness of the surface roughness	[-]
S_q	Root mean square value roughness of surface	[m]
$S_{x,y}$	Slope of the asperity in x and y directions	[-]
$U_{1,2}$	Velocity of contacting bodies	[ms^{-1}]
V	Volume of an asperity	[m^3]
V_{valley}	Volume of the valleys in the surface	[m^3]
W	Work done in asperity deformation processes	[Nm]
a	Semi-major radius of ellipse	[m]
a_a	Half width of the asperity	[m]
$a_{contact}$	Contact radius of the asperity	[m]
b	Semi-minor radius of ellipse	[m]
d	Asperity flattening distance	[m]
e	Eccentricity of the elliptical base of the asperity	[-]
$f_{1,2}$	Constants used in asperity deformation model	[-]
f_{BL}	Friction factor for boundary layers	[-]
f_d	Boundary layer degradation factor	[-]
f_{hk}	Interfacial friction factor	[-]
g_s	Grain size	[m]
h	Separation of the surface	[m]
h_{lub}	Fluid film thickness	[m]
k	Shear strength of the deforming material	[Pa]
l	Contact length in the blank holder region	[m]
l_a	Asperity half length	[m]
l_g	Grain spacing length	[m]
m	Elliptic integral parameter, $(1-\kappa^2)$	[-]
$m_{0,2,4}$	Power spectral moments of the surface	[m^2],[-],[m^{-2}]
n	Hardening parameter in Nadai'model	[-]
$p_{x,y}$	Pixel size in x and y direction	[m]
q	Frictional heat quantity	[W]
s	Summit height of the tool asperity	[m]
u	Rise of asperities in the valley	[m]
$v_{a,b}$	Flattening and rising velocity of asperities	[ms^{-1}]
z	Asperity height	[m]

List of Greek Symbols

Symbol	Description	Units
α	Fractional contact area	[-]
β	Attack angle of the asperity	[°]
γ	Surface lay parameter	[-]
α'	Non-dimensional semi axis of contact ellipse in major direction	[-]

β'	Non-dimensional semi axis of contact ellipse in minor direction	[-]
γ'	Non-dimensional interference of paraboloid	[-]
γ_{lay}	Surface lay parameter (from autocorrelation length)	[-]
δ	Dimensionless interference	[-]
ε	Applied strain	[-]
ε_0	Initial strain	[-]
$\dot{\varepsilon}$	Strain rate	[s^{-1}]
η	Asperity persistence parameter	[-]
η_{lub}	Lubricant viscosity	[Pa·s]
θ	Asperity angle	[°]
θ_g	Grain orientation	[°]
κ	Ellipticity ratio of the asperity	[-]
κ_x	Curvature of the asperity in semi-major direction	[m^{-1}]
κ_y	Curvature of the asperity in semi-minor direction	[m^{-1}]
λ	Asperity curvature ratio	[-]
μ	Coefficient of friction	[-]
$\nu_{1,2}$	Poisson ratio of the contacting bodies 1 and 2	[-]
ξ	Expression used in the normal loading process	[-]
ρ	Asperity density	[m^{-2}]
ρ_{lub}	Density of lubricant	[Ns^2m^{-3}]
σ_κ	Standard deviation of the surface curvatures	[m^{-1}]
σ_s	Standard deviation of the surface slopes	[-]
σ_y	Yield strength of the sheet material material	[Pa]
σ_{yy}	Principal stress in y-direction	[m]
σ_z	Standard deviation of the surface heights	[m]
ς	Shape factor of the asperity	[-]
τ	Shear strength	[Pa]
τ_{crit}	Critical shear strength at grain boundary	[Pa]
τ_g	Shear strength at grain boundary	[Pa]
ϕ	Probability density function of surface	[-]
ϕ_s	Flow factor for velocity driven flow	[-]
ϕ_x	Flow factor for pressure driven flow	[-]
φ	Orientation of the asperity with respect to sliding direction	[deg]
χ	Expression used in the Westeneng's model [18] for normal loading process	[-]
ψ	Bandwidth parameter of the surface	[-]
ω	Interference of asperity	[m]
ω_1	Interference of asperity at the onset of plasticity	[m]
ω_2	Interference of asperity at the full plastic deformation	[m]

ω_{ul}	Interference of asperity after unloading	[m]

Subscripts

BL	Boundary lubrication
applied	Applied work on the asperity
asp	Asperity
e	Elastic deformation mode
ep	Elastic-plastic deformation mode
p	Plastic deformation mode
flat	Flattening of asperity
l	Normal loading process for asperity flattening
real	Real contact area of the surface
rise	Rising of asperities
nom	Nominal area of the surface
p	Plastic deformation mode
s	Stretching process for asperity flattening
t	tool
ul	Unloading of asperity
wp	Workpiece surface

Superscripts

lub	Lubricant contacting part
sol	Solid contacting part
trans	Transition points for elastic and plastic deformation modes

Abbrevations

ACL	Auto correlation length
BCC	Body centered cubic
BEM	Boundary element method
BL	Boundary lubrication
EBT	Electron beam texturing
EDT	Electrical discharge texturing
EHL	Elasto-hydrodynamic lubrication
FCC	Face centered cubic
FE	Finite element
FFT	Fast fourier transform
HCP	Hexagonal close packing
HL	Hydrodynamic lubrication
LT	Laser texturing
ML	Mixed lubrication
PHL	Plasto-hydrodynamic lubrication
RFT	Rotational friction tester
SBT	Shot blast texturing

SMF	Sheet metal forming

Chapter 1
INTRODUCTION

1.1 Background

The popularity of numerical simulations to predict product/process performance is gaining interests in automotive industries. Sheet metal forming (SMF) is one of the widely used processes in automotive industries to manufacture body parts from cold-rolled sheet material as shown in Figure 1.1 (a). A typical deep drawn product, an unfinished body side of Ford Mondeo, is shown in Figure 1.1 (b). In the manufacturing sector, the understanding of the process is vital for increasing the production efficiency, reducing the wastage of material and reducing the time to market. Product design is often combined with the feasibility of manufacturing. This technique is known as "Design for manufacturing" and it is constantly evolving. Nowadays, Finite Element (FE) methods are widely used to predict the manufacturability of the product at the design stage itself. In sheet metal forming simulations, the predictability is determined by material models and contact algorithms. In the past decade, a lot of attention has been paid to the material models but the friction models have not been developed. However, the friction conditions are affected by the surface related micro-mechanisms [1]-[4]. In this chapter, a brief overview is given of friction conditions and their influence in forming processes.

(a) (b)

Figure 1.1: (a) Skin pass cold-rolling mill with EDT surface texturing (Source - Tata Steel website) and (b) Side panel of Ford Mondeo car (Source - Corus Emotion, issue 14, 2008).

1.2 Friction

If two solid bodies are in a direct or indirect surface contact and sliding relative to one another, there is always a resistance to motion called friction. Friction is influenced by the

environmental and operational conditions of the interacting surfaces, according to Czichos [5]. The environmental conditions can be affected by the presence of humidity and gaseous substances. The operational conditions are the contact load, temperature and relative sliding velocity. Friction is typically classified into two types – static and dynamic friction. Static friction is the friction at which the body is at a state of rest. Static friction reaches its maximum when the body starts to move. Static friction is useful in restricting the motion between objects, for example fasteners and jackscrews. Dynamic friction is the friction at which the bodies are in relative motion. Depending on the nature of motion, it can be subdivided into rolling friction (e.g. metal rolling process, bearings) and sliding friction (e.g. sheet metal forming processes, internal combustion engine).

1.3 Deep drawing processes in automotive industry

A SMF process has many variants depending on the process nature. The conventional SMF processes like bending, rolling, incremental forming, extrusion and deep drawing are widely used in automotive industries. Deep drawing process is one of the commonly used methods to form the required product shape by subjecting the sheet metal to plastic deformation. Deep drawing process is known for its capability to produce complex shapes with a higher production rate than the other manufacturing processes.
In principle, the deep drawing operation uses tool and die to transform the sheet metal in to the required functional shape. The tool and die replicates the final or intermediate shape of the product. To view a deep drawing process in a simple manner, a cup drawing process is shown in Figure 1.2. In a deep drawing process, a flat sheet material which is usually lubricated with oil or a pre-coated sheet material is placed on the die. A blank holder holds the sheet firmly with a preset holding pressure to avoid wrinkling and control the slipping of the sheet over the die. A tool (which has complex geometric details) and a punch come into contact with the blank and deform the blank in the die cavity. The punch force should be just enough to deform the sheet.

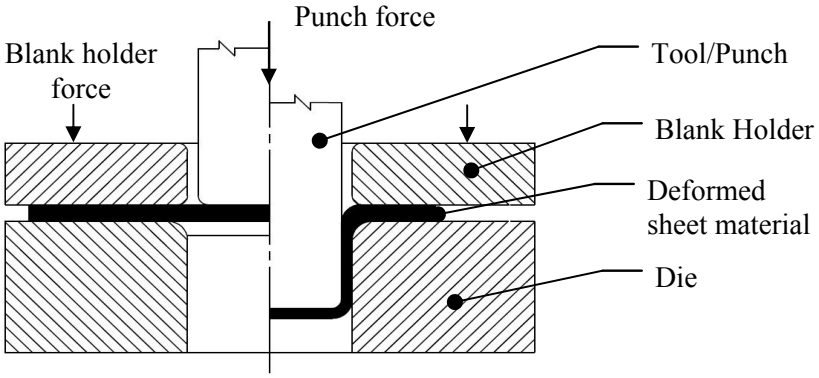

Figure 1.2: Cup drawing process illustration.

Deep drawing for complex geometries and large height-diameter ratio components is generally done in multiple steps. The greater the depth, the higher the number of reduction steps required. Deep drawing may also be accomplished with fewer reductions by heating the sheet material. The most commonly used sheet materials for automotive applications are steel and aluminium because of their natural availability, mechanical properties and cost effectiveness. Typically cold-rolled steel is used for body parts because of its structural strength and durability. Cold-rolled steel has good ductility which can be easily formed into the desired shape. Zinc-coatings on the steel are also used in the automotive parts for the protection against corrosion. The tool is subjected to repeated contacts with the sheet material during forming processes. Generally, tool is made of heat treated alloy steel and may be coated with protective layers to prolong its useful life. The tool has better surface properties than the sheet material.

1.4 Surface roughness

The surface topography at the micro level (μm) has surface irregularities known as asperities or summits and valleys. The surface irregularities continue to occur even when the magnification level increases. The surface irregularities can occur in different patterns which are transferred from the rolls during the sheet metal manufacturing process. The surface pattern influences the deep drawing process performance. The mill-finished sheet material typically has rolling direction marks. A specific texture can be produced by using textured rolls. Different types of roll texturing process are shot blasting texturing (SBT), laser texturing (LT), electron beam texturing (EBT) and electrical discharge texturing (EDT). SBT steel sheets have the highest surface roughness and rolling direction marks and are strongly anisotropic with a surface roughness in the order of 1.8~2.3 μm. EDT steel sheets have an isotropic surface with a surface roughness in the order of 1.3 μm. LT and EBT steel sheets have cavities or annular grooves to improve the lubricating properties during the deep drawing operation and the surface roughness is in the same order of magnitude as that of EDT. EBT has greater flexibility and better repeatability of the surface textures than the other methods. The surface images of different process are shown in Figure 1.3. Press tools also use these texturing methods and are coated with wear resistant materials.

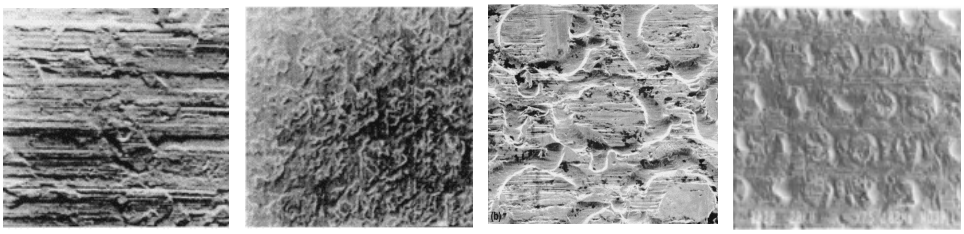

(a) (b) (c) (d)

Figure 1.3: Surface texturing of sheet materials (a) SBT, (b) EDT, (c) EBT and (d) LT.

1.5 Contact between rough surfaces

When two nominally flat rough surfaces are brought into contact with each other, contact occurs only at the peak of surface features known as asperities. The real contact area, A_{real}, occurring at the surface is generally less than the nominal contact area, A_{nom}, as shown in Figure 1.4. The ratio of the real contact area to the nominal contact area is known as the fractional contact area or the degree of contact, α. The development of the contact area depends on the material properties, contact load, surface roughness and presence of lubricant. The initial roughness of the surface changes due to plastification of the asperities during deformation. The asperity deformation can also be influenced by the subsurface stresses during the bulk deformation process. The asperity deformation and interaction between the asperities during the sliding motion determines the contact and friction behaviour.

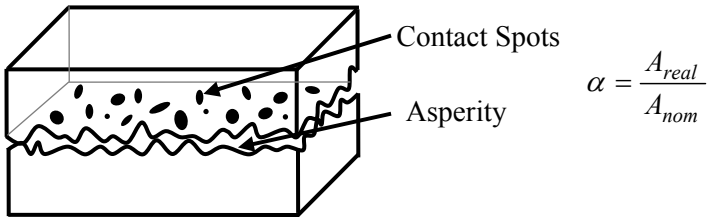

Figure 1.4: Contact between rough surfaces.

1.6 Tribological system in deep drawing processes

Tribology is the science and technology of the interacting surfaces between bodies when subjected to relative motion. The study of tribology revolves around the friction, wear and lubrication phenomena in between the contacting surfaces at macro to atomic scales. Hence the study of tribology comprises a system with interacting bodies, environment and operational/process conditions at different length scales. A tribological system in deep drawing processes consists of interacting surfaces of sheet material and tool in a lubricated environment operating under the influence of applied load and sliding velocity at room temperature conditions, as shown in Figure 1.5.

The friction occurring in deep drawing processes is a very complex phenomenon. The friction can occur due to adhesive forces, deformation (ploughing) and hydrodynamic effects in the case of lubricated contacts. Friction is influenced largely by the lubricant adhering to the surfaces, forming boundary layers which govern the adhesive force. Surface deformation processes increase the real contact area between the asperities, thereby influencing the friction. These two phenomena are vital for the friction between rough contacts. If there is a difference in the hardness of the materials in contact, the harder shears the softer material and contributes to the frictional force. If the contact is lubricated, the friction is greatly reduced due to lubricant hydrodynamic action. The influencing friction

micro-mechanisms are discussed in detail in Section 2.3. During deformation, the material can undergo different modes of deformation (i.e. elastic, elastic-plastic and plastic). In deep drawing processes, the surface is subjected to repeated contact conditions.

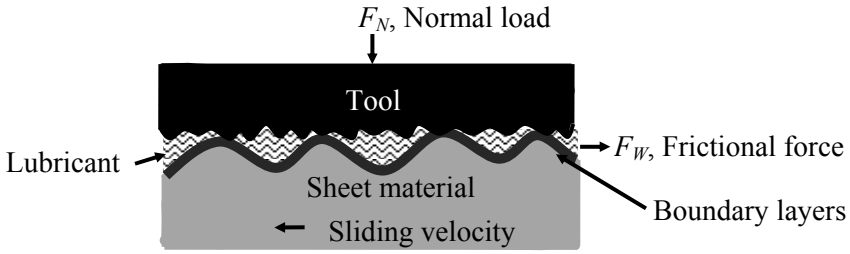

Figure 1.5: Tribological system in deep drawing processes.

To describe the friction behaviour between the surfaces in deep drawing processes, the tribological system is simplified with the following assumptions,

- The sheet material and tool surfaces are considered as uncoated surfaces. The surface coatings increase the complexity of the problem.
- Material transfer and wear of the tool surfaces occur over a considerable usage of the deep drawing tools. The surface properties of the tool will remain unchanged during a single deep drawing operation.
- Most of the forming process is done in a cold working environment. Therefore the influence of temperature on the mechanical/tribological properties is neglected. Local frictional heating will affect the tribological properties but the influence is more pronounced at high speed conditions.

1.7 Influence of friction in deep drawing FE simulations

The effect of various factors influences the final shape of the deep drawing product. The material characteristics, product geometry, die geometry, friction, blank holding and punch forces are considered to be the main factors affecting the forming process. The influence of friction is critical to the deep drawing processes. High friction in the blank holder or die rounding regions results in tearing of the sheet material which results in complete rejection of the product during forming processes. In case of low friction, wrinkling of the sheet material may occur in the flange region of the product due to excessive compressive stress or excessive flow of the material. Thinning or thickening of the sheet material denotes the onset of these defects, which are caused due to the combined effect of material, product geometry and tribological conditions. Spring-back of the sheet material after a deep drawing operation is also influenced by the friction conditions. The friction influences the punch force displacement characteristics, stresses and strains during the deep drawing operation. Hence it is important to consider the friction at the local conditions for deep drawing proceses.

1.8 Objectives of the research

The contact behaviour between the sheet material and tool is generally determined by the micro-geometrical properties of the surface as well as the mechanical properties of the materials. The relative motion between the interacting surfaces causes friction during a deep drawing operation. This in turn affects the predictability of the FE simulations. The principal objectives of the research are as follows:

- Determination of boundary layer properties of the interacting surfaces due to the presence of a lubricant.
- Development of a contact model which includes surface deformation processes and surface roughness effects.
- Development of a lubrication model under forming conditions.
- Development of a friction model incorporating the newly developed contact and lubrication model.
- Validation of the friction model under laboratory scale conditions and its application in FE simulations.

1.9 Overview of the thesis

This thesis focuses on the development of the friction model originating from asperity micro-mechanisms. A summary of the literature review on the asperity micro-mechanisms and friction modelling is presented in Chapter 2. The influence of lubricant layers on the interacting surfaces is studied by experiments in Chapter 3. The experiments are performed with the materials applicable to the deep drawing processes. In Chapter 4, a hydrodynamic lubrication model is developed to explain the effects of lubrication in deep drawing processes. The model is built based on the contact model available from the literature review. The application of the lubrication model is shown for cup drawing FE simulations. The contact model is improved to include the surface roughness effects in Chapter 5. The contact model and friction model are further improved using the mixed modes of deformation and reloading effects in repeated contact conditions, as explained in Chapter 6. The validation of the friction model is performed in Chapter 7 using standard friction testing equipment. In Chapter 8, major conclusions of the research work and recommendations for the future work are outlined.

Chapter 2
CONTACT AND FRICTION IN DEEP DRAWING PROCESSES

2.1 Introduction

In this chapter, a literature review of tribological conditions occurring in deep drawing processes related to friction modelling is presented. The review focuses the various phenomena during deep drawing operation like surface deformation, lubrication effects and roughening in the contacting regions.
In Section 2.2, the possible different contact conditions and their relevance to friction occurring between the sheet material and tool is discussed. In Section 2.3, the micro-mechanisms responsible for friction occurring at the interacting surfaces are discussed. In the following Sections 2.4 - 2.6, the friction mechanisms and the modelling approach are discussed in detail. In Section 2.7, the surface roughening mechanism occurring due to bulk deformation is discussed. A general overview of the model to calculate the coefficient of friction from the discussed friction mechanisms is presented in Section 2.8. An analysis of the surface topographies measured from the sheet material and tool surfaces are discussed in Section 2.9. The chapter concludes with a summary.

2.2 Contact in deep drawing processes

In a deep drawing process, the sheet material held by the blank holder is forced into the die cavity by the punch to form the desired product shape. The contact which occurs between the sheet material and tool material during sliding results in friction. Different contact conditions arise from the contact between the

- blank holder and sheet material,
- die and sheet material,
- punch and sheet material.

There are six regions where the contact conditions related to friction occur in a deep drawing process according to Schey [7], as shown in Figure 2.1. The regions marked as 1 and 2 are the blank holder regions where the pressure applied is usually low. The blank holder pressure is in the order of 10-50 MPa for the deep drawing process accompanied by a tangential tension due to punch forces. A circumferential compressive stress and radial tensile stresses is also experienced near the die rounding region. A high blank holding pressure will result in tearing of sheet due to high punch forces. In this region, the sheet material experiences a radial draw-in. The strains in these regions are rather small compared to the other regions. In these regions, the sliding velocity during deep drawing

operation will be in the order of 10^{-3}~10^{-1} m/s, where the sliding velocity is determined by the punch velocity. The blank holder region can operate in the Stribeck's different lubrication regimes (detailed in Section 2.5) depending on the sliding velocity of the sheet, surface roughness and lubricant viscosity. Apart from the material parameters and operational conditions, the product geometry influences the transition in the lubrication regimes. If the deep drawing depth is shallow, the lubrication conditions will be mostly in boundary lubrication (BL) since not much sliding takes place between sheet material and tool. When the deep drawing depth is high, the lubrication regime transits to mixed lubrication (ML) if the material and operational conditions are favourable. The hydrodynamic flow of the lubricant occurs in the valleys of the surface roughness due to the squeezing of the lubricant by the surface deformation process. In region 3, the sheet material undergoes severe bending stresses. The pressure occurring in this region is in the order of 10~100 MPa. The tensile stress caused by the punch is high and the sheet is subjected to stretching. BL, ML and ploughing mechanism prevails in this region due to high contact pressure conditions. Regions 4 (punch flank and sheet) and 5 (punch end and sheet) do not have significant impact on the friction in a deep drawing process. The real contact does not occur in these regions due to clearance between the die and punch. In region 6, the contact occurs between the punch rounding and sheet material. This region is subjected to a similar condition as in the die rounding region 3. The sheet is subjected to high pressure and stretching conditions. Regions 1, 2, 3 and 6 are of interest when studying the tribological conditions in a deep drawing process.

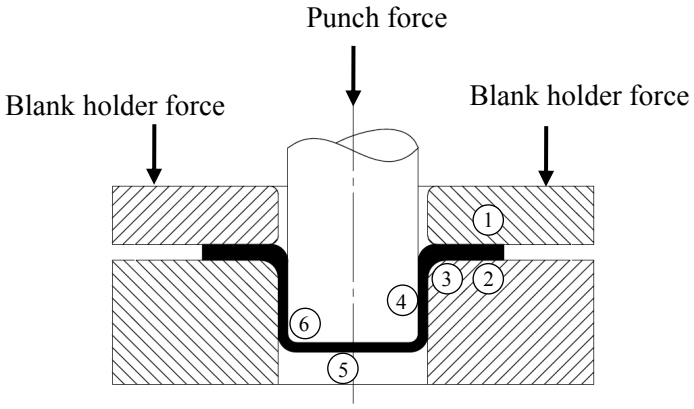

Figure 2.1: Contact conditions in a deep drawing process [7].

2.3 Friction in deep drawing processes

Surfaces are always rough and contaminated due to lubrication or environmental conditions. In deep drawing processes, the interacting surfaces differ in roughness levels and material properties. There are three important mechanisms which are responsible for friction between the interacting surfaces are adhesion, ploughing and shearing of lubricant

film, as shown in Figure 2.2. Additionally, the real contact area increases due to the applied normal forces and bulk strain in a deep drawing process which also influences the friction.

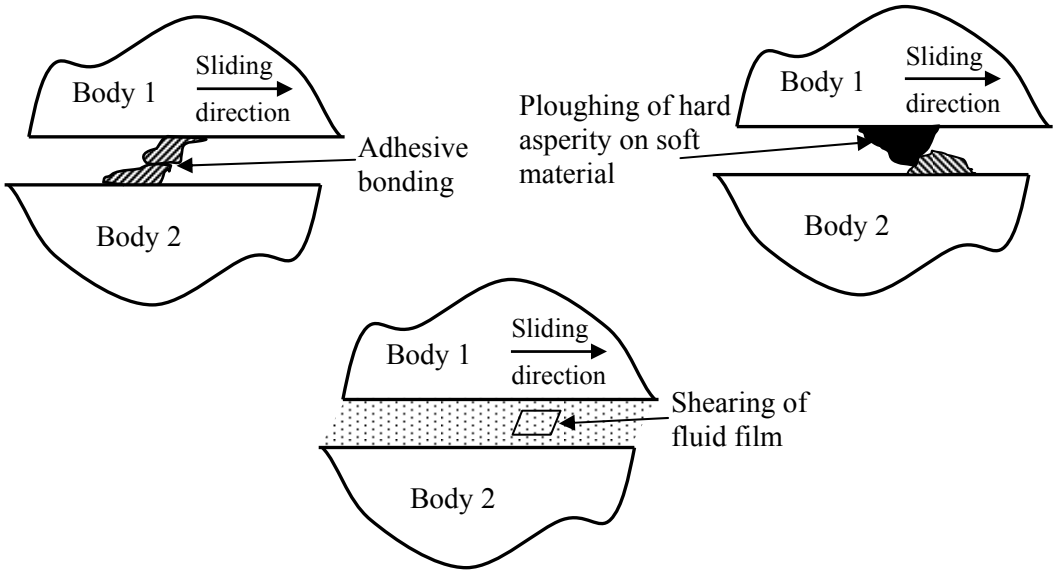

Figure 2.2: Basic friction mechanisms for the interaction between surfaces.

2.3.1 Adhesion

When two surfaces are made to contact with each other, different types of surface forces occur depending on the environment, materials, temperature and load. Bowden and Tabor [8] postulated that the junction growth occurs between metallic surfaces due to the cold welding of asperities under clean and dry conditions. Johnson et al. [9] found that there is an increased contact area for low loads under clean conditions, due to the adhesive forces between the surfaces. Adhesive friction will occur only when surfaces of metals are brought under clean and vacuum conditions. This is considered as less important in a deep drawing process. However, the shear of the boundary layers in lubricated environments (often called as adhesive friction) is considered to be important in deep drawing processes as discussed in Section 2.5.1.

2.3.2 Ploughing

Ploughing prevails in the deep drawing process due to the difference in the hardness of the contacting materials. The friction force due to ploughing is caused by energy losses on the deformation. Bowden and Tabor [8] considered that the frictional stress is due to the shearing action of the welded asperities produced from the adhesion. However, they also postulated that friction can arise due to the ploughing of hard asperities over the soft material. The three main models proposed by Challen and Oxley [10] describes the interaction of hard asperities affecting the friction by considering the three modes – ploughing of hard asperities on a soft sheet material, wear, and the cutting process due to

hard asperities. The underlying model is based on the Green's plasticity theory used to estimate the forces involved in the deformation process using slip line field analysis at the junctions. In a lubricated environment, the friction is reduced by the interfacial film formed on the asperities. In the model, the interfacial shear strength between the junction, angle of the hard asperity and velocity fields are used to calculate the coefficient of friction. The hard asperities are assumed not to deform with the normal load. The ploughing is characterized by the low attack angles of the tool asperities and low friction conditions. The ploughing process is discussed in greater detail in Section 2.6.

2.3.3 Shearing of lubricant film

Most of the engineering surfaces work with a lubricant to reduce wear and friction. The physical and chemical interactions between the metal-lubricant contacts influence the local friction conditions. Friction is produced by the shearing of the lubricant film due to sliding motion. The hydrodynamic flow of the lubricant between surfaces carries the applied load and reduces the contact between surfaces. In 1902, Stribeck [11] studied the variation of friction between the two lubricated surfaces and explained the coefficient of friction against the sliding velocity. Stribeck's curve for the lubrication of slider and roller bearings illustrates the frictional behaviour under lubricated conditions. Later, Hersey [12] systematically studied the lubrication and formulated a lubrication number which is a function of load, velocity and viscosity of the lubricant. In a forming process, the lubrication effect on the friction is typically dependent on the quantity of the lubricant as only a specified amount of lubricant is applied. For high speed and well lubricated processes, the coefficient of friction will decrease due to the increased separation of surfaces from hydrodynamic lubrication. The film thickness of lubricant is formed as a function of viscosity, velocity, pressure and geometry of the contact surfaces. For insufficient lubrication and low speed forming process, the coefficient of friction will be high since there is no load carried by the lubricant due to hydrodynamic flow. The lubrication regimes and friction mechanisms are discussed elaborately in Section 2.5.

2.3.4 Influence of asperity deformation process

The deformation process of the asperity indirectly contributes to the friction. The extent of the contact occurring between the surfaces is determined by the asperity deformation process. The asperity deformation is normally considered only due to the application of the normal load. It can also appear due to the bulk deformation of the sheet caused by stretching. The deformation process depends on the magnitude of the load and the hardness of the material ($H = 2.8\sigma_y$) according to [8]. If the load is small and material is hard, only elastic deformation occurs. In case of deep drawing of aluminium or steel, the hardness is low in comparison with the tool and the load is high in certain contact spots, resulting in mixed modes of deformation of the asperities [13]-[20]. The applied load is shared by the presence of lubricant in the valleys due to hydrodynamic pressure generation [1]. The work hardening of asperities will also occur in the case of a cold working process. The contact models to describe the flattening behaviour of the asperities are discussed in the following section.

2.4 Contact model

In this section, a brief overview of the contact modelling techniques is given for the tribological conditions in deep drawing processes. Contact problems are often encountered with the interaction between two deforming surfaces for normal loading. In deep drawing processes, additionally the effect of bulk deformation mode on surface deformation is also addressed. The extent of surface deformation depends on the material properties, surface roughness and applied load.

2.4.1 Asperity flattening due to normal loading

2.4.1.1 Statistical contact model

In literature, most of the contact models [13]-[20] assume that the contact occurs between the hard flat tool and the soft rough sheet material which is valid for SMF processes. Further assumptions about the deformation modes and shape of the asperities are critical for modelling the friction behaviour. The developed real contact area depends on the mode of deformation i.e. elastic, elastic-plastic and fully plastic [20]. For elastic deformation, the nominal pressure on an asperity depends on the equivalent elastic modulus at the contact interface and contact radius. Also for the plastic deformation, the contact area can be related to the hardness of the softest material. The fractional contact area, α, which is the ratio of real contact area to the nominal contact area can be calculated from the contact model. If the density of asperities in contact and the separation distance are known priori, the nominal pressure can be formulated for the given material properties. In the Figure 2.3, the contact between a rigid flat and rough surface is shown by means of a set of spherically shaped summits. Greenwood and Williamson's model [13] describes the contact between surfaces using spherical shaped summits with a radius, R, in contact with a flat surface. The surface is assumed to be of Gaussian distribution, $\phi(z)$, which gives the probability of occurrence of summits with a certain height, z. When a normal load, F_N, is applied, the surface is flattened through a distance h elastically with a certain density of summits, ρ, in contact. The model of Greenwood and Williamson [13] for nominal pressure, P_{nom}, and fractional contact area, ($\alpha = A_{real}/A_{nom}$), under elastic deformation of asperities is

$$P_{nom} = \frac{2}{3}\rho\sqrt{R}E^{*}\int_{h}^{\infty}(z-h)^{3/2}\phi(z)dz \tag{2.1}$$

$$\alpha = \pi\rho R\int_{h}^{\infty}(z-h)\phi(z)dz \tag{2.2}$$

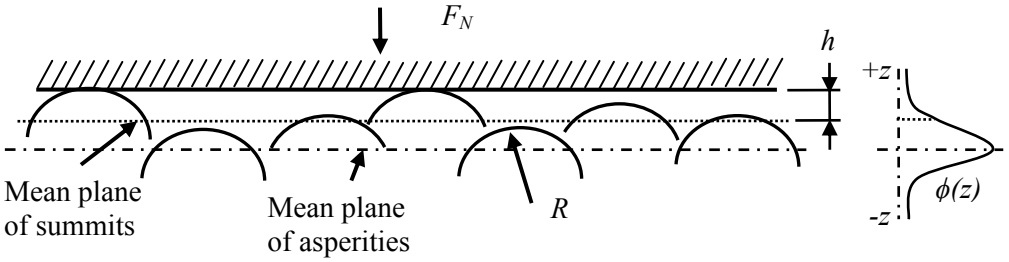

Figure 2.3: Statistical representation of surfaces for the contact between a flat and a rough surface.

Greenwood and Williamson's model is valid for only small deformations and large separations where the asperities deform independently. Plastic deformation occurs when the contact pressure is high.
Apart from summit based contact models, contact models also exist which take account of the complete deformation of the surface. In ideal plastic deformation, the real contact pressure in the asperity equals the hardness of the material. The fractional contact area is given as

$$P_{real} = H \; ; \; \alpha = P_{nom} \; / H \tag{2.3}$$

The fractional contact can be calculated from the surface height distribution, $\phi(z)$, for a given surface separation, h as follows:

$$\alpha = \int_{h}^{\infty} \phi(z) dz \tag{2.4}$$

The fractional contact area increases linearly with the contact pressure. However, in constrained situations the bulk material is restrained to flow outwards. Pullen and Williamson [15] observed that the linear increase of fractional contact area is not followed anymore when $P_{nom} > 0.3H$. Plastically deformed asperities require additional energy due to volume conservation (i.e. height of asperity indentation, (h-z), is equal to the rise of the asperity, (u)). The degree of contact with volume conservation is given as

$$\alpha = \frac{P_{nom}}{P_{nom} + H} \tag{2.5}$$

The fractional contact area, α and the rise of valleys, u, from the surface distribution, $\phi(z)$, is calculated as follows:

$$\alpha = \int_{h-u}^{\infty} \phi(z) dz \;\; ; \;\; u = \int_{h-u}^{\infty} (z - h + u) \phi(z) dz \tag{2.6}$$

The contact models have been extended by many researchers for elastic-plastic deformation [16] and work hardening [17]. However, these contact models are generic and cannot be applied directly to the deep drawing processes to describe the friction behaviour.

Westeneng [18] developed a statistically based contact model to describe the friction behaviour in deep drawing processes. The surface heights are represented as bars. The model is derived from the work energy principle and volume conservation. He considered the flattening and rising of asperities due to the interaction with neighbouring asperities. The model explains the asperity deformation under ideal plastic deformation for normal loading and bulk strain. A brief explanation of the model is presented in Section 4.2.

2.4.1.2 Deterministic contact model

For a real rough surface, the asperities do not have perfectly shaped geometry like spherical. The asperity distribution does not necessarily follow a Gaussian distribution. The spherically shaped summit with Gaussian distribution for the rough surface is an often used assumption in the statistical methods. The asperities occur with different heights and radii depending on the separation level. Deterministic methods are used by researchers [19]-[21] to characterize the shape of the asperity with real surface topography. The asperity shapes are characterized by fitting the micro-geometry with simple shapes like elliptical paraboloids using the volume and base area of the contact patches at the given separation level as described by de Rooij [22]. The characterization of the asperity by elliptical paraboloids is given in Section 5.4. This method of characterizing the asperities gives a better description of the shape than the spherical or conical geometries. In Chapter 5, the deterministic contact model is discussed elaborately to model the friction behaviour for asperity deformation and ploughing processes. Pure elastic deformation of the asperities will occur in very low loads. Full plastic deformation occurs at a load which is about 400 times higher than the initial plastic yield according to Johnson [23]. Asperities can undergo different modes of deformation depending on their size during repeated contact. In Chapter 6, a deterministic model explains the asperity deformation in elastic, elastic-plastic and plastic modes of deformation for loading and reloading conditions.

2.4.2 Asperity flattening due to bulk deformation

A characteristic feature of deep drawing is the bulk deformation. Both flattening and roughening of the sheet material surface are expected to occur in bulk strain conditions. Flattening of asperities occurs when the material is subjected to normal loading as well as stretching conditions. The models described for asperity flattening are based on the idealized asperity geometries. There are no analytical models which describe the arbitrarily shaped asperities for the bulk deformation process. Also the regularly shaped asperities are typically in a complex state of three dimensional stress and strain. Therefore, the models are simplified with a reduced stress or strain state. The flattening models discussed here are for wedge-shaped asperities as shown in Figure 2.4 under plane stress and plane strain conditions including normal loading and uniaxial strain conditions from [24] and [25].

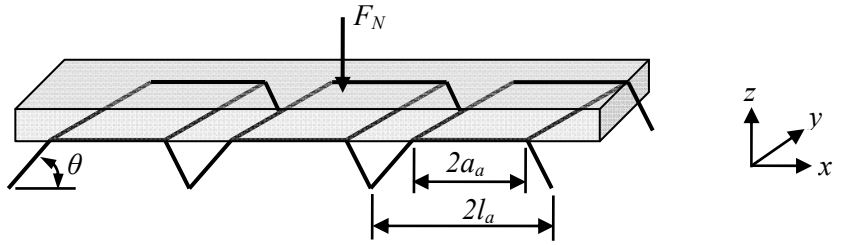

Figure 2.4: Wedge-shaped asperities for bulk deformation.

2.4.2.1 Plane stress model

Wilson and Sheu [24] developed an asperity deformation model based on the plane stress condition of the wedge-shaped asperities assuming that the length of the asperities is greater than the width. The wedges are assumed to have a constant slope, θ, and uniaxial strain, ε, applied parallel to orientation of the asperities (i.e. y-direction), as shown in Figure 2.4. Therefore a plane stress situation exist in the y-direction, where principal stress σ_{yy}=0. From the geometric analysis, Wilson and Sheu deduced a relation for the real area of contact of one asperity due to uniaxial strain as

$$\frac{d\alpha}{d\varepsilon} = \frac{1}{E\tan\theta} \tag{2.7}$$

The fractional contact area of one asperity is the ratio of half the width of the asperity, a_a, and to half the asperity spacing, l_a.

$$\alpha = \frac{a_a}{l_a} \tag{2.8}$$

The non-dimensional strain rate, E is defined as

$$E = \frac{\dot{\varepsilon}\cdot l_a}{v_a + v_b} \tag{2.9}$$

where, v_a and v_b are respectively the indentation velocity of the asperities and the rising velocity of the valley due to stretching. Since the asperities are equally shaped and constantly spaced, the total fractional area is equal to the contact area of a single asperity. The non-dimensional effective hardness obtained by Wilson and Sheu from the upper bound analysis of plasticity is given as

$$H_{eff} = \frac{P_{real}}{k} = \frac{2}{f_1(\alpha)E + f_2(\alpha)} \tag{2.10}$$

where the functions $f_1(\alpha)$ and $f_2(\alpha)$ are given as

$$f_1(\alpha) = 0.515 + 0.345\alpha - 0.86\alpha^2 \tag{2.11}$$

$$f_2(\alpha)=\frac{1}{2.571-\alpha-\alpha\ln(1-\alpha)} \tag{2.12}$$

2.4.2.2 Plane strain model

Sutcliffe [25] deduced the effective hardness with plane strain model for the same wedge shaped geometry as shown in Figure 2.4 which is used by Wilson and Sheu. With the assumption of unidirectional strain in perpendicular orientation of the asperities (i.e. x-direction), Sutcliffe performed the slipline analysis for an ideal plastic model. The relation between the real contact area and strain given by Sutcliffe as

$$\frac{d\alpha}{d\varepsilon}=\frac{1}{\varepsilon+1}\left(\frac{1}{E\tan\theta}-\alpha\right) \tag{2.13}$$

The effective hardness of the deforming material during bulk deformation is obtained from the relation

$$H_{eff}=\frac{2.72}{1-\alpha}\ln\left(\frac{0.826}{E}+0.152\right) \tag{2.14}$$

For both the models of bulk deformation process, the effective hardness decreases in line with the increasing non-dimensional strain, E. The fractional contact area is overestimated/underestimated by using upper and lower bound analysis of Wilson and Sheu [24] and Sutcliffe [25] respectively.

2.5 Lubrication in deep drawing processes

Most of the tribological systems consist of two or more interacting bodies and a lubricant. In the case of deep drawing processes, the sheet and tool interacts often with an intermediate layer of liquid lubricant. The application of a lubricant influences the process in one or more ways as mentioned below.

- Lubrication prevents the sheet material from corroding.
- Lubrication lowers the drawing force (i.e. frictional force) needed to perform the operation when compared with dry contact situations.
- Lubrication reduces the wear of tooling surfaces caused by adhesion and galling mechanisms.
- Lubrication prevents the product defects, such as tearing of the sheet material and wrinkling, by controlling the friction.

The lubricant eases the deep drawing processes and it results in an improved forming process. The understanding of the lubricant mechanisms on the surfaces is important for improving the forming process. In principle, the operation of the lubricant can be divided into three regimes (see Figure 2.5).

- Boundary lubrication regime – shearing of the lubricant layers formed on the surfaces during sliding.

- Hydrodyanmic lubrication regime – hydrodynamic flow of the lubricant between the surfaces during sliding causes the surfaces to separate.
- Mixed lubrication regime – combined shearing of the lubricant layers and hydrodynamic flow between surfaces during sliding.

These lubrication regimes are discussed in detail in the following sections.

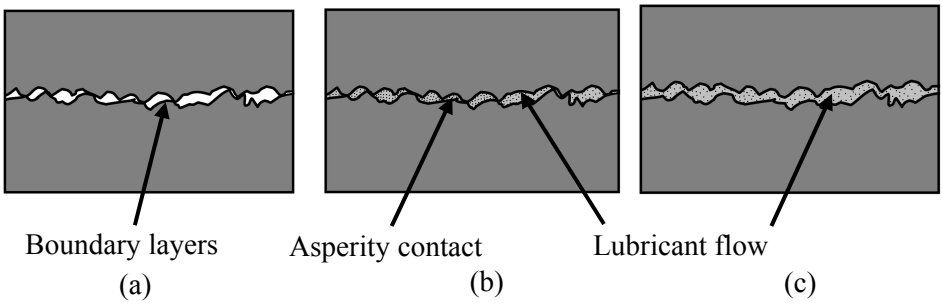

Figure 2.5: Different modes of lubrication (a) Boundary lubrication (BL), (b) Mixed lubrication (ML) and (c) Hydrodynamic lubrication (HL).

2.5.1 Boundary layer lubrication

In the presence of lubricant, the interacting surfaces are contaminated. The welding of asperities is prevented by this contaminated layer if it remains intact. Conservation oils with lubricating properties can be used for deep drawing operations, although sometimes the sheets are applied with a dedicated lubricant according to customer requirements. Lubricants can contain organic compounds such as phosphorous and calcium. Sometimes antioxidants or extreme pressure additives are also used along with the base oil. However, the use of these additives is becoming more and more restricted for environmental reasons. The molecular mechanisms of the oil and its additives result in the formation of boundary layers on the surfaces. The boundary layers are formed by two mechanisms – physical adsorption and chemical adsorption.

2.5.1.1 Physical adsorption

Molecules of non-polar fluids (such as pure mineral oils) bond to the metal surfaces by weak Van der Waals forces. During sliding, physical adsorption is sufficient to transmit the shear forces into the bulk fluid. However, under severe (local) sliding conditions, the weak bonding forces may break down the boundary film, allowing the surfaces to contact. Hence the typical friction values in boundary lubrication are high due to the local failure. The molecules of boundary layers consist of fatty acids, alcohols and amines. The mechanisms of boundary lubrication are explained by the formation of long hydrocarbon chains with polar groups at the end. These polar ends attach to the metal surface by means of physical adsorption, forming parallel chains when the load is applied, as shown in Figure 2.6. The physical adsorption of lubricant on inactive materials like gold and platinum are studied by Bowden and Tabor [8] and Timsit and Pelow [26]. The bonds between the chains determine

the shear strength of the lubricant. The shear strength depends on the number of chains, molecular weight and the number of carbon and hydrogen atoms.

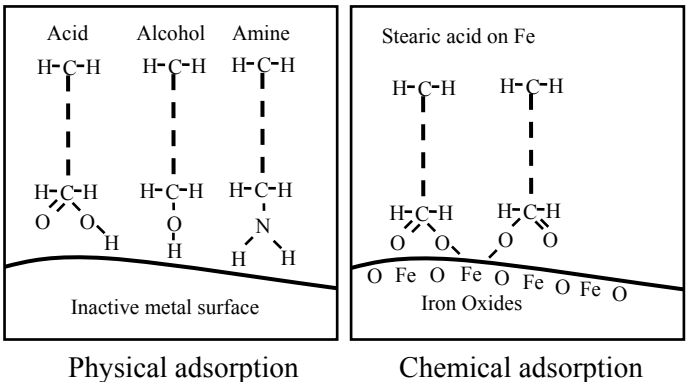

Figure 2.6: Boundary layer formation mechanisms [8].

2.5.1.2 Chemical adsorption

Chemical adsorption is the formation of boundary layers by means of chemical reaction between the surface and the lubricant. After the formation of lubricant layers by means of physical adsorption, a chemical reaction occurs between the surface and polar groups of the lubricant. The chemical reaction depends on the type of lubricant and environmental conditions. Under atmospheric conditions, iron oxides are formed due to the oxidation process. When the lubricant is applied, it reacts with iron oxides and forms chemical bonds. In case of stearic acid type of lubricants, iron stearates are formed by the chemical reaction as shown in Figure 2.6. According to Akhmatov [27], adsorption is aided by oxide film and the presence of water. This might be because in dry conditions the molecules of acid exist as lined pairs which are broken by the presence of water. The adsorbed film on the metal surface protects the metal to metal contact and reduces the shear strength of the interface, junction growth and wear.

2.5.1.3 Boundary layer desorption/degradation

When the boundary layer properties degrade, the direct metal to metal contact may occur during sliding. Increase in temperature is considered to be the main reason for the degradation. Due to frictional heating, the temperature at the local contact spot of asperity is high; this is known as flash temperature. At a critical temperature, the adsorbed layer becomes disoriented, boundary links collapse and the surface becomes unprotected. Blok [28] postulated that the frictional heat generated during sliding weakens the strength of boundary layers. The frictional heat quantity per second, q, for a sliding contact is given as

$$q = \mu F_N U \tag{2.15}$$

Another reason for boundary layer degradation could be the limited chemical compatibility of the metal and lubricant. The reduced reactivity of certain metal-lubricant combinations decreases the effectiveness of the lubricant. When a hard asperity ploughs through the

surface, the underlying metal is exposed to the contact. Desorption of the lubricant is not instantaneous. Further, if the contact time between the asperities of the surface is too short, the chemical reaction will not occur.

2.5.2 Hydrodynamic lubrication

In this regime, there is no physical contact between the contacting surfaces and the load is carried completely by the lubricant film formed between the surfaces. Under the complete separation of surfaces, the coefficient of friction could be low in the order of 0.01. When the normal load is high, elastic deformation occurs at the contacting surfaces. This is known as Elasto Hydrodynamic Lubrication (EHL) [29]. When the load is high and the hardness is low, it can also cause plastic deformation of surfaces. This is known as Plasto Hydrodynamic lubrication (PHL) [29]. The frictional characteristics are determined purely by the shearing action of the fluid and modelled by the use of fluid dynamics theories like the Navier stokes or Reynolds equation for calculating the film thickness and pressure distribution. For full film lubrication, the film thickness to surface roughness ratio, h_{lub}/S_q, should be around 3.0. The full film regime is unlikely to happen in deep drawing processes since the ratio h_{lub}/S_q is in the order of 0.6-2.0 and the lubricant amount is low compared with the surface roughness.

2.5.3 Mixed lubrication

In SMF processes, ML is favoured due to limited amount of lubricant. In the ML regime, the applied load is shared between the contacting asperities and the lubricant present in the valleys. The lubricant flow in ML is described as HL (considering the 1D flow) as given by Reynolds equation:

$$\frac{\partial}{\partial x}\left(\frac{\rho_{\mathrm{lub}} h_{\mathrm{lub}}{}^{3}}{12\eta_{\mathrm{lub}}}\frac{\partial P_{nom}^{\mathrm{lub}}}{\partial x}\right)=\frac{U_1+U_2}{2}\frac{\partial\left(\rho_{\mathrm{lub}} h_{\mathrm{lub}}\right)}{\partial x}+\frac{\rho_{\mathrm{lub}} h_{\mathrm{lub}}}{2}\frac{\partial(U_1+U_2)}{\partial x}+\frac{\partial(\rho_{\mathrm{lub}} h_{\mathrm{lub}})}{\partial t} \qquad (2.16)$$

The Reynolds equation is valid for the thin film flow between surfaces under the following assumptions:

- The flow is laminar.
- The fluid behaviour is Newtonian (i.e. shear stress is linear with strain rate).
- No slip condition, the fluid adheres to the surfaces.

The two types of flow which can be observed are:

- Poiseuille flow
- Couette flow

The left side term in the Reynolds equation (2.16) represents the Poiseuille flow which is the pressure driven flow. The terms on the right side of the Reynolds equation describes the three effects.

- Wedge effect – the flow due to the change of fluid film separation height.
- Stretch effect – the flow due to the elongation of surfaces in the direction of flow.
- Squeeze effect – the flow due to the change of density or film thickness over the time.

Most of the fluid flow models neglect the squeeze effect and stretch effect when applied to lubrication problems for the forming process by assuming that these effects are negligible in comparison with the other contributions [30] - [35].
A schematic representation of the different regimes of lubrication is shown in a Stribeck plot (see Figure 2.7). The Stribeck plot shows the coefficient of friction against the lubrication number as defined by Hersey [36]. Schipper [37] non-dimensionalised the lubrication number with the composite roughness of the surfaces.

$$L = \frac{\eta_{\text{lub}} U}{P_{nom} R_a} \tag{2.17}$$

The coefficient of friction is determined by the lubricant regime in which the tribological system operates, as shown in Figure 2.7. For boundary lubrication, the friction is high (in the order of 0.1~0.2), since the formed layers have higher shear strength than the bulk lubricant. In a full film hydrodynamic regime, the coefficient of friction is usually low and is in the order of 0.01. In this lubrication regime, the friction is determined by the properties of the lubricant owing to the conditions. With the increased pressure and shear rate, the shear strength of the lubricant typically increases. Hence the coefficient of friction increases to a certain degree in full film regime. In the mixed lubrication regime, the friction transits from the BL to HL as soon as the fluid film builds up due to process conditions (contact pressure and sliding velocity).

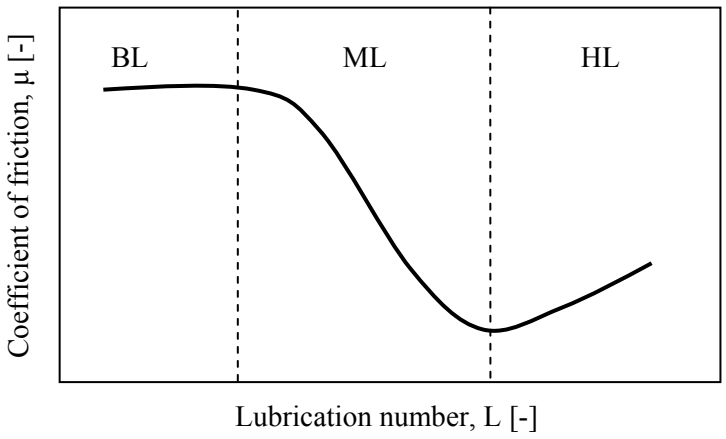

Figure 2.7: Schematic representation of Stribeck plot.

In literature, most of the lubrication models are applicable to rolling and sliding contacts of gears and bearings where the lubricant film thickness is determined from the inlet geometry of the interacting surfaces. However, in a deep drawing process scenario, the tool and sheet material contact is nominally flat. The film thickness variation causing a wedge effect can be considered only from the progressive asperity flattening processes. Johnson et al. [38] used the Greenwood and Williamson model [13] for deformation of the surface and Christensen's model [39] for surface effects to describe a model for the hydrodynamic lubrication process. The film thickness in this model was described by the surface geometry of the interacting bodies and the surface texture incorporated with the elastic deformation of

asperities. This model can be applied only for elastic contacts where there is no severe asperity flattening. Patir and Cheng [40] used the Reynolds equation neglecting the stretch and squeeze effects to derive a thin film flow model for the rough surfaces with the flow in one direction, as shown in Figure 2.8. In their work, the Reynolds equation (2.16) has been used with flow factors for the shear and the pressure flow for the given roughness of the surface. However, this method is unsuitable if the surface separation becomes very small which happens in deep drawing operations with high fractional contact areas.

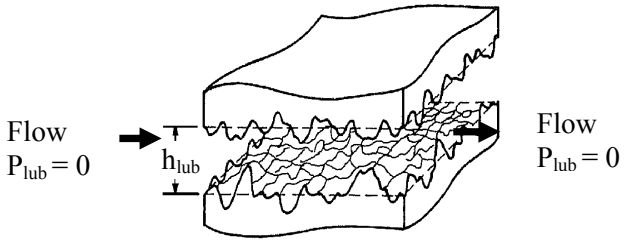

Figure 2.8: Flow factor simulation with rough surfaces [40].

Sheu and Wilson [30] modelled the mixed lubrication process for the high speed strip rolling by using the asperity contact model for wedge-shaped asperities of Wilson and Sheu [24] (see Section 2.4.2). This model predicted a higher inlet film thickness for the ML conditions than the thick film theory developed by Wilson and Walowit based on HL theory [31] due to the contribution of asperity contact to support load. Wilson and Chang [32] developed a model for the bulk metal forming under the low speed conditions where the inlet zone does not contribute significantly to hydrodynamic pressure generation. The model treated the flow of isoviscous lubricant between the longitudinal saw tooth shaped asperities of workpiece and a flat tool. The flow is characterized by the Reynolds equation with the film thickness calculated from the geometric relations of the saw tooth asperities. The asperity flattening model is based on the previous model of Wilson and Sheu [24]. This model [32] gave a better understanding of the hydrodynamic actions under low speed conditions which are usually neglected. Wilson and Marsault's model [33] gave an insight into the behaviour of the lubricant in a metal forming operation under high fractional contact areas (see also Appendix A). When the film thickness reaches the threshold (see Equation (A.3), Appendix A), the influence of pressure gradient flow of the lubricant (i.e. Poiseuille flow) becomes negligible and the pressure flow factor will tend towards zero. Under such conditions hydrodynamic pressure generation is only due to Couette flow. Ahmed and Sutcliffe [41] have shown experimentally the formation of micro pits in stainless steel at considerable fractional contact area for low speed forming operations. In rolling, the elimination of micro pits is restricted more, due to the hydrostatic effect of the lubricant trapped in the pits. In strip drawing, the lubricant is drawn out of the pit due to the sliding action. Additionally, the strip drawing results with the artificial indents confirm the Micro Plasto Hydrodynamic Lubrication process. Helenon et al. [42] have considered the two contacting surfaces as rough by assuming saw tooth and sinusoidal surfaces. The

lubricant pressure development shows an increase for the two rough surfaces in comparison with the regular smooth tool and rough sheet material. Le and Sutcliffe [34] used a longitudinal roughness on a primary scale to the rolling direction and a transverse roughness on the secondary scale to the rolling direction. In the primary scale, the lubricant pressure is assumed to be constant across the valley and the averaged Reynolds equation is used to calculate the lubricant pressure along the rolling direction, with the primary scale contact area originating from the secondary scale where the asperities are transversely aligned to the rolling direction. The secondary scale contact area is calculated based on the assumption that the oil will be trapped, since the surface roughness lay (see Equation (C.11), Appendix C) is transverse to the rolling direction. Lo and Yang [35] used the flattening model developed by Wilson and Sheu [24] and developed a mixed lubrication model related to the metal forming process for the FE implementation.
Klimczak and Jonasson [43] analysed the real area of contact and change of roughness with the deep drawn steel sheets. The high fractional contact area development results in entrapment of lubricant in the valleys near the die rounding regions where high plastic deformation occurs. These lubricant pockets will be pressurized and reduces further contact area development. In the blank holder region, the lubricant is squeezed and causes a shift from BL to ML regime. This is due to the pressurized fluid which can be easily delivered to the other valleys. This action prevents the breaking of the film separating tool and sheet material, and the hydrodynamic flow persists. Roizard et al. [44] showed the influence of roughness orientation on lubricant flow in a deep drawing process experimentally on mill finished aluminium sheets. When the surface lay is orthogonal to the sliding direction, there is a hydrodynamic effect of the lubricant in the valleys and this reduces the friction. If the sliding direction is parallel to the surface lay, the lubricant is squeezed out of the contact zone and the friction is dominated by the boundary lubrication. An in-situ observation of the micro wedge effect of the lubricant for drawing experiments in aluminium by Lo et al. [45] is shown for longitudinal and transverse roughness. The longitudinal and isotropic surface roughness shows a monotonic increase of contact area higher than the transverse roughness lay. This is due to the hydrodynamic pressure generation in transverse roughness being higher than for the other surfaces. Ter Haar [1] measured friction values with a linear friction tester simulating deep drawing conditions and modelled Stribeck curves with a tanhyp fit. The coefficient of friction is influenced by the roughness of the sheet and tool surfaces, lubricant and sliding velocity. The empirical friction models were used in FE simulations to show that the coefficient of friction significantly influences on punch forces characteristics, stresses and strains. Wihlborg and Gunnarsson [46] showed experimentally the presence of hydrostatic effects in EBT uncoated steel in bending under tension friction test. The surfaces were specifically textured with isolated pockets to improve the performance of deep drawing processes. The hydrostatic effects were found for medium rough steel which has a large number of isolated oil pockets and shows less friction than the rougher or smoother surfaces. However, the friction reduction due to hydrostatic effects is minor. If there are a larger number of oil pockets, higher mixed lubrication effects due to hydrostatic lubrication can be expected. These experiments confirm the presence of hydrodynamic lubrication effects in the deep drawing processes.

2.6 Ploughing model

As mentioned earlier, the contact between hard asperities of the tool and soft sheet material in deep drawing processes results in ploughing. Only a fraction of the surface is in contact and the asperity bears large loads. The harder tool asperities plough through the deformed sheet material asperities during sliding. Challen and Oxley [10] performed a slip line field analysis for the deformation of a soft surface by a hard asperity for the corresponding coefficients of friction and wear rates. From the slip line analysis of triangularly shaped asperities, three main modes – ploughing, cutting and wear mode are proposed as shown in Figure 2.9. For low attack angles and interfacial shear strength, the ploughing shows only plastic deformation of the soft surface without any removal of material. For the rougher surfaces with high attack angle, the material removal occurs by a chipping or a wear process depending on the interfacial shear strength. The film shear strength ranges from zero (perfect lubrication) to the shear strength of the soft material (welding of junctions). The model follows the frictional force proportional to normal load and independent of contact area (i.e. following the basic laws of friction). The model has two important parameters for calculating the coefficient of friction; as already mentioned, which are attack angle of the asperity, β and friction factor for the interfacial film, $f_{hk} = \tau_{BL}/k$, $(0 \le f_{hk} \le 1)$. For a dry contact, the interfacial friction factor can approach close to unity. In the case of contact in the boundary lubrication regime, the friction factor is reduced. It typically ranges between 0.4 and 0.7, even though the lubricant shear strength is lower. The boundary layers at the asperity contact can fail due to temperature or sliding conditions and then direct metal contact occurs.

In the ploughing mode of deformation, the coefficient of friction is given as

$$\mu = \frac{B\sin\beta + \cos\left(\cos^{-1} f_{hk} - \beta\right)}{B\cos\beta + \sin\left(\cos^{-1} f_{hk} - \beta\right)} \tag{2.18}$$

where $$B = 1 + \frac{1}{2}\pi + \cos^{-1} f_{hk} - 2\beta - 2\sin^{-1}\left(\frac{\sin\beta}{(1-f)^{1/2}}\right)$$

In the wear mode of deformation, the coefficient of friction is given as,

$$\mu = \frac{\left\{1 - 2\sin\beta^* + \left(1 - f_{hk}{}^2\right)^{1/2}\right\}\sin\beta + f_{hk}\cos\beta}{\left\{1 - 2\sin\beta^* + \left(1 - f_{hk}{}^2\right)^{1/2}\right\}\cos\beta + f_{hk}\sin\beta} \tag{2.19}$$

where $$\beta^* = \beta - \frac{1}{4}\pi - \frac{1}{2}\cos^{-1} f_{hk} + \sin^{-1}\frac{\sin\beta}{\left(1 - f_{hk}\right)^{1/2}}$$

In the cutting mode of deformation, the coefficient of friction is given as,

$$\mu = \tan\left(\beta - \frac{1}{4}\pi + \frac{1}{2}\cos^{-1} f_{hk}\right) \tag{2.20}$$

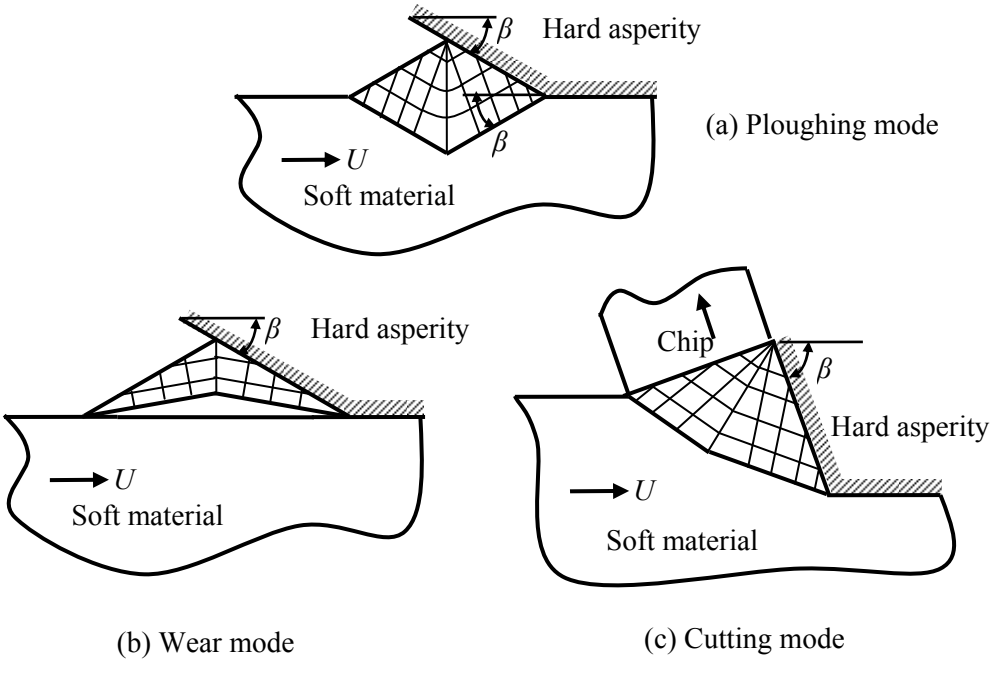

Figure 2.9: Different modes of deformation according to Challen and Oxley [10].

2.7 Surface Roughening

2.7.1 Overview

Surface roughening is the process of change of roughness during the bulk deformation in deep drawing processes. Roughening reduces the real contact area between the tool and sheet material. Roughening process depends on the bulk strain, grain size, initial roughness and material lattice structure. The effect of increased roughening is shown for large grain sized material by Kienzle and Mietzner [48]. Oskada and Oyane [49] studied the effect of the lattice structure on the roughening of aluminium materials. They found an increasing roughening effect for the materials with a small number of slip systems. The roughening tendency can be seen more in HCP (Hexagonal Close Packed – 3 slip systems) than FCC (Face Centered Cubic – 12 slip systems) and BCC (Body Centered Cubic – 48 slip systems) materials. The roughening effect was also found to be proportional to the grain size of the material. The larger the grain size, the higher the roughening rate. Atala and Rowe [50] studied the roughness change for the rolling process with the lubricant. Their main conclusion is that the asperities tend to flatten easily and the valleys persist longer due to hydrodynamic pressure. When the deformation occurs at very high pressure, the lubricant may escape from the valleys depending on the roughness lay. Thomson and Nayak [51] aimed to study the roughness change of deep drawn steel cups with the mode of plastic deformation and examined the potential of the valleys in the profile to grow. At small plastic strains ($\varepsilon = 0.1$), the increase in the roughness is due to the aggravation of features in

the original profile. At intermediate strains new surface features forms from the slip bands. At high strains (ε = 0.3), the modified surfaces continue to roughen and the creation of new features occurs. They also showed that roughening increases with the reduction of initial blank thickness in the uniaxial tension test. Guangnan et al. [52] found that the roughening rate of steel is dependent on the strain rate and the initial roughness. For steel, the roughening is due to the grain rotation rather than void growth or slip emergence as in aluminium. Lubbinge et al. [53] studied the influence of plastic bulk deformation on the surface roughness of the steel during free deformation in uniaxial strain conditions. For small strains, smoothing of the surfaces occurs; this might be due to light distortions and at high strains the roughening process actually takes place.
In deep drawing processes, the deformation occurs in a complex manner at different contact points of the sheet material with the die. There are six major contact areas identified in the deep drawing process as shown in Figure 2.1. Amongst the featured contact spots, the operating conditions, material, lubricant and surface properties play a significant role in the roughening process. The experiments of Wichern et al. [54] and [55] on roughness change without lubricant showed that the increase of sliding distance has decreased the final roughness of the surface. In deep drawing processes, the sheet material is in contact with the blank holder, die and punch where flattening will occur. The sheet material between the die and punch rounding regions is deforming under no contact conditions. In these regions, the roughening process is likely to happen. In deep drawing, bending occurs near the die and punch rounding regions. The bending action over these contact spots causes a tensile and compression stresses over the thickness of the sheet which affects roughening of the sheet material.

2.7.2 Surface roughening model

Lee [56] proposed an upper bound model for surface roughening in aluminium material during straining. He considered the difference in hardness of the grains in the surface causes roughening for aluminium. He also developed a geometry based model for the grain rotation process for the applied bulk strain. The model has been adapted to define the roughening process in steel for a grain rotation mechanism. The roughening model consists of grains with an active slip system. There are two stages in the roughening process depending on the strain. In the first stage, the grains deform plastically when the strain is low. The smoothening of surface takes place due to the flattening of grains. In the second stage, as the strain increases, the critical shear strength between the grains is reached and the grains start to rotate. Thereby, the grain rotation causes the surface to roughen.
A schematic representation of the smoothening and roughening of the surface is shown in Figure 2.10. The grain size, g_s, and active slip angle of the grain, θ_g, are the input for the roughening model. The roughening process is modelled by the geometric rotation of grains. The result of the roughening model is shown in Figure 2.11 for the given bulk strain. For explanations about the roughening model, the reader is referred to Appendix B. With the increase in grain size, the surface roughening process increases, as shown in Figure 2.11(a). The grains with higher active slip angle roughen more, as shown in Figure 2.11(b).

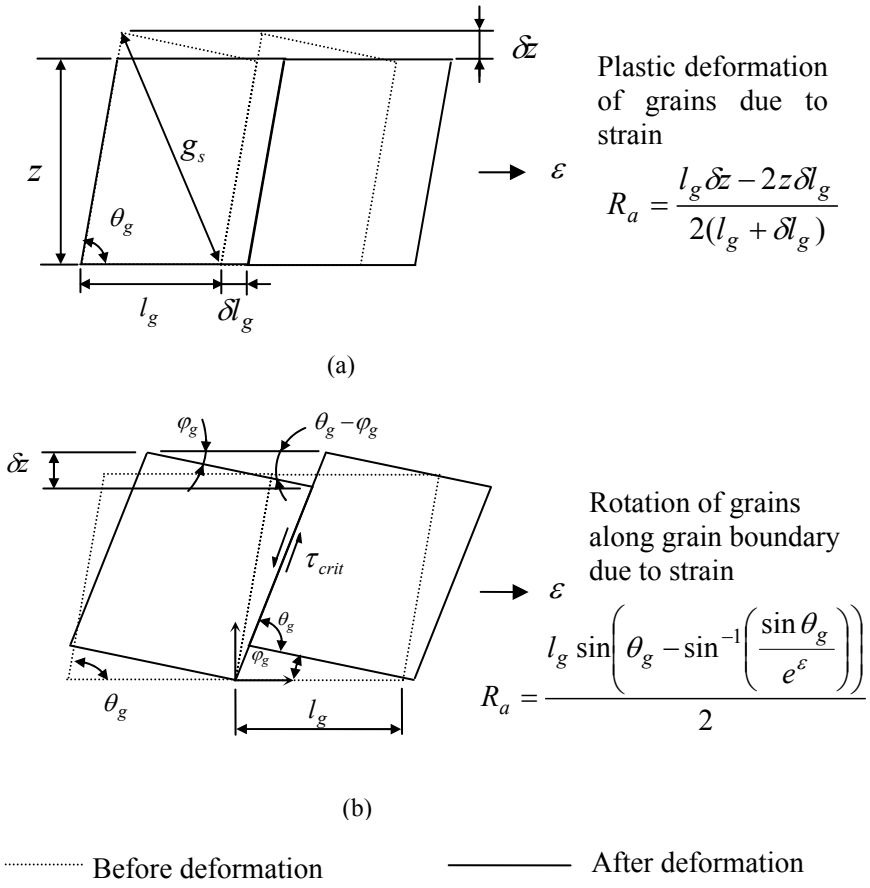

Figure 2.10: Schematic representation of surface roughening process (a) Smoothening at small strains and (b) Roughening at large strains, [56].

The effect of smoothening during the low strain is included as well. The roughening process takes place when the applied strain reaches the critical shear strength at the grain boundary. The shear strength at the interface is resolved from the applied stress using the Nadai hardening law and the Schmid factor:

$$\tau_g = \left(C\left(\varepsilon_0 + \varepsilon\right)^n \right) \cdot M \tag{2.21}$$

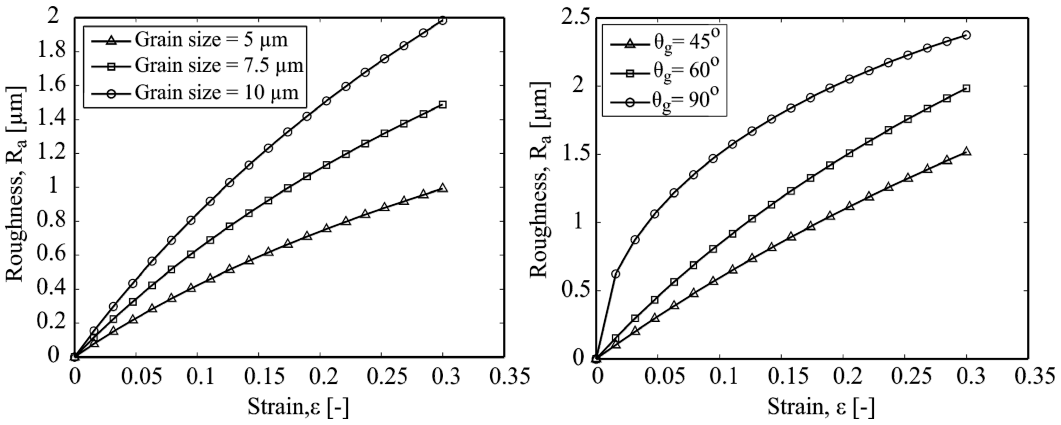

(a) (b)

Figure 2.11: Surface roughening for various (a) Grain size and (b) Grain orientation.

The Schmid factor, *M*, gives the projection factors for the critical resolved stresses with respect to the orientation of the grains and to the applied stress for the rotation of grains. The effect of strain on smoothening and roughening is shown in Figure 2.12. Although the model is quite simple, it can predict the trend of smoothening and roughening behaviour quite well. The roughening process depends on the lattice structure of the metals. The transfer of the roughening process from the lattice structure to the actual surface topography is cumbersome at this stage. It is important to predict the changes in surface due to the roughening process for friction modelling. Although the grain rotation can be described with simple models, lack of in-depth knowledge about roughening and transformation to the surface topography limits the application of the current model.

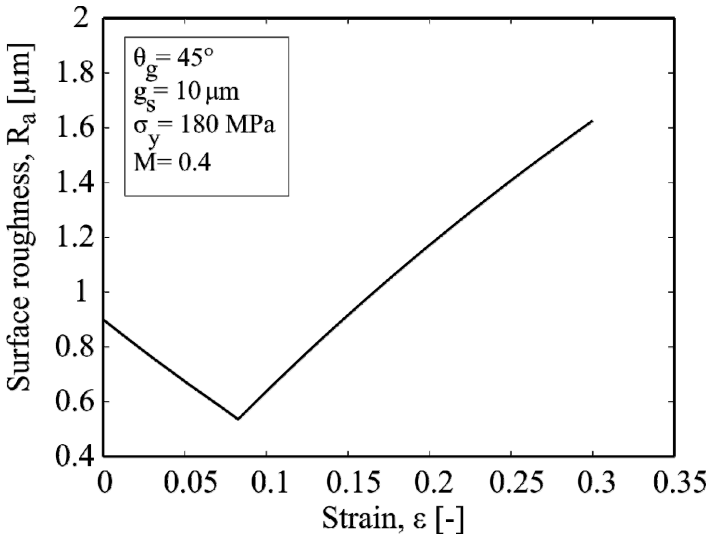

Figure 2.12: Surface roughness change.

2.8 Overview of friction modelling in deep drawing processes

In this section, an overview of the friction model is explained based on the above-mentioned asperity micro-mechanisms. In deep drawing processes, the tribological system is composed of three elements – sheet material surface, tool surface and lubricant. The friction model should encompass all three elements interacting mutually. In the friction model, three main steps are distinguished here. In the first step, the flattening of asperities due to normal loading and stretching is considered. In the second step, the hydrodynamic lubrication between the tool and sheet material surface is considered, depending on the amount of lubrication. In the final step, the coefficient of friction is calculated from the individual contribution of the friction forces from the asperity contact and shear of the lubricant.

2.8.1 Asperity flattening

The asperity flattening process of the sheet material surface is due to the interaction between the sheet material and tool with the application of load and strain. The tool surface is treated as flat at this stage since the order of roughness is relatively low when compared with sheet material surface. The sheet material is normally cold rolled by means of textured rolls. The RMS roughness of the sheet material surface, S_q, is around 1~2 μm. The tool surface roughness is usually polished with grinding/lapping process with a roughness of around 0.1~0.2 μm. Therefore the tool roughness on the asperity flattening can be considered as negligible when describing the contact between thw two surfaces. The parameters which influence the deformation of asperities are material properties, mode of deformation, the distribution of asperities and the contact pressure.

2.8.2 Hydrodynamic lubrication

Lubricant is normally applied in the deep drawing processes to prevent the corrosion and to improve the product formability. During the progressive deformation of the asperities, the lubricant will be trapped in the roughness of the sheet material. Due to sliding, the lubricant will flow in the interconnected valleys of the surface. The hydrodynamic pressure in the valleys of the surface limits the asperity flattening process, since the total applied load is shared between the asperity and lubricant. The hydrodynamic pressure generation depends on the fluid film thickness, sliding velocity, lubricant properties and surface roughness.

2.8.3 Calculation of the coefficient of friction

In the final step of the friction model, the coefficient of friction is calculated from the shear of the lubricant (in the case of any hydrodynamic lubrication) and shear of the interfacial layers (BL and ploughing). The shear strength of the lubricant without any pressure and temperature dependency is given according to the Newtonian behaviour of the lubricant as,

$$\tau_{\mathrm{lub}} = \frac{\eta_{\mathrm{lub}} U}{h_{\mathrm{lub}}} \tag{2.22}$$

The shear strength of the asperity contact is dependent on the shear strength of the boundary layers and ploughing forces. The ploughing forces depend on the geometry of the tool asperities which plough through the deformed plateaus of the sheet material asperities. If the total friction force due to ploughing is F_W, the shear strength of the solid contact is

$$\tau_{sol} = F_W / A_{real} \tag{2.23}$$

From the fractional contact area, the coefficient of friction is calculated as

$$\mu = \frac{\alpha \tau_{sol} + (1-\alpha)\tau_{\text{lub}}}{P_{nom}} \tag{2.24}$$

2.9 Analysis of surface properties for DC06 sheet material and deep drawing tool surface

Typical surfaces of the sheet material and tool surfaces from the materials used in the deep drawing processes are shown in Appendix C (see Figure C.1 and Figure C.2). The surfaces of the DC06 steel surface have been measured with a confocal microscope at six different spots. The distribution of the sheet material surface is shown in Figure 2.13 (a). The figure shows the frequency of occurrence of the asperities for the given height. The random distribution of the surfaces varies from one measurement to another. However, the variation in height distribution does not clearly indicate how the real contact area changes. In Figure 2.13 (b), the bearing area of the surface is shown. It can be seen that the fractional contact area vary from each other especially at high separation levels. In deep drawing processes, the contact pressure is not very high. It can be expected that the separation level is high for low contact pressures where the fractional contact area varies significantly for each surface. The real contact area will affect the coefficient of friction. Hence, the friction model should account for the variation in the surfaces.

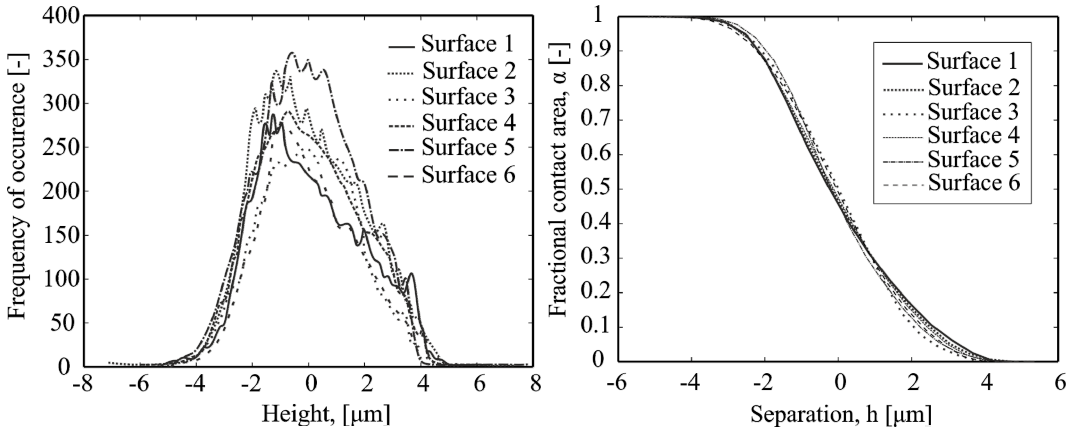

Figure 2.13: Properties of DC06 steel surface (a) Distribution of surface roughness (b) Bearing area of the surface

The geometry of the asperities on the tool surface is also critical to the friction prediction. The surface geometry is usually characterized by the asperity radius and the number of asperities in contact. In the ploughing model, the geometry of the tool asperities is important since the indentation process is shape and size dependent.
Summits are the local maxima of the surface heights in the statistical approach. During the loading process, only top summits will contact. However, the growth and merging of summits are not considered in the statistical analysis.
Asperities are the geometrical description of the micro-contacts obtained from the surface height data. During contact, asperities merge together with the neighbouring contact patches to form a bigger asperity. de Rooij [22] prescribed a method to characterize the asperity geometry based on the volume and contact area of the asperity as shown in Figure 2.14 (see also Chapter 5).
The location of the summits and asperities from the surface at a separation level $h/\sigma_z = 1$ are plotted in Figure 2.14 (a) and (b). It can be clearly seen that the number of asperities and summits are different. The size and the number of the asperities in contact varies depending on the surface separation level using deterministic approach as shown in Figure 2.14 (c). It can be seen that the number of asperities increase with a lower value of surface separation and also big asperities are formed due to clustering of contact patches. The big asperities will be dominant in carrying the applied load.

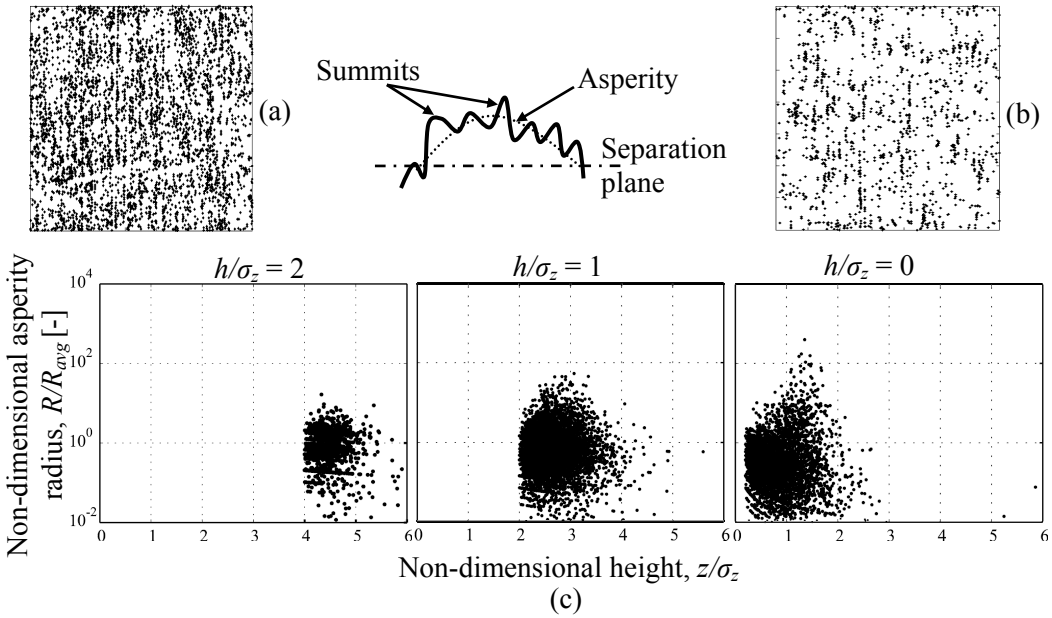

Figure 2.14: At a surface separation of $h/\sigma_z = 1$, the location of the (a) summits found by statistical representation (b) asperities found by a deterministic approach. (c) Asperity radius at given separation of the surface using a deterministic approach.

2.10 Summary

In this chapter, a review of micro-mechanisms responsible for friction in deep drawing processes has been presented in detail. The influence of contact conditions between sheet material, blank holder, punch and die is discussed. The influencing mechanisms for friction modelling in deep drawing processes are asperity deformation, ploughing and lubrication. A detailed overview of contact models for the micro-mechanisms is presented. The coefficient of friction is strongly dependent on the boundary layer properties and ploughing. The increase in contact pressure increases the shear strength of boundary layers. For ploughing, the geometry of the tool surfaces is critical to the friction prediction. Sharper asperities result in a high coefficient of friction, while blunt asperities result in a low coefficient of friction. In the case of well lubricated conditions, mixed lubrication effects play an important role. The lubricant properties, asperity deformation and sliding conditions influence the mixed lubrication process. Moreover, all of these friction mechanisms are dependent on the distribution of the sheet material and tool surfaces. From the literature review, it can be seen that the contact models have been well established for the deep drawing models. Westeneng [18] developed a statistical model to describe the friction in deep drawing processes. The asperity deformation model is developed for normal loading and bulk strain in the boundary lubrication regime. However, there were important shortcomings of the friction model as discussed below.

- The boundary layer models used are from the experiments of [26], [57]-[64] which were performed on materials like mica, glass, gold and aluminium. Hence determination of boundary layer is related essentially to the metal-lubricant combination in deep drawing processes.
- The mixed lubrication is known to occur in the deep drawing processes due to the hydrodynamic lubrication in the valleys of the surface roughness during deformation. In deep drawing, less amount of lubricant is applied. The hydrodynamic pressure generation is not from the inlet geometry but due to progressive asperity deformation process under low speed process conditions, as described by [32], [35] and [46].
- The asperity geometry is typically represented by a single asperity with a constant mean radius and summit density at all separation levels. However, it has been shown from the surface analysis that the asperity geometry is not unique. Depending on the contact load (i.e. surface separation) the number of asperities and the asperity geometry vary. The contacting heights will merge together, thus changing the shape of the asperity. This will influence the friction coefficient depending on the surface topography. During ploughing, the indentation hardness of the material should be size and shape dependent.
- When the asperity radius is small, plastic deformation occurs even at low loads. In case of large asperities, mixed modes of deformation are likely to occur. The friction model of [18] is developed based on the assumption that the asperity deformation and indentation process is completely plastic. The contact model is needed to include the mixed modes of deformation. Contact loading/reloading of the surfaces and the friction evolution can be explained with the inclusion of the elastic deformation mode in the contact model.

Chapter 3
DETERMINATION OF THE BOUNDARY LAYER SHEAR STRENGTH

3.1 Introduction

Deep drawing processes are mostly performed in lubricated conditions. If the lubricant amount is insufficient to cause hydrodynamic lubrication, the friction forces arise mainly due to shearing of the boundary layer present between the sheet metal and tool surfaces. Boundary layers are formed due to either physical or chemical adsorption on the interacting surfaces as explained in Section 2.5.1. For lubricated contacts during sliding, the friction force arises due to boundary layer shearing and ploughing. The combined effect of boundary lubrication and ploughing is modelled by Challen and Oxley [10]. The model is developed for a single hard asperity deforming the softer material plastically with the slipline theory. In this chapter, the friction force due to boundary layers is studied in detail on the basis of review of the literature and the friction experiments performed on steel-steel contact. Further, the influence of the real contact area on the boundary layer friction is shown and also a comparison with the existing model is shown.

3.2 Boundary layer lubrication models

Hardy and Doubleday [57] postulated for sliding metallic surfaces that there is another kind of lubrication regime known as boundary lubrication. When the surfaces are near enough, physical and chemical mechanisms of the lubricant directly influence the properties of the interfaces. The physical mechanisms of adsorption and friction of a thin layer of lubricant are researched by [58]-[61]. The experiments to find the effect of interfacial boundary layers on friction are usually carried out with mica or glass with a low roughness for a circular contact or a cylindrical contact. The friction is measured using a surface force apparatus which makes a reciprocating movement. Since the surface is of low roughness and high hardness, the surfaces deform elastically. Experiment results show that the shear strength of boundary layers is due to shearing of boundary layers since no breakage of film was observed. The shear strength is calculated from the measured friction force and the calculated contact area for the applied normal load according to the Hertz contact theory. The influence of temperature, pressure and sliding velocity are shown on the shear strength for combinations of different materials like glass, mica and aluminium. Westeneng [18] gave a comparison of the boundary layer lubrication experiments available in the literature

as shown in Figure 3.1. Typically, the increase in shear strength is less than proportional to the nominal contact pressure.

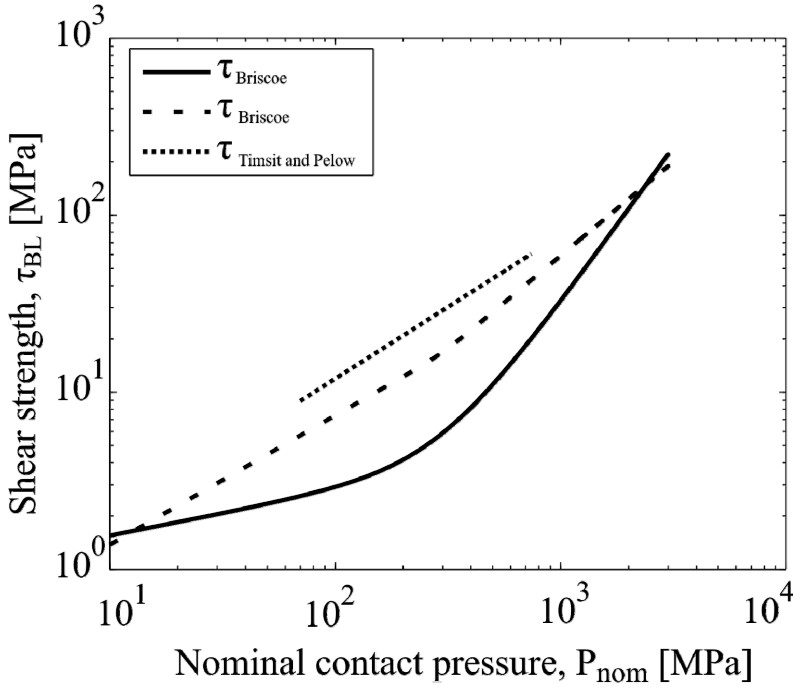

Figure 3.1: Boundary layer shear strength models, [18]

The influence of temperature is studied by Briscoe et al. [60] and [62] on the shear strength of the boundary layers. The lubricating property of the boundary layers is found to degrade with the increase in temperature for stearic acid type of lubricants adsorbed on glass. The boundary layer breaks and opens the contact between the metallic surfaces in contact. This causes the coefficient of friction to increase due to local lubricant failures.

The influence of sliding velocity on shear properties of the boundary layers is studied by Briscoe et al. [60] and [63]. The influence of sliding velocity is different for the type of lubricant used. According to Briscoe et al. there are two physical phenomena responsible for the dependence of shear strength on sliding velocity. Firstly, the strain rate in the boundary film over its thickness influences the shear strength, $\tau = \eta U/h$. The shear strength of the boundary layers increases as the sliding velocity increases. The second effect is due to the visco-elastic behaviour of lubricant. The lubricant layers require some time to respond to the applied normal load. When the visco-elastic effect is larger, the real load carried by the monolayers is smaller than the applied load. This decreases the shear strength of the boundary layers.

The shear strength of the boundary layers is dependent on the number of monolayers built-up on the surface. Briscoe et al. [64] measured the influence of number of monolayers for stearic acid type lubricants. It is found that the increase of number of monolayers decreases the shear strength of the interface.

Westeneng [18] gave a power law fit for the shear strength of boundary layers with nominal contact pressure for the reported experiments in the literature (see Figure 3.1)as follows,

1. Briscoe et al.[62] calcium stearate on glass

$$\tau_{BL} = \left\{ \left(2.56 \cdot 10^{4} P_{nom}^{\ 0.25}\right)^{1.5} + \left(4.18 \cdot 10^{-9} P_{nom}^{\ 1.76}\right)^{1.5} \right\}^{0.67}; \ 10 < P_{nom} < 3000 MPa \tag{3.1}$$

2. Briscoe et al. [62] stearic acid on glass

$$\tau_{BL} = \left\{ \left(10.65 P_{nom}^{\ 0.73}\right)^{30} + \left(0.017 P_{nom}^{\ 1.06}\right)^{30} \right\}^{1/30}; \ 10 < P_{nom} < 3000 MPa \tag{3.2}$$

3. Timsit and Pelow [61] stearic acid on aluminium

$$\tau_{BL} = 3.94 P_{nom}^{\ 0.81}; \ 70 < P_{nom} < 740 MPa \tag{3.3}$$

3.3 Influence of interfacial friction factor

Challen and Oxley's model as described in Section 2.6 is used to calculate the friction due to ploughing, along with the influence of boundary layers. The model consists of two important parameters to calculate the coefficient of friction – the attack angle, β, and the interfacial friction factor due to boundary layers, f_{BL}. The interfacial friction factor ($f_{BL} = \tau_{BL}/k$), is the ratio of shear strength of the boundary layers to the shear strength of the deforming material. Based on the attack angle and friction factor, there are three different modes of deformation as shown in Figure 3.2.

In the case of lower attack angles and well lubricated conditions ($\beta < 45°$ and $f_{BL} < 0.5$), ploughing occurs. In case of larger attack angles ($\beta > 45°$), cutting will occur. The wear process of the interfaces will take place, where a degradation of lubricant quality occurs ($f_{BL} > 0.5$). When the shear strength of the boundary layers is independent of hardness of the deforming material, the coefficient of friction reduces (since, $k \approx H/(3\sqrt{3})$). In sheet metal forming, any of the discussed modes of deformation can happen at the asperity scale. The attack angle may vary, depending on the penetration of the tool asperities. At the very local contact conditions of the asperity, the lubricant may fail to adhere to the surfaces. Lubricant may fail due to high flash temperatures or rupture due to high contact pressure and sliding conditions. The coefficient of friction will be influenced by these factors if operating in the boundary lubrication regime.

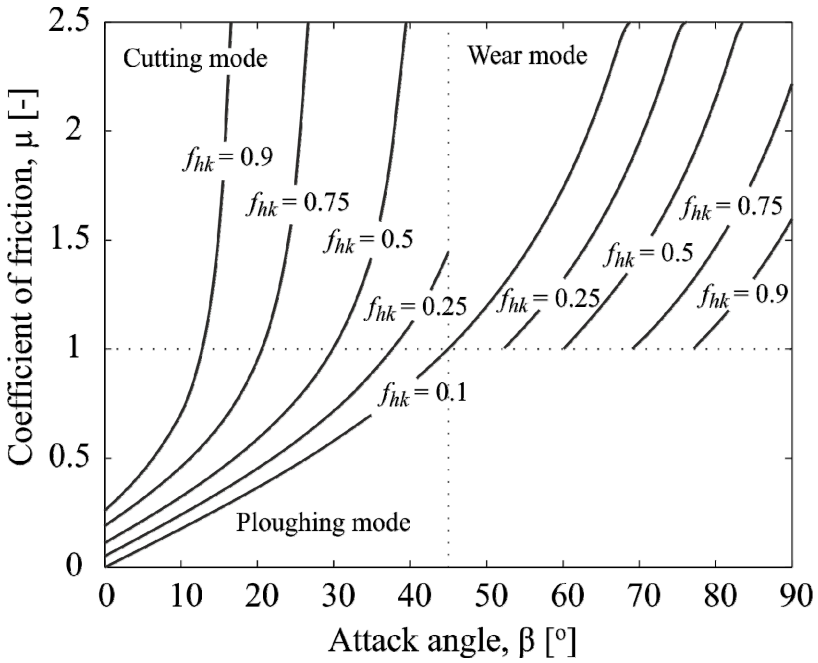

Figure 3.2: Influence of friction factor with Challen and Oxley friction model [10].

3.4 Experimental determination of friction factor for the BL model

The empirical models available in literature do not apply for the metal-lubricant combination in the deep drawing processes. Hence the aim of the present investigation is to find the shear strength of the boundary layers formed by the lubricant Quaker N6130 between hardened tool steel and DC06 high formable steel. Quaker N6130 is a common oil used in deep drawing for lubrication as well as for conservation against corrosion. The shear strength is investigated as a function of contact pressure and lubrication amount at constant sliding velocity. The frictional force is measured during sliding of a cylindrical pin (100Cr6 bearing steel) over DC06 sheet material. Experiments have been performed at room temperature. The boundary layer shear strength is obtained from the measured friction force and the calculated contact area, which follows from the Hertz contact theory.

A linear sliding friction tester (shown in Figure 3.3 (a)) is used to study the dependence of nominal contact pressure and lubrication amount on the shear strength. The friction tester has a XY linear positioning stage driven separately by actuators. The loading tip is supported in a horizontal beam with a linear actuator for the z-stage and a piezo sensor/actuator. The coarse displacement in the z-direction is carried out by the linear actuator and the fine displacement is controlled by the piezo actuator. The normal force is applied by means of a force controlled piezo actuator in the z-direction. The piezo actuator is connected to a PID control loop feedback system. The friction force is measured by another piezo sensor as shown in Figure 3.3 (b). The normal force and friction force can be measured with a fine precision in a broad range of load. The specification of the friction

tester is given in Table 3.1. The sliding pin is self-aligning with the application of normal load, which provides intact contact with the sheet material during sliding.
The DC06 steel sheet is relatively rough, requiring a polishing process before friction tests to avoid ploughing effects. Polishing provides a complete contact over the width of the sliding pin. This will ensure that the measured friction is primarily caused by the shearing of boundary layers. First, DC06 steel sheet is cut to the required size and glued to a steel block to ensure the flatness of the sheet during polishing. The polishing is done in a rotating disc polisher in three stages with fine grain diamond slurry. Diamond grains of sizes 25 μm, 6 μm and 3 μm are used for polishing in three cycles of 15 minutes. A coarse polishing step with grains of 25 μm size will ensure that the surface is completely flat. The coarse polishing step will remove any sharp edges or major waviness in the surface. The surface is then mirror polished with finer grains. The lubricant Quaker N6130 is applied in a controlled amount on the sheet material by using a mass balance. The friction force is measured over a contact length of 20 mm. A typical friction measurement from the linear sliding friction tester is shown in Figure 3.4. It can be seen that the coefficient of friction decreases as the normal load increases. The variation in the friction measurement appears to be constant within a considerable range of sliding distance for one sliding traverse.

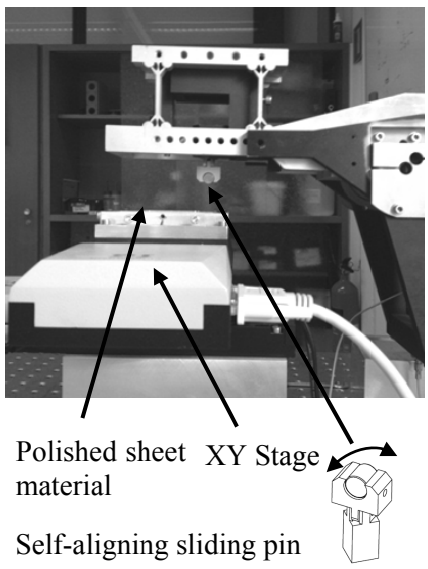

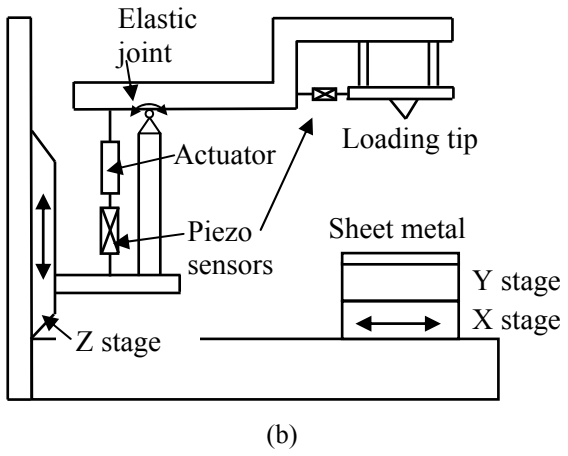

Material specifications	
Radius of the pin	5 mm
Roughness of the pin	120 nm
Roughness of the sample	5~10 nm
Controlled lubricant amount	0.6-2.0 g/m^2 ± 0.1

Figure 3.3: (a) Linear sliding friction tester and (b) Schematic representation of friction tester.

In Figure 3.5, the surface profile of the sliding pin and the polished DC06 sheet material before and after sliding test are shown. The surface of the polished sheet after sliding can be seen with some light scratches and there was no transfer of material. It can be assumed that the major contribution of the friction forces arise from the shearing of the boundary layers

and ploughing contributes only a minor part of it. It can also be seen from the surface distributions of the DC06 surface before and after loading (see Figure 3.5 (e and f)) that there is not much change in the surface topography either due to asperity flattening or to dominated ploughing effects, although some minor scratches are evident (see Figure 3.5 (c and d)).

Property	Range	Precision
Normal force	0.1-50 N	5 mN
Friction force	0.1-50 N	5 mN
Sliding velocity	0-50 mm/s	1 µm/s
Sliding stroke length	0-50 mm	1 µm
Vertical stroke (with actuator)	0-50 mm	1 µm
Vertical stroke (with piezo)	0-200 µm	10 nm

Table 3.1: Specifications of the sliding friction tester.

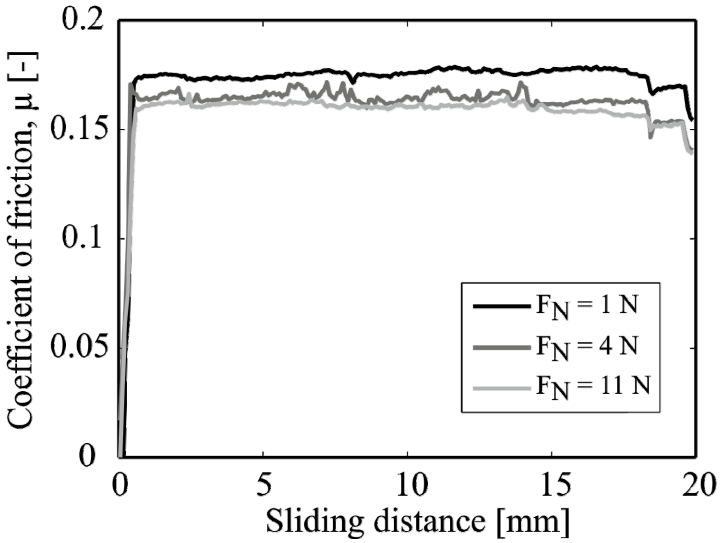

Figure 3.4: Friction measurements with the linear sliding friction tester apparatus for normal loads, F_N = 1, 4 and 11 N.

The repeatability of the friction measurements within the same track is measured as shown in Figure 3.6. For the first four traverses, there was no significant difference in the coefficient of friction and it started to increase afterwards. This is due to the removal of the lubricant from the contact due to the repeated traverses. The durability of the boundary layer degrades after repeated traverses. The mechanism behind the degradation of the boundary layers is not analysed within this research. However, in this case the increase in friction could be due to a limited supply of the lubricant in the contact. The lubricant adherence is well conserved during the first traverse which is important for the friction measurements.

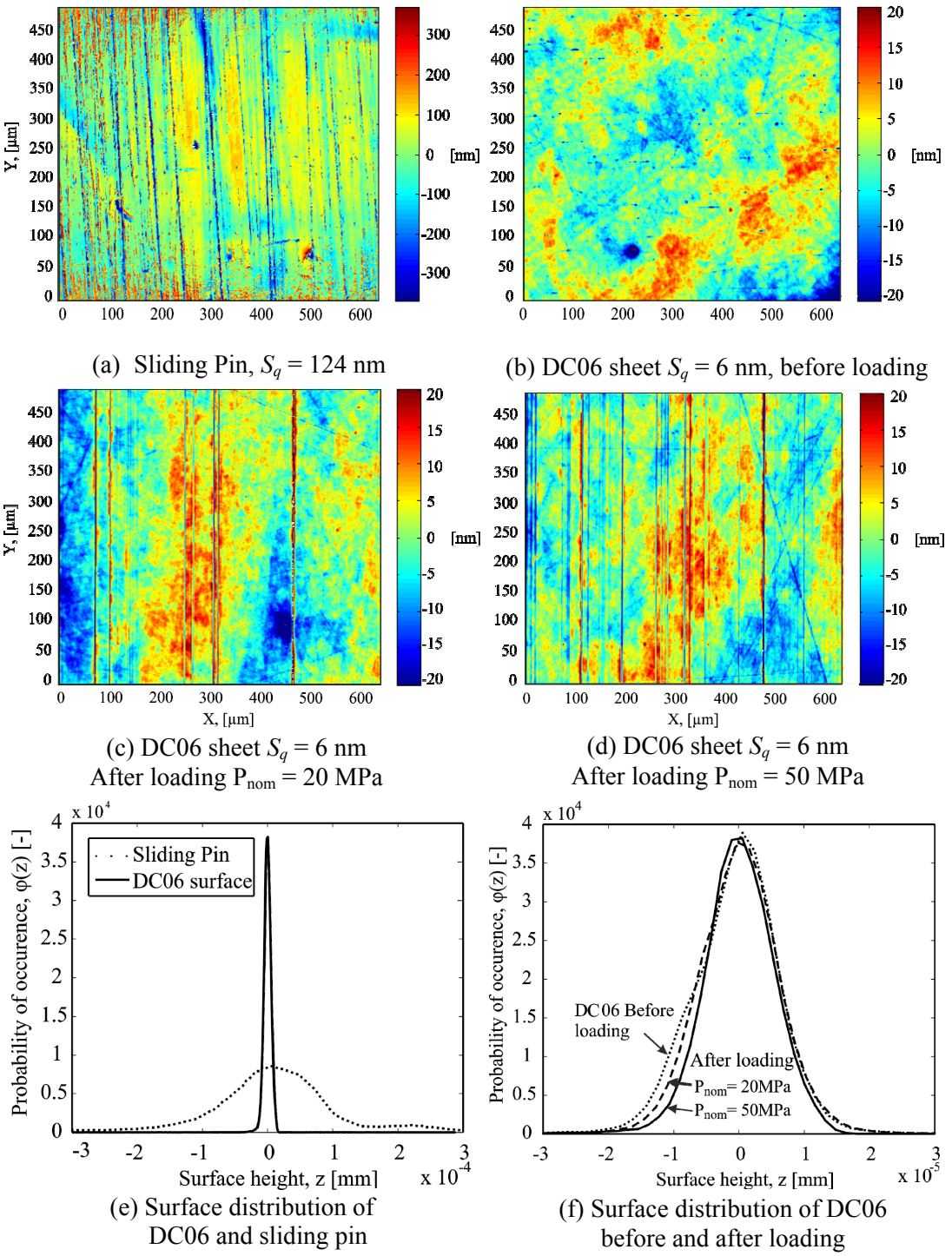

(a) Sliding Pin, S_q = 124 nm

(b) DC06 sheet S_q = 6 nm, before loading

(c) DC06 sheet S_q = 6 nm
After loading P_{nom} = 20 MPa

(d) DC06 sheet S_q = 6 nm
After loading P_{nom} = 50 MPa

(e) Surface distribution of DC06 and sliding pin

(f) Surface distribution of DC06 before and after loading

Figure 3.5: Surface topography of the sliding pin and polished DC06 sheet.

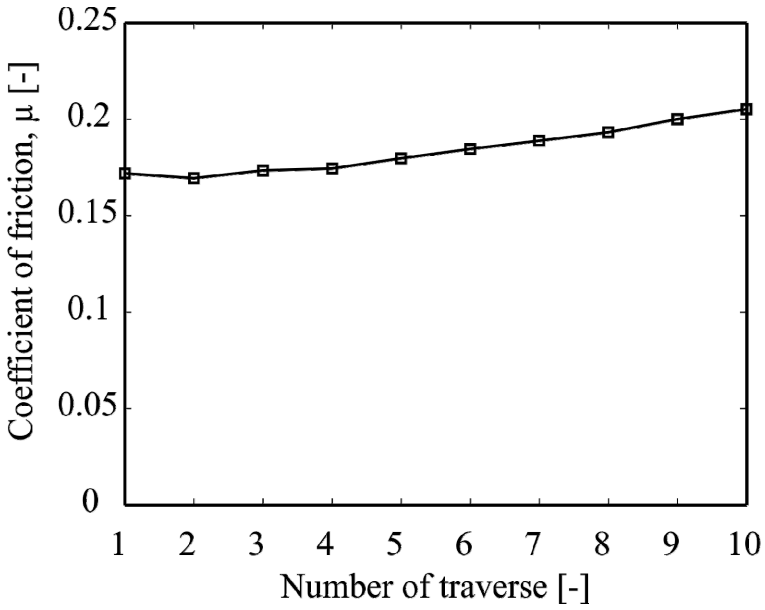

Figure 3.6: Repeated sliding traverses at nominal pressure, P_{nom}= 20 MPa and sliding velocity, U= 1 mm/s.

In sheet metal forming operations, generally the lubrication amount is controlled. The amount of lubrication on the sheet material is maintained at between 0.6 and 2.0 g/m^2 which are the typical standards used in automotive industries. In the current study, the standards are followed within an accuracy of +/- 0.1g/m^2. The influence of the contact stress and the lubrication amount is studied on the shear strength at a constant sliding velocity of 1 mm/s. The friction force, F_w is measured for a sliding distance of 20 mm. The contact area, A_{nom}, is calculated for the Hertzian line contact between a cylindrical pin and a flat as given in Appendix D. The shear strength of the boundary layers, τ_{BL}(= F_w/A_{nom}), is calculated for a sliding distance of 14 mm to neglect the initial static friction and tail end of the sliding measurements. The influence of the lubrication amount and the nominal pressure is shown in Figure 3.7. The error bar is calculated from the standard deviation of the three different sliding traverses on the sheet metal surface. The sliding pin was cleaned with acetone and alcohol after each traverse. The increase in shear strength is less than proportional to the nominal contact pressure as reported in [60] and [61]. From the measurements, it can be seen that the amount of lubrication hardly influences the boundary layer shear strength. The empirical fit for the boundary layer model from Timsit and Pelow [61] varies marginally with the current experiments especially at lower nominal pressure. From the shear strength experiments, it can be concluded that the shear strength is dependent on the nominal pressure. The lubrication amount does not affect the shear strength of the boundary layers.

Timsit and Pelow [61] proposed a power law ($\tau_{BL} = cP_{nom}^{\ n}$ with c = 3.94, n = 0.81) for the boundary layer shear strength for stearic acid on aluminium and glass for a pressure range of 70-740 MPa. Results from Timsit and Pelow are extrapolated to the pressure range in the experiments. Though the model is derived for other metal-lubricant combinations and slightly higher pressure ranges, the results vary marginally from the experiments. The same

relation from Timsit and Pelow can be modified with c=0.96 and n=0.88 as shown in Figure 3.7. The trend might be extrapolated to other pressure ranges, but additional experiments are required.

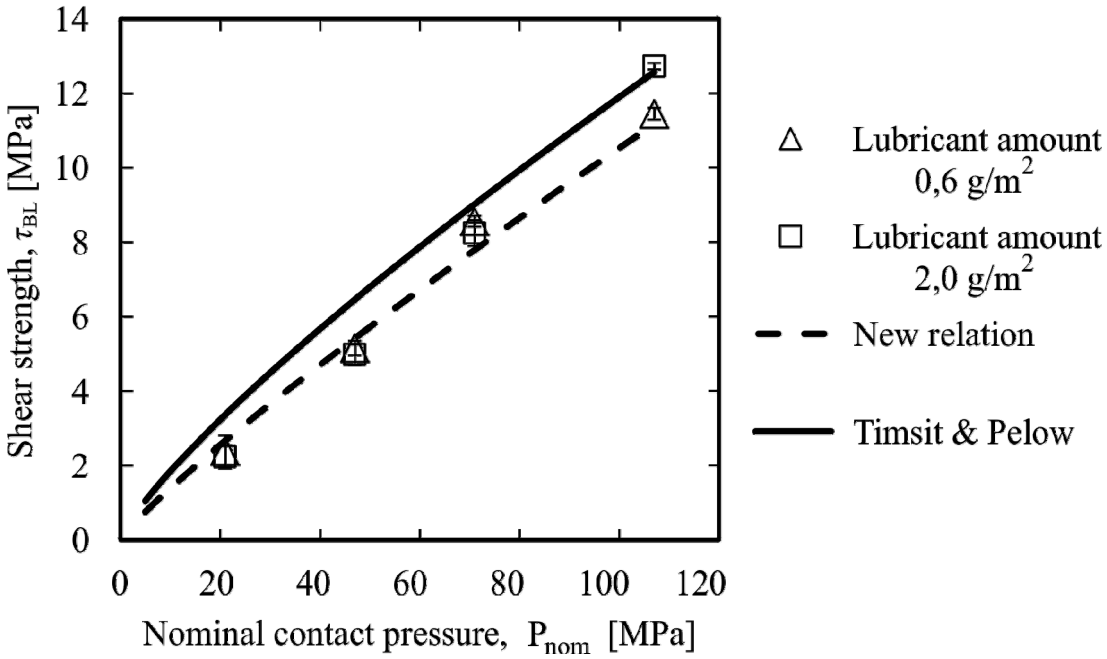

Figure 3.7: Boundary layer shear strength measurements.

3.5 Influence of real contact area on interfacial shear strength

Timsit and Pelow performed their experiments between aluminium and a glass slider with stearic acid type monolayers at the interface. The experiments were performed to shear only the boundary layers not the bulk material. In order to calculate the boundary layer shear strength, they used the contact area from the Hertz contact theory assuming that the surfaces are smooth. However, in reality only a few asperities of the surface will be in contact. Timsit and Pelow also reported that there is some degree of penetration of the glass slider surface asperities on the aluminium material. Through EDX spectroscopy they confirmed a small transfer of aluminium on the slider material. These findings show that the contact occurs only at a discrete area even when the contact occurs with very smooth surfaces like glass or mica.

The metal-metal adhesion occurs at these discrete contact spots and increases the effective shear strength at the interface. The lubricant at the interface fails due to flash temperature caused by frictional heating or high compressive stresses in the contact zone, which considerably decreases the effectiveness of the boundary lubrication. It can be concluded that calculation of shear strength from the Hertz contact area underestimates the shear strength of the contact interface. However, finding the real contact area through experiments is difficult. The Boundary Element Method (BEM) can be used to calculate the

real contact area with given rough surfaces. To verify the BEM, the contact area and pressure are found for a smooth cylinder against a flat surface. The calculated real contact area and mean contact pressure are compared with the Hertz contact theory as shown in Figure D.2 (see Appendix D).
The mean contact pressure is calculated for different radii of the pin with a normal load of F_N = 1 N as shown in Figure D.2 (a). The mean contact pressure decreases in line with the increase of the cylinder size for the same load which is due to the increase of contact area as shown in Figure D.2 (b). The BEM calculation is in accordance with the Hertz contact theory for a smooth cylinder. The influence of surface roughness on the real area of contact is now considered. Cylinders of different surface roughness are generated numerically using the FFT techniques of Hu and Tonder [65]. The influence of surface roughness on the contact area between a cylinder and flat for a given normal load of F_N = 1 N is shown in Figure 3.8.

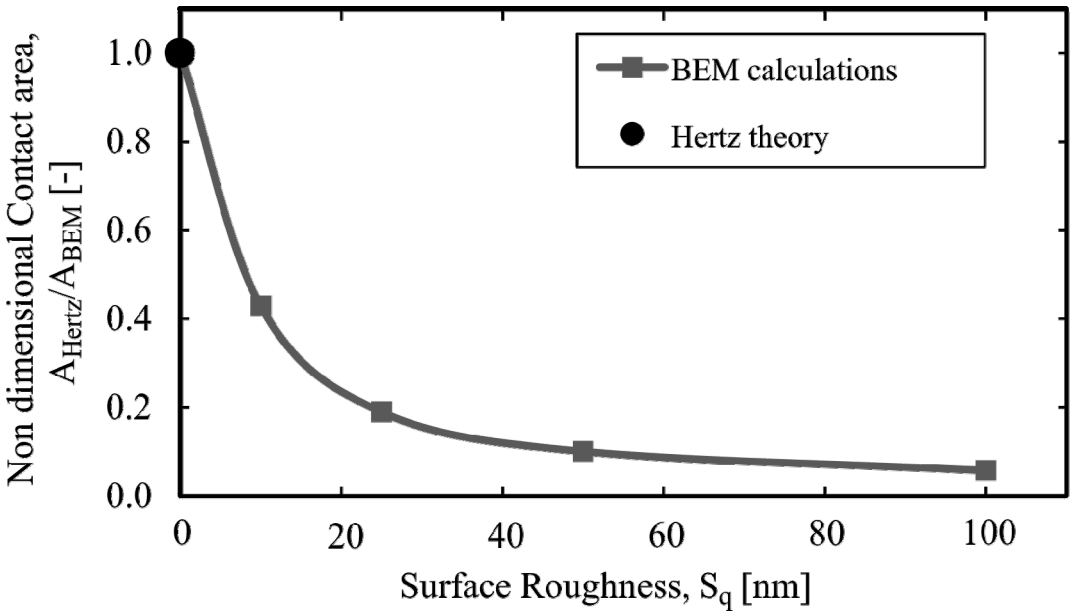

Figure 3.8: Influence of surface on real area of contact.

When the cylinder is smooth, there is no difference in the real contact area between Hertz and BEM contact theories as already shown in the validation process (see Appendix D). Figure 3.8 shows the contact area from BEM contact calculations normalized by the Hertz contact area for smooth cylinder and flat. The real contact area for the same loading conditions decreases as cylinder's surface roughness increases. There is a huge decrease of real contact area as roughness changes from a smooth cylinder to a rough cylinder of 20 nm. In that case, the real contact area gradually decreases with the increase of surface roughness. This shows that contact occurs only at discrete spots and it is much dependent on the surface roughness. The calculation of interfacial shear strength with the Hertz contact theory is inappropriate. In Figure 3.9, the influence of the real contact area on the interfacial friction factor is shown. With the Hertz contact theory, the friction factor is of the same order of magnitude as Timsit and Pelow's relation. However, if the real contact

area calculated from the BEM calculation is used, the friction factor is quite high. The surfaces used for the calculation are obtained from the pin and the flat specimen used in the experiments as shown in Figure 3.5 (a) and (b). The calculated real contact area is shown in Figure 3.10 (a) and (b). A comparison for the real contact area is shown in Figure 3.11 for the calculations from the Hertz contact theory and BEM calculation using the measured surfaces of pin and polished DC06 sheet material surface. The contact area from BEM calculations is lower than the Hertz theory and also increases as the nominal contact pressure increases.

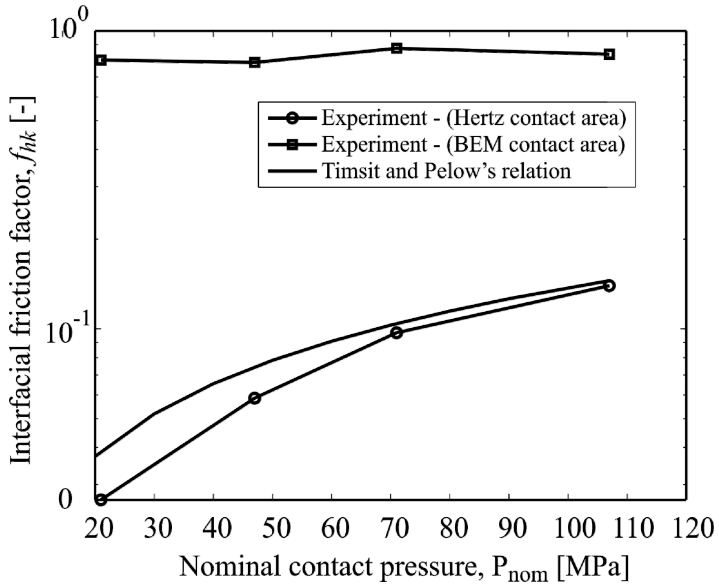

Figure 3.9: Influence of real contact area on friction factor.

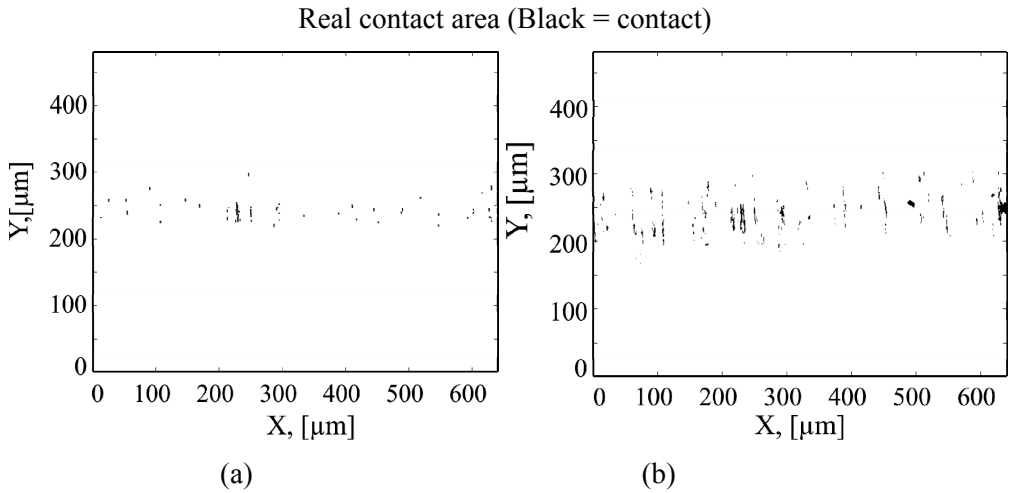

Figure 3.10: Calculated real contact area with the BEM contact theory for nominal contact pressure of (a) P_{nom} = 20 MPa and (b) P_{nom} = 50MPa.

For lower contact pressures, there are only a few asperities in contact and the real contact area increases with the increase in contact pressure. It can be seen that there is a qualitative agreement between the contact area from the measured surfaces after deformation (see Figure 3.5 (c) and (d)) and the calculated real contact area using BEM calculations (see Figure 3.10 (a) and (b)).

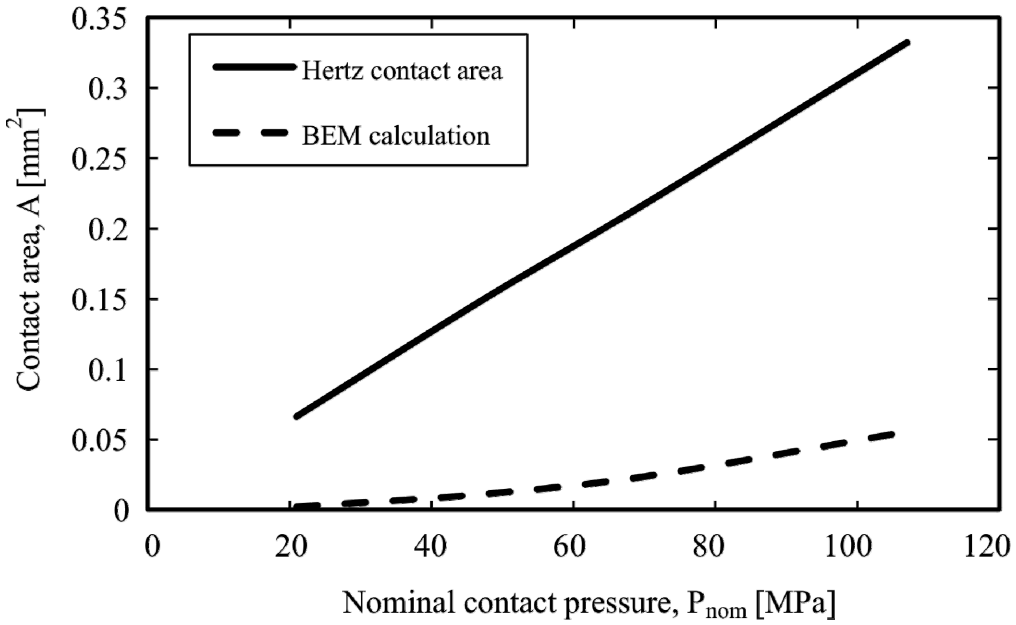

Figure 3.11: Comparison for the contact area calculated from the Hertz contact theory and BEM calculations.

From these calculations, it can be seen that the real contact area influences the shear strength of the boundary layers. The calculation of the shear strength using the Hertz contact area underestimates the friction at the local conditions. For the friction models, it is essential to use the local interfacial shear strength while calculating the coefficient of friction from the micro-mechanisms. It can also be seen that the friction factor is almost constant when using the real contact area as shown in Figure 3.10. The friction factor from these measurements is between 0.7 and 0.9. The Hertz and BEM contact calculations are for static contact situations. There would be an influence of sliding on the real contact area. Ovcharenko et al. [66] studied the junction growth of metals during the sliding and static contact conditions of a single asperity. During sliding, there was an increased contact area due to the additional tangential stresses. It is found that the junction growth of the contact increases as the normal load increase. The increase in real contact area ranges between a factor of 1.0 and 1.4 for low and very high normal loads respectively. The increase of contact area during sliding will also reduce the friction factor to some extent.

3.6 Summary

In this chapter, a summary of boundary layer friction models from the literature is presented. The influence of the interfacial friction factor on the coefficient of friction is shown with Challen and Oxley's model. In literature, shear strength experiments were done mostly on materials other than steel. Therefore, experiments were performed on the steel-steel contact with a typical lubricant, Quaker N6130 used in deep drawing processes. The boundary layer shear strength is calculated from the measured friction forces and the contact area from the Hertz theory. It has been shown that the experiments were of the same order of magnitude as Timsit and Pelow's experiments. However, in reality the Hertz contact theory is valid for smooth surfaces. The influence of surface roughness on the real contact area is studied with the BEM calculations. It has been shown that the surface roughness gives a large difference in the real contact area between Hertz theory and BEM calculations. Further, BEM calculations are done to calculate the real contact area for the surfaces used in the experiments. A comparison is shown of how the real contact area influences the friction factor.

Chapter 4
MODELLING MIXED LUBRICATION FOR DEEP DRAWING PROCESSES

4.1 Introduction

Lubricants are often used in the deep drawing processes. Typically, lubricant is applied all over the blank which is then pressed. In tool-sheet material contact situations, the lubricant is retained in the blank holder and punch rounding regions. The retained lubricant chemically or physically bonds to the surface of the tool and sheet material governing the friction value at the solid contacting asperities. If the lubricant amount is sufficient to fill the valleys of the rough surface, under the right conditions it can build up hydrodynamic pressure due to the applied pressure and sliding of sheet material. In that case, the development of real contact area is hindered by the lubricant pressure generated in the valleys. The pressure carried by both the asperities and the lubricant need to be taken into account in the friction model. The lubricant pressure generation is dependent on sliding conditions, lubricant properties and surface features such as roughness and lay.
In literature, most of the lubrication models are applicable for rolling and sliding contacts of gears and bearings where the lubricant film thickness is determined from the inlet conditions such as geometry of the interacting surfaces, lubricant viscosity and operational conditions. However, in a deep drawing process scenario, the tool and sheet material contact is nominally flat. An important contribution of the pressure generation in the contact is expected to originate from the asperity deformation mechanisms. In this chapter, the asperity deformation model of Westeneng [18] is used to describe the sheet material surface deformation due to normal loading and stretching process. The developed mixed lubrication model accounts for the change in film thickness due to asperity deformation.

4.2 Asperity deformation model

Westeneng [18] considered asperities of the sheet material surface as separate bars which rise and flatten to the applied load as shown in Figure 4.1. In the sheet material roughness scale, the workpiece (i.e. sheet material) is considered to be rough and soft. The tool is considered to be flat and hard and it deforms the encountered workpiece asperities. Using the principle of energy conservation and volume conservation, a contact model had been developed by Westeneng [18] to explain the flattening of the asperities. In this model, it is assumed that the asperities which are not in contact with the tool rise uniformly. A part of external applied energy is used to flatten the asperities, to raise the valleys and also to retain

the asperities which come into contact with the tool during flattening process. The asperities flatten due to applied normal loading and also due to stretching (i.e. bulk strain).

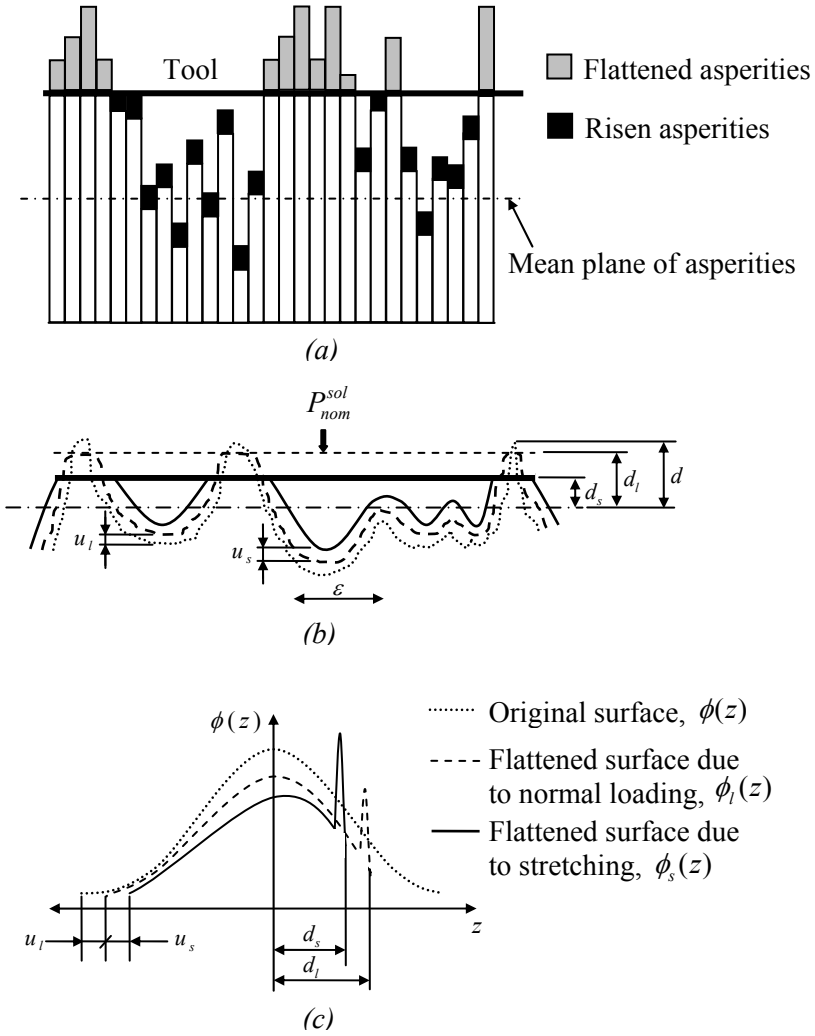

Figure 4.1: (a) Representation of asperity flattening and rising model (b) Asperity flattening and rising process during surface deformation process (c) Change of surface distribution during deformation process.

4.2.1 Asperity flattening due to normal loading

In Westeneng's model, the workpiece material is assumed to deform under ideal plastic conditions. The total work done is divided into two parts – work done on asperity to flatten and workdone to raise the asperity. The asperities which are not in contact are assumed to

rise. Asperity persistence is also included in the model, which determines the amount of energy needed to lift up the asperities.

$$W_{applied} = W_{flat} + W_{rise} \tag{4.1}$$

By using the probability density distribution of the asperity heights, $\phi(z)$, the fractional contact area, α, developed during normal loading and stretching of the workpiece is calculated as shown in Equations (4.2)-(4.9).
After normal loading of the workpiece, the asperities which are in contact are flattened and the separation between the flat tool and mean plane of the workpiece is reduced to d_l from d as shown in Figure 4.1 (a and b). The asperities which are not in contact rise by an amount of u_l. The fractional contact area for normal loading is found from the probability density of the surface as given in Equation (4.2).

$$\alpha_l = \int_{d_l - u_l}^{\infty} \phi(z) dz \tag{4.2}$$

The nominal pressure, $\left(P_{nom}^{sol} = F_N^{sol} / A_{nom}\right)$, carried by the asperities alone which are in contact under ideal plastic deforming conditions is given in Equation (4.3).

$$\frac{P_{nom}^{sol}}{H} = \xi \left(1 + \eta \chi \int_{d_l}^{\infty} \phi(z) dz \right) \tag{4.3}$$

The nominal pressure carried by the solid contact depends on the material hardness, surface distribution function and separation between tool and workpiece during normal loading. The expressions for the functions ξ and χ can be found in Appendix E. The detailed derivations of these expressions are given in [18] and [67].
Equation (4.4) gives the rise of the asperities for a given separation distance using the volume conservation principle.

$$u_l (1 - \alpha_l) = \int_{d_l - u_l}^{\infty} (z - d_l) \phi(z) dz \tag{4.4}$$

The parameter η is the asperity persistence parameter. The parameter $\eta = 0$ means no work is done to cause the rise of valleys. The parameter $\eta = 1$ means that maximum amount of work is done to cause the rise of the valleys.
The unknown variables are fractional contact area, the amount of flattening, d_l, and the amount of rising, u_l, which are calculated by simultaneously solving the Equations (4.2)-(4.4).

4.2.2 Asperity flattening due to bulk deformation

When a soft material in contact is subjected to bulk deformation, surface topography change will occur. During bulk deformation, the sheet material becomes softer and more deformation occurs with normal loading. Assuming the asperity to be like wedges, Wilson and Sheu [24] and Sutcliffe [25] presented asperity flattening models for plane stress and plane strain conditions using the upper bound and slipline methods respectively as explained in Chapter 2.

The fractional contact area as given in Equation (4.7) due to bulk strain is calculated from the probability density of the surface after normal loading. During bulk straining of the workpiece, the effective hardness is substantially reduced which causes further flattening of the workpiece asperities by the tool. Generally, the effective hardness is the ratio of hardness to the shear strength of the material. For pure plastic conditions, the hardness is the real pressure in the contact.

$$H_{eff} = \frac{P_{real}}{k} \tag{4.5}$$

When bulk strain occurs, the real contact area increases. Hence the contact pressure also decreases and the effective hardness during bulk straining is given as,

$$H_{eff} = \frac{P_{nom}}{\alpha_s k} \tag{4.6}$$

The fractional contact area due to stretching is given as,

$$\alpha_s = \int_{d_s - u_s}^{\infty} \phi_l(z) dz \tag{4.7}$$

The asperity flattening rate due to bulk strain in the workpiece for a single asperity is given by Equation (4.8). The non dimensional strain rate E (see Section 2.4.2.1) is described for a plane stress deformation mode in the asperities from the work of Sutcliffe [68] as,

$$\frac{d\alpha_s}{d\varepsilon} = \frac{l_a}{E} \phi_l(z)(d_s - u_s) \tag{4.8}$$

The rise of the valleys due to stretching at a given separation level is described as,

$$u_s(1-\alpha_s) = \int_{d_s - u_s}^{\infty} (z - d_s)\phi_l(z) dz \tag{4.9}$$

The fractional contact area evolution is found by incrementally increasing the strain with Equation (4.8). The fractional contact area, separation and rise of asperities are found by simultaneously solving the Equations (4.7)-(4.9). In Figure 4.2, the development of the real contact area is shown for different nominal pressures as a function of the strain. With the increase in nominal pressure and strain, the fractional contact area increases. The numerical procedure for the asperity deformation model under normal loading and stretching can be seen in Appendix E. The derivation and the FE implementation of the friction model based on this asperity deformation model are explained in detail by [67] with its application to a deep drawing product.

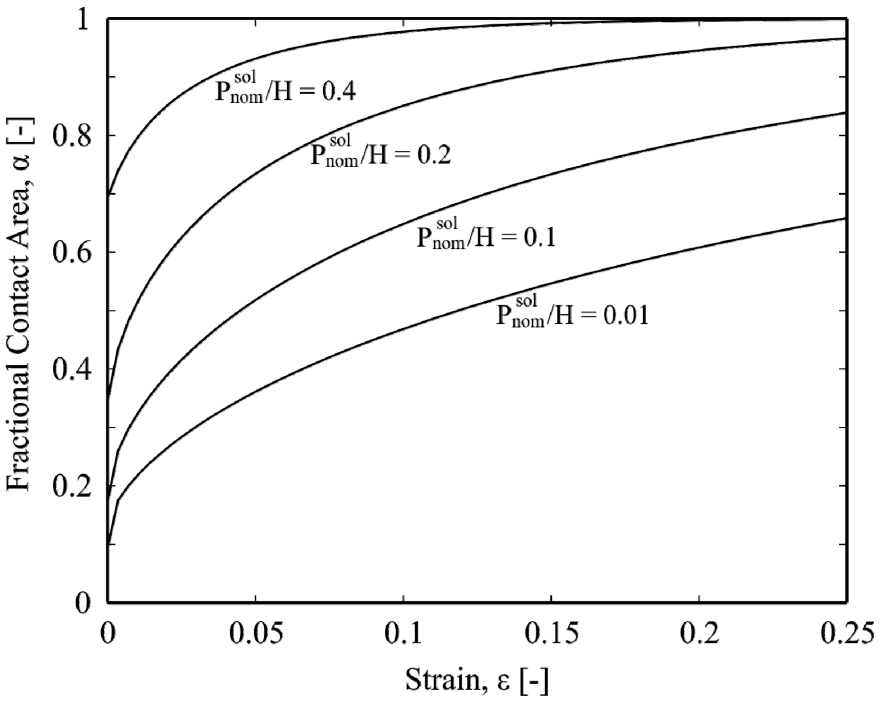

Figure 4.2: Fractional contact area with nominal pressure and strain.

4.3 Mixed lubrication modelling

In the mixed lubrication contacts, the total applied load is shared between the load carried by the contacting asperities and the load carried by the lubricant as a result of pressure generated between the contacts due to hydrodynamic lubrication. The load balance as shown in Figure 4.3 (b) is given by

$$F_N = F_N^{sol} + F_N^{\text{lub}} \tag{4.10}$$

where, F_N - Total applied normal load, [N]
F_N^{sol} - Total load carried by the contacting asperities, [N]
F_N^{lub} - Total load carried by the lubricant, [N]

The fraction of the load carried by the lubricant is dependent on the lubricant properties, the operating conditions and the film thickness. Mixed lubrication can potentially occur in the blank holder region of a deep drawing process. In the blank holder, the sheet slides over the stationary tool under a normal loading and is stretched by the punch action as shown in Figure 4.3 (a).

For a simple deep drawing process, the workpiece is in contact with the blank holder and drawn into the die in radial direction (i.e from $x = 0$ to $x = l$ as shown in Figure 4.3 (a)). The major sliding velocity in this direction contributes to the hydrodynamic flow of the lubricant. A converging wedge of the fluid is formed in the case of increasing strain or

contact pressure over the contact length as shown in the Figure 4.3 (c) due to the asperity flattening mechanism which was explained in Section 4.2. The asperity gets flattened due to normal loading and stretching. Note that the thinning and thickening of the sheet occurring due to the forming process is not taken into account in the film thickness formulation. There are no macro oil pockets or wedges considered which will contribute to the hydrostatic pressure generation.

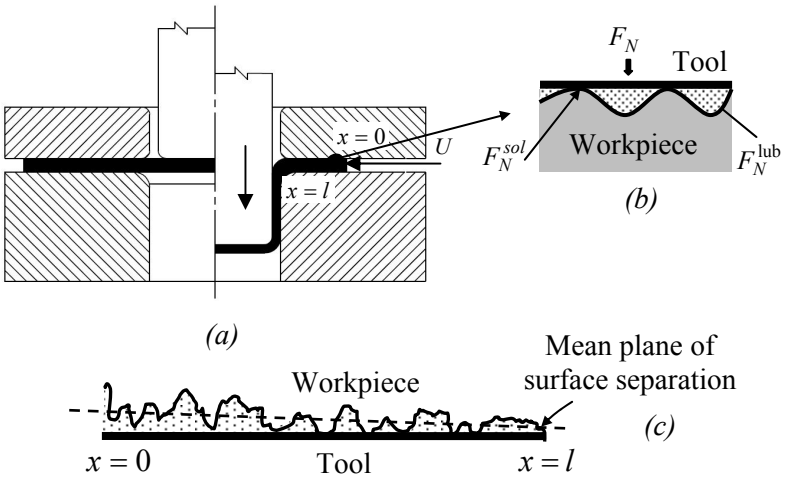

Figure 4.3: Mixed Lubrication in Deep drawing process.

The lubricant flow between the tool and workpiece is treated as a 1D flow across the major sliding direction to find the lubricant pressure share. The general 1D Reynolds equation (RE) is used to describe the flow between the tool and the sheet material. Neglecting the squeeze effect of the fluid, the 1D RE is given as

$$\frac{\partial}{\partial x}\left(\frac{{h_{\text{lub}}}^3}{12\eta_{\text{lub}}}\frac{\partial P_{nom}^{\text{lub}}}{\partial x}\right)=\frac{U_1+U_2}{2}\frac{\partial h_{\text{lub}}}{\partial x}+\frac{h_{\text{lub}}}{2}\frac{\partial(U_1+U_2)}{\partial x} \tag{4.11}$$

Since the tool is stationary, $U_2 = 0$, Equation (4.11) becomes

$$\frac{\partial}{\partial x}\left(\frac{{h_{\text{lub}}}^3}{12\eta_{\text{lub}}}\frac{\partial P_{nom}^{\text{lub}}}{\partial x}\right)=\frac{U_1}{2}\frac{\partial h_{\text{lub}}}{\partial x}+\frac{h_{\text{lub}}}{2}\frac{\partial(U_1)}{\partial x} \tag{4.12}$$

In finite element calculations, the velocity of the sheet due to stretching (i.e. bulk straining) is readily available and can be used as an input to the ML model. Neglecting the stretching effects for simplicity, Equation (4.12) can be further simplified to,

$$\frac{\partial}{\partial x}\left(\frac{{h_{\text{lub}}}^3}{12\eta_{\text{lub}}}\frac{\partial P_{nom}^{\text{lub}}}{\partial x}\right)=\frac{U}{2}\frac{\partial h_{\text{lub}}}{\partial x} \tag{4.13}$$

If the average flow rate along the contact length is Q, then Equation (4.13) after integration is given as

$$\frac{\partial P_{nom}^{\text{lub}}}{\partial x} = \left(\frac{U}{2} h_{\text{lub}} - Q\right) \cdot \left(\frac{12\eta_{\text{lub}}}{h_{\text{lub}}^{3}}\right) \tag{4.14}$$

With the known viscosity of the lubricant, the unknown variables in Equation (4.14) are the film thickness h_{lub} and the flow rate Q.
The film thickness is found from the asperity deformation model (explained in Section 4.2) after normal loading and stretching processes. The film thickness at each discretized point is calculated. The flattening and rising of the asperities are reflected in the film thickness calculation, as shown in Figure 4.4.

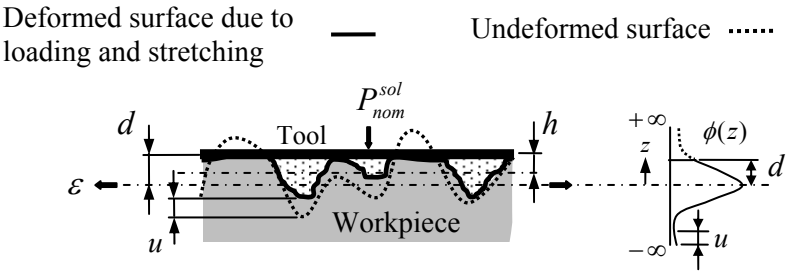

Figure 4.4: Fluid film thickness calculation.

The average film thickness is the ratio of the volume of the fluid below the tool to the area underneath the lubricant film as given in Equation (4.15). The film thickness from the probability density function of the workpiece surface is given as

$$h_{\text{lub}} = \frac{\int_{-\infty}^{d-u} (d-u-z)\phi(z)dz}{\int_{-\infty}^{d-u} \phi(z)dz} \tag{4.15}$$

In Equation (4.14), the flow rate Q is unknown. The flow rate can be calculated by an iterative procedure, applying the given boundary conditions. The lubricant pressure distribution is solved by iterating over Q until the following boundary conditions are satisfied:

$$x = 0; x = l,\ P_{nom}^{\text{lub}} = 0,\ \textit{then}\ P_{nom}^{sol} = P_{nom} \tag{4.16}$$

The boundary condition at $x = 0$ is used as an initial value in the integration of Equation (4.14). With the shooting method as the iterative procedure, the target boundary condition at $x = l$ is achieved within the permissible tolerance by numerically integrating Equation (4.14) for the lubricant pressure. The numerical procedure for the mixed lubrication model integrated with the asperity deformation model is given in Appendix E (see Figure E.1 and Figure E.2). The fractional contact area is calculated by using the resulting pressure available for the solid part, using Westeneng's model [18].

4.4 Friction calculation

To calculate the coefficient of friction in the mixed lubrication region, the shear strength due to the solid contact as well as lubricant part are used. In the solid contact, mechanisms such as the shear of the boundary layer and ploughing are included. In the lubricant part, the shear strength of the lubricant film between the tool and workpiece is included. Ploughing occurs when there is a significant difference in the hardness of the contacting surfaces. The hard asperities plough through the soft material, thereby increasing the friction force. For ploughing, Challen and Oxley's [10] slipline model as shown in Figure 4.5 is used to calculate the frictional stress for multiple tool asperities. Challen and Oxley's model is characterized by the normal load, interfacial shear strength between the tool and workpiece asperity and the attack angle of the tool asperity.

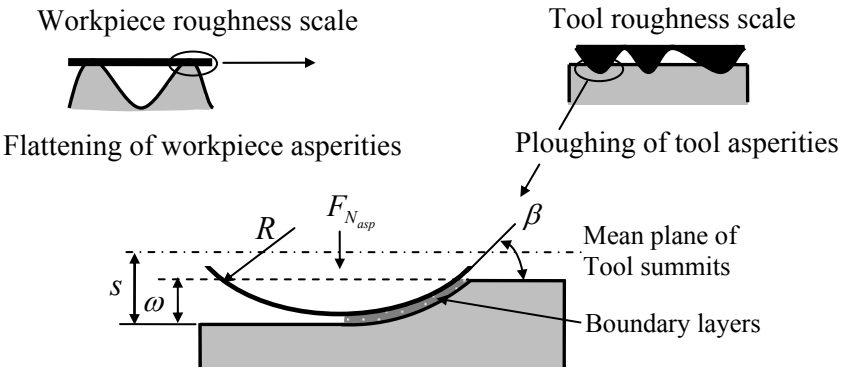

Figure 4.5: Ploughing of tool asperities.

Two levels of surface roughness are considered in this friction model. At the workpiece roughness scale, the smooth tool flattens the rough workpiece as explained in Section 4.2. At the tool roughness scale, the workpiece surface is already flattened and the flattened asperity of workpiece is considered smooth. The tool is considered to be rough at this scale and ploughs through the workpiece. The frictional force due to the solid contact part is modelled from [10] for a single asperity of the tool and extended to the multi-asperity contact from the stochastic variables of the tool surface. The total shear strength caused by the tool asperities for ploughing with boundary layer shear is given as,

$$\tau_{sol} = \rho_t \int F_{W_{asp}} \phi_t(s) ds \tag{4.17}$$

$$F_{W_{asp}} = f_{asp} F_{N_{asp}} \tag{4.18}$$

From Challen and Oxley's model [10], the coefficient of friction for a single asperity contact situation is given as

$$f_{asp} = \frac{B\sin\beta + \cos(\arccos f_{BL} - \beta)}{B\cos\beta + \sin(\arccos f_{BL} - \beta)} \tag{4.19}$$

The normal force acting on the front half of the cylindrical summit for unit width of rough surface under small indentations as shown in Figure 4.5 is given by

$$F_{N_{asp}} = \pi R \omega H \tag{4.20}$$

The friction factor, f_{BL}, at the boundary layer of the asperities is used from Timsit and Pelow [61]. Timsit and Pelow gave the relation for the shear strength of stearic acid type lubricants as a function of the contact pressure. During ploughing, the contact pressure equals the effective hardness of the softer material since ideal plasticity is assumed. The relation of shear strength and effective hardness due to bulk deformation is given in Equation (4.21). With the Timsit and Pelow's shear strength relation, the friction at the boundary layer is given in Equation (4.22).

$$k \approx H_{eff} \,/ 3\sqrt{3} \tag{4.21}$$

$$f_{BL} = \frac{\tau_{BL}}{k} = \frac{3.94 P_{nom}^{0.81}}{k} = 20.47 H_{eff}^{-0.19} \tag{4.22}$$

The shear stress in the lubricant film is calculated using the film thickness (as explained in Section 4.3), the sliding velocity and the lubricant viscosity (assuming a Newtonian fluid).

$$\tau_{\text{lub}} = \frac{\eta_{\text{lub}} U}{h_{\text{lub}}} \tag{4.23}$$

The friction value for the mixed lubricated contact calculated from the shear strength of the solid and the lubricant part is given by

$$\mu = \frac{\alpha_s \tau_{sol} + (1 - \alpha_s)\tau_{\text{lub}}}{P_{nom}} \tag{4.24}$$

If n is the number of discretized points for the whole contact length l, the average coefficient of friction is given for the ease of presenting the results.

$$\mu_{ave} = \frac{1}{n} \sum_{i=1}^{n} \frac{\alpha_s^i \tau_{sol}^i + (1 - \alpha_s^i)\tau_{\text{lub}}^i}{P_{nom}^i} \tag{4.25}$$

when $i = 1$, $x = 0$ and $i = n$, $x = l$
The calculation procedure for the complete friction model is shown in Appendix E (see Figure E.1 and Figure E.2).

4.5 Results and Discussion

The results discussed here are obtained using the models described before. The input parameters for the mixed lubrication model and the asperity deformation model are given in Table E.1 and Table E.2 (see Appendix E).

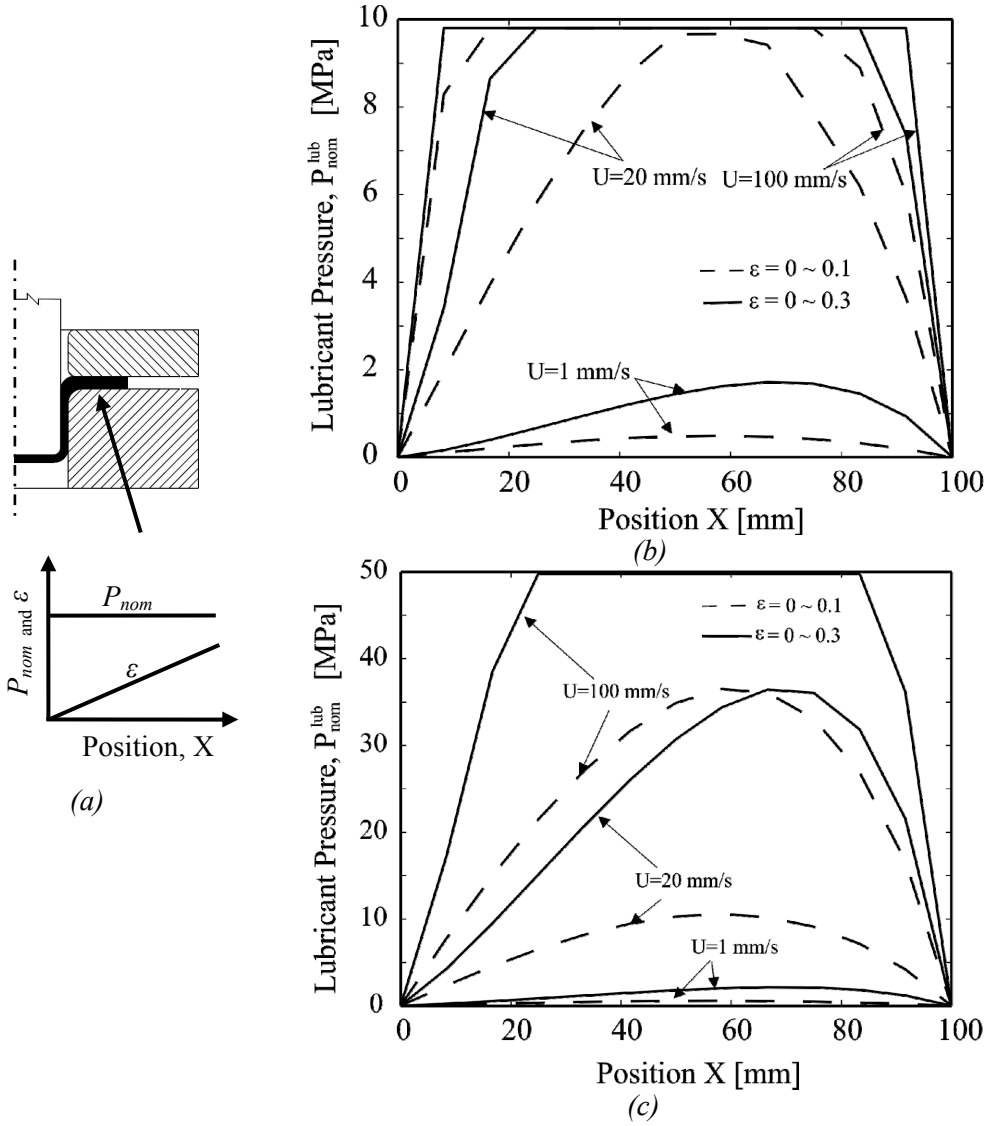

Figure 4.6: (a) Schematic representation of the model problem and lubricant pressure generation for different sliding velocities and strains at nominal blank holder pressures of (b) 10 MPa, (c) 50 MPa.

To understand the friction model in a simple way, the strain is assumed to be increasing linearly along the contact length (representing the blank holder region) in this model problem as shown in Figure 4.6 (a). Further, a constant sliding velocity and a uniform blank holder pressure are used for these model calculations. The lubricant pressure generation for different sliding velocities and blank holder pressure are shown in the Figure 4.6 (b and c). At low sliding velocities, the Couette flow is limited and the lubricant pressure generation is low in comparison with higher sliding velocities. When the strain is increased, the asperity deformation is higher. There is a steeper converging film which results in increased lubricant pressure. The increase of the blank holder pressure also increases the lubricant

pressure generation as shown in Figure 4.6 (c). It can be also be seen that at high sliding velocity (U = 100 mm/s) and strain (ε = 0~0.3), the total applied pressure is carried by the lubricant itself. At high sliding velocity, there is a full film hydrodynamic lubrication. In Figure 4.7, the effect of contact length on the lubricant pressure generation is shown. This illustrates how the pressure generation changes as the contact zone length of the blank holder region decreases during the progress of deep drawing process. The film thickness at the inlet and outlet of the contact zone shown in Figure 4.7 is same for all contact lengths. Hence the film thickness gradient changes with the contact length. The lubricant pressure is shown to increase as the contact length increases.

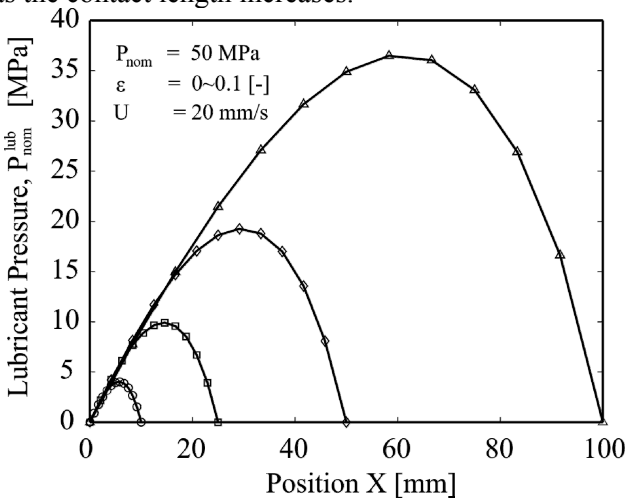

Figure 4.7: Lubricant pressure generation for different contact length.

In Figure 4.8 (a and b), the effect of strain and contact length on the coefficient of friction against the dimensionless lubrication number in the Stribeck curve. The dimensionless lubrication number is given by the following relation according to Schipper [37],

$$L = \frac{\eta_{\text{lub}} U}{P_{nom} R_a} \tag{4.26}$$

In Figure 4.8 (a), the coefficient of friction is shown for a low straining process. The coefficient of friction is high for the shortest contact length because of the lack of lubricant pressure generation as seen in Figure 4.7. For shorter contact lengths, the system is mostly in the boundary lubrication regime and reaches to mixed lubrication regime at high lubrication numbers. For longer contact length, the transition to a mixed lubrication regime occurs at a lower lubrication number. For large deformation processes, the contact pressure and bulk straining is high. The asperity deformation goes higher and under these conditions the transition to different lubrication regimes is quicker when compared with low strain conditions as shown in Figure 4.8 (b). It can be also seen that there is an increase in coefficient of friction at low lubrication numbers. This is due to a higher fractional contact area resulting from the straining process. With the increase of fractional contact area, the number of tool asperities interacting with the workpiece also increases. The solid contact is predominant at low lubrication numbers.

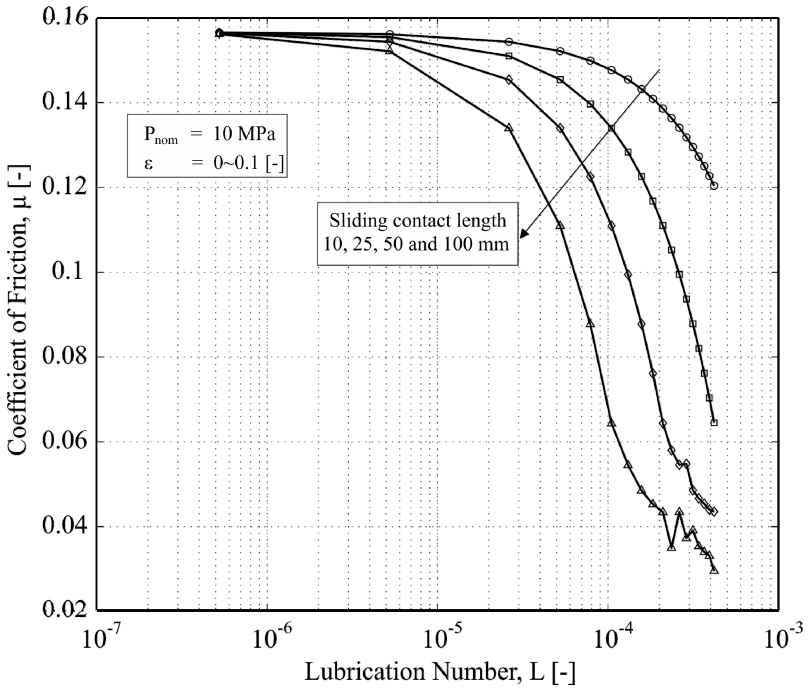

(a)

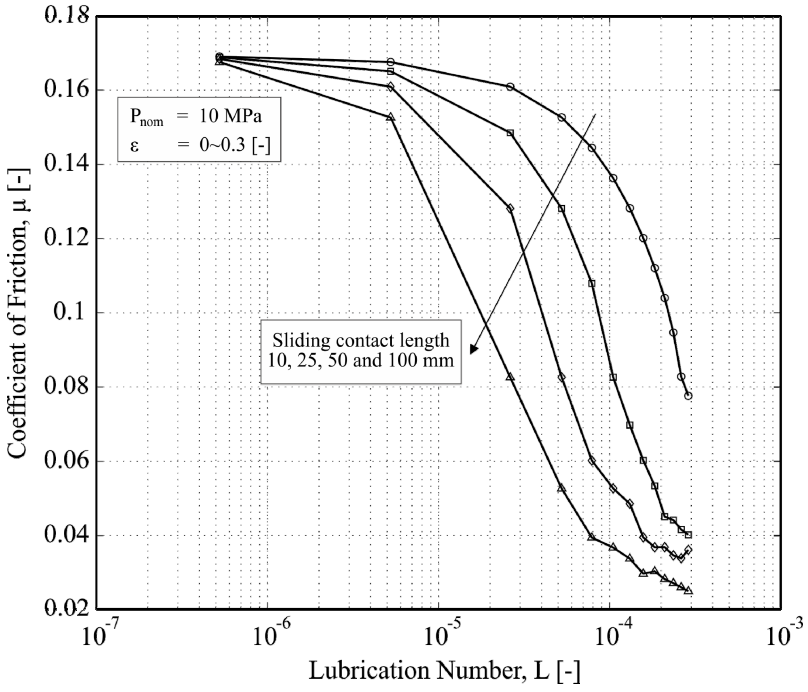

(b)

Figure 4.8: Stribeck Curve showing transition from BL to ML for various strain conditions (a) ε = 0~0.1 and (b) ε = 0~0.3.

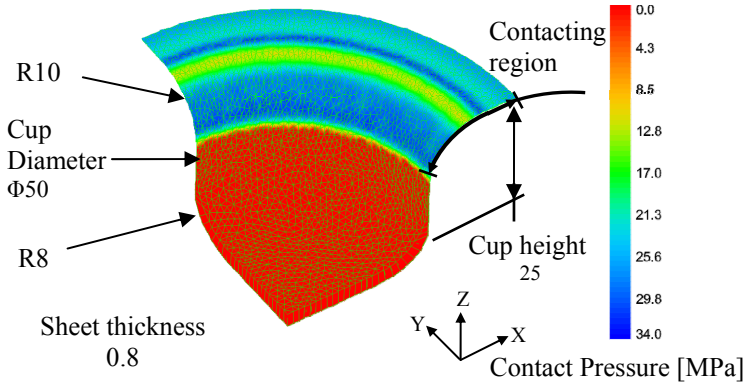

Finite element simulation parameters for sheet material	
Material model	: Elastic plastic Hill 48 (refer [69])
Young's modulus	: 210 GPa
Poisson's ratio	: 0.3
Coefficient of friction (Boundary lubrication)	: 0.16
Cup drawing speed	: 25 mm/s

All dimensions are in *mm*

Figure 4.9: Contact normal stress of cup drawing simulation.

To illustrate the ML model under deep drawing conditions, a simple axi-symmetric cup is considered, as shown in Figure 4.9. The cup drawing is simulated using the FE software DiekA, an in-house Finite Element (FE) code developed at the University of Twente. The cup geometry and the contact normal stress for the cup are shown in Figure 4.9. The input parameters from the FE simulation for the ML and friction model are the blank holder contact pressure, strain and sliding velocity. The calculated friction values are to be used for calculating the shear strength in the contact algorithm in the FE simulation. For this simulation, the friction model is not coupled within the FE framework. The input values are taken from the free edge of the sheet in the blank holder region up to the contacting region in the die round as shown in Figure 4.9 at three different drawing depths. Figure 4.10 shows the nominal contact pressure at the contacting region and the generated lubricant pressure for three different drawing depths. The average fractional contact and average coefficient of friction for a different drawing depth and drawing speed is shown in Table 4.1. The results of the boundary lubrication (BL) and mixed lubrication models are compared in Table 4.1. At the drawing depth of 10 mm (shown in Figure 4.10 (a)), there was no significant lubricant pressure generation because of low strain and normal pressure. The strain increases as the drawing depth increases, and it forms a converging film. The lubricant pressure generation gets higher as the drawing depth increases, as seen in Figure 4.10 (b) and (c). The cup drawing velocity used in the FE simulation is 25 mm/s. At this speed, the average coefficient of friction (shown in Table 4.1) is close to the BL regime. The coefficient of friction is dependent on the contact area that evolves from the asperity flattening processes.

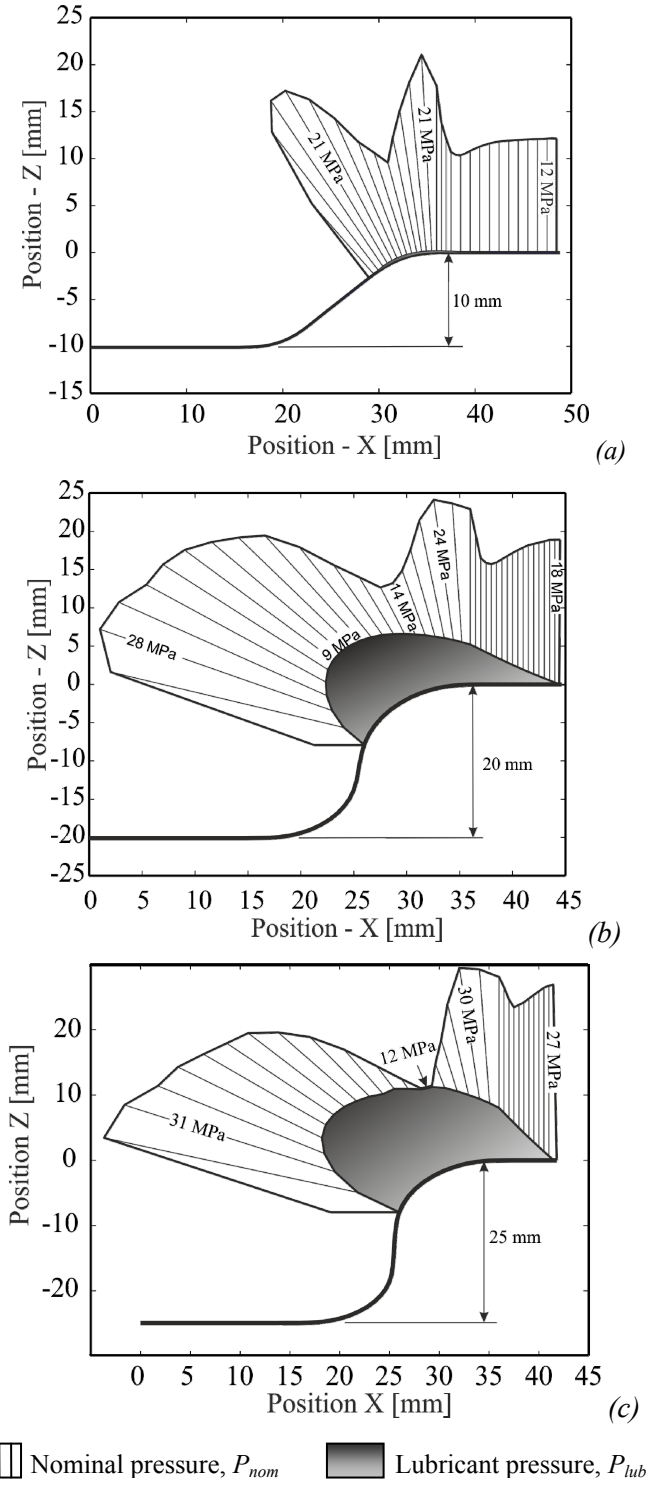

Figure 4.10: Pressure profile under the blank holder of the cup for three depths (a) 10 mm, (b) 20 mm and (c) 25 mm respectively.

When the drawing depth increases, the fractional contact area is increased due to asperity flattening as a result of an increase in stretching and normal loading. At a drawing depth of 25 mm, even though the fractional contact is high, the load carried by the lubricant is high as seen in Figure 4.10 (c), which led to a low coefficient of friction.
When the drawing speed is increased two-fold, the average coefficient of friction decreases further due to ML at a drawing depth of 25 mm. The coefficient of friction is even lower with the four-fold increase of the drawing velocity at a drawing depth of 25 mm. The coefficient of friction in the BL and ML regime is compared in Table 4.1. The average coefficient of friction values (see equation (4.25)) are higher for the ML model than for the BL model. As seen in the Table 4.1, the average fractional contact area for the whole contact zone is hindered by the generation of lubricant pressure due to sliding action. There is no significant ML process up to a cup depth of 10 mm. As the cup depth increases, ML becomes more pronounced due to the increase in contact pressure and straining, which results in a lower coefficient of friction. From these results, it can be seen that the coefficient of friction cannot be constant for the deep drawing processes. It is dependent on the operational, deformation and material conditions.

Cup depth (mm)	Drawing speed (mm/s)	Average Fractional contact area [%]		Average Coefficient of friction, μ_{ave} [-]	
		(BL)	(ML)	(BL)	(ML)
10	25	16	16	0.220	0.220
20	25	55	26	0.227	0.179
25	50	71	61	0.224	0.143
25	50	71	60	0.224	0.097
25	100	71	60	0.224	0.046

Table 4.1: Calculated average friction values and average fractional contact area at various drawing depths and speeds.

4.6 Lubricant starvation

In deep drawing processes, the amount of lubricant applied on the sheet material reduces the friction in the blank holder and punch regions. Lubrication reduces the failure of the deep drawn products like necking, wrinkling and fracture. However, the amount of lubricant is reduced to cut down the additional cost of cleaning up the oil after the forming process as required by stringent environmental laws. A typical norm for the lubrication amount after cold rolling process is within a range of 0.6 – 2.0 g/m^2 depending on the customer requirement. The lubricant film thickness is 0.67 - 2.2 μm for these lubrication amounts (lubricant viscosity of Quaker N6130 = 0.892kg/dm^3). Sometimes, other levels of lubrication are also applied for specific process requirements. In addition, lubricant is also applied on the tool surface during complex deep drawing processes. Hence, the input of the lubrication amount to the ML model is critical for friction prediction. To account for the presence of limited amounts of lubrication, the volume of the valleys in the workpiece surface is calculated after the asperity deformation process explained in Section 4.2 as,

$$V_{valleys} = \int_{-\infty}^{d_s - u_s} (d_s - u_s - z)\phi(z)dz \tag{4.27}$$

If the volume of applied lubricant is equal to or greater than the volume of the surface, hydrodynamic flow occurs. Otherwise, the coefficient of friction is calculated from the BL lubrication model.

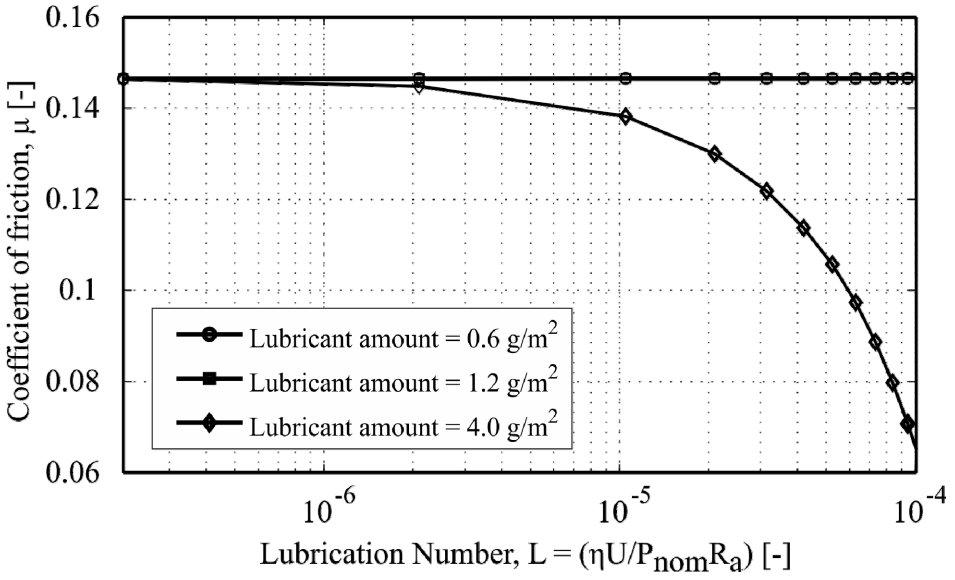

(a)

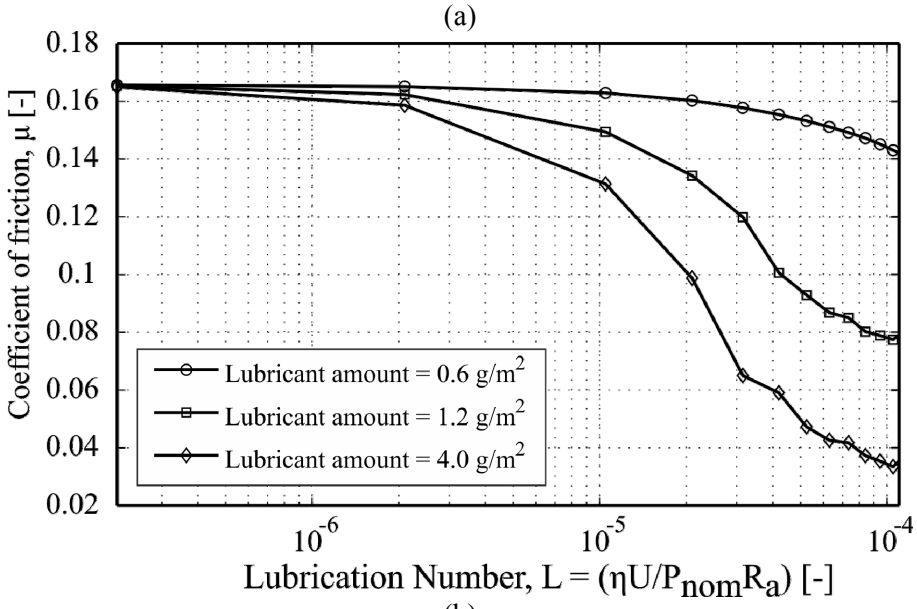

(b)

Figure 4.11: Starved lubrication for (a) low straining process and (b) high straining process.

In Figure 4.11 (a), the development of the coefficient of friction is shown for a low straining process (ε = 0~0.1) with different amounts of applied lubricant in a Stribeck plot. The BL regime is predominant for limited lubrication (0.6~1.2 g/m^2). For a high amount of lubrication (4.0 g/m^2), the lubrication regime transits to mixed lubrication. In the case of high straining processes (ε = 0~0.3), the lubrication regime transition to ML is more evident. Even for lower amounts of lubricant, the friction conditions slowly transit from BL to ML regime. When the lubrication amount is increased, then the coefficient of friction is further reduced due to ML.

4.7 Surface roughness effects on lubricant flow using flow factors

The standard Reynolds equation is suitable for describing the flow of the lubricant between smooth surfaces. Surface roughness affects the flow of the lubricant. Patir and Cheng [40] were one of the first to introduce roughness effects on fluid flow in hydrodynamic lubrication. They formulated flow factors in the Reynolds equation for the pressure and shear driven flow for nominally separated surfaces. However, this model is not suited for application in deep drawing processes where high fractional contact areas are involved. Wilson and Marsault [70] developed an alternate flow factor method using a wide variety of surfaces for large fractional contact area situations. The surface lay is defined by the auto-correlation function of the surface in both directions of the surface as explained in Appendix A. When the surface lay is orthogonal to the sliding direction (transversal anisotropic surface $\gamma_{lay}<1$), there is a increase in lubricant pressure generation due to the restriction of the hydrodynamic flow as shown in Figure 4.12 (a). When the surface lay is parallel to the sliding direction (longitudinal anisotropic surface $\gamma_{lay}>1$), there is a decrease in lubricant pressure generation since the surface facilitates the hydrodynamic flow as shown in Figure 4.12 (b). The coefficient of friction development is shown in Figure 4.12 (b). Due to increased lubricant pressure in transversal surfaces, the load carried by the contacting asperities is low. Hence the coefficient of friction is lowered due to hydrodynamic flow. In longitudinal surface lay, the contacting asperities carry more load than the lubricant. Consequently, the coefficient of friction is higher than the isotropic surface. The flow factor is widely criticised for its use with the standard Reynolds equation to describe the roughness effects. Only the roughness effects are illustrated with the flow factor method but the accuracy of the method is not discussed. Homogenization techniques are developed recently by [71]-[73] based on the local changes in the film thickness giving a better description of the roughness. Surface roughness effects are described by the oscillation coefficients for the hydrodynamic pressures in the Reynolds equation.

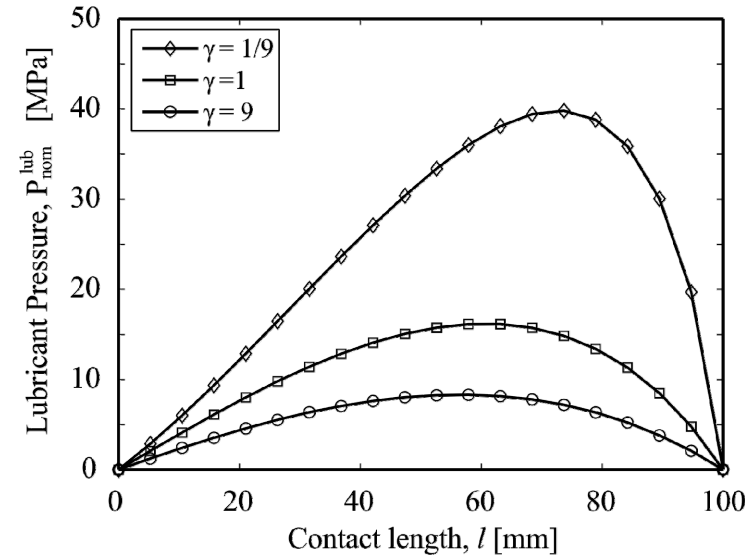

(a)

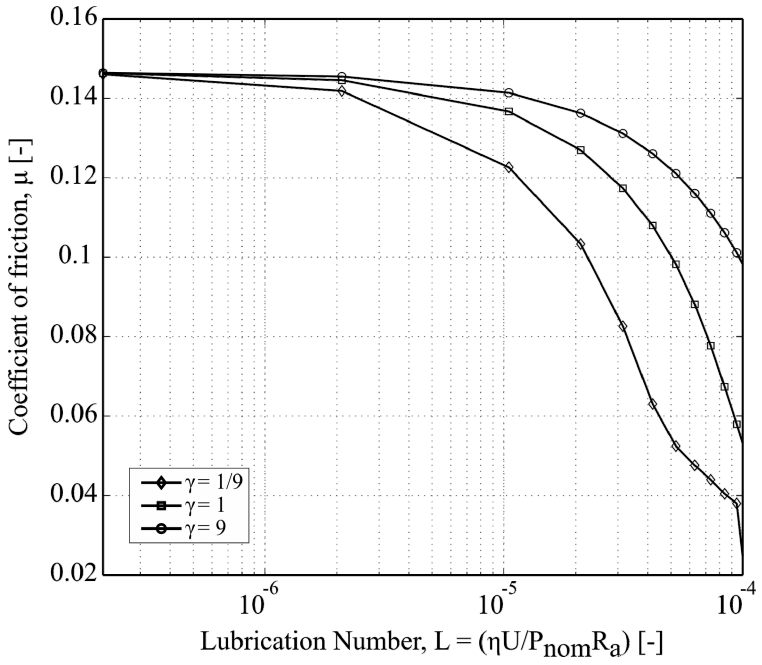

(b)

Figure 4.12: (a) Lubricant pressure generation and (b) Coefficient of friction development for different surface lays using flow factor method.

4.8 Summary

In this chapter, a mixed lubrication model has been developed and combined with the asperity deformation model of Westeneng [18]. The micro-mechanisms occurring at the workpiece and tool roughness scale such as flattening due to normal loading and stretching, ploughing, boundary and mixed lubrication are taken into account. The lubricant pressure distribution for various sliding velocities is shown. The coefficient of friction decreases due to hydrodynamic effects and also increases due to the influence of bulk strain. Further, the nominal pressure, sliding velocity and strain were taken from FE simulation of a cup and used in the mixed lubrication model to calculate the coefficient of friction. The coefficient of friction was shown for cup drawing at three different drawing depths. Results show that there is a transition from BL to ML towards the end of the drawing process. For high-speed drawing processes, it will even reach hydrodynamic lubrication. The current model better describes the friction conditions related to sliding contacts in the deep drawing processes under lubricated conditions. Further, a lubricant starvation model is included to see the influence of the amount of applied lubricant. The tribo-system in the SMF processes operates in the BL regime for low amount of lubrication and transists to the ML regime for high amount of applied lubricant. The surface roughness effects are also included in the model by introducing the flow factor method of Wilson and Marsault [70] for high fractional contact situations, such as in deep drawing processes. Longitudinal surface lay facilitates fluid flow and increases the coefficient of friction while transversal surface lay restricts the fluid flow and decreases the coefficient of friction.

Chapter 5
DETERMINISTIC CONTACT AND FRICTION MODEL – FULLY PLASTIC DEFORMATION MODE

5.1 Introduction

For two rough surfaces in contact, the actual surface to surface contact occurs only at asperity level. The local contacting asperities form micro-contacts. The real contact area of these micro-contacts is generally lower than the nominal contact area. Friction force arises within the micro-contact patches due to adhesion and ploughing. To predict the friction in the contact, it is essential to develop the contact model for describing the interaction in the micro-contacts. The main focus of this chapter is to develop an asperity interaction model and friction model for plastic conditions. In tribological problems, the traditional contact models of [13] and [15] are characterized by elastically or plastically deforming asperities using a summit based model on a single roughness scale. When the friction process is deformation dependent in a sliding contact, the asperity geometry which is interacting within the micro-contact influences the friction. In SMF processes, the contact occurs between a smooth tool and a rough workpiece (i.e. sheet material) surface under sliding contact conditions. The workpiece surface deforms under normal loading and makes small micro-contact patches. The interacting surfaces have different roughness levels. Hence the contact occurs at two different roughness levels as shown in Figure 5.1.

- At workpiece roughness level, the workpiece surface is deformed by normal loading of the tool.
- At tool roughness level, tool asperities indent and plough through the workpiece due to sliding of the sheet between the tools.

Ploughing occurs when there is a difference in the hardness of the materials under contact. The friction force is generated due to the energy losses by deforming the softer surface and shearing the boundary layer during sliding. In this chapter, a multi-scale contact model is developed for rough contact situations between tool and workpiece occurring in metal forming processes. In contrast to the existing contact models, the current model includes the roughnesses of both the sheet and the tool. The contact model uses a deterministic approach to characterize the interacting asperity geometry by an elliptical paraboloid [74]. The deterministic approach gives a better description of the asperity geometry when compared with the statistical approach. An asperity deformation model is used to describe the formation of contact patches of the workpiece surface. A ploughing model is used to calculate the amount of indentation of the tool asperities. The indented asperity geometry of the tool surface is used to calculate the coefficient of friction with a friction model. The

deterministic model is analysed with various workpiece and tool surfaces for different loading conditions and the friction influencing factors are discussed.

5.2 Contact of rough surfaces

The contact conditions which occur between the sheet metal and tool at the local contact spot determine the coefficient of friction. The interacting surfaces are composed of peaks and valleys. The surface height matrix (see Figure 5.2) indicates the height of a surface at a certain location in the sampled area. The roughness between the tool and workpiece is significantly different for the contact modelling pertaining to the friction prediction. Hence, the contact between the surfaces is modelled at two different roughness levels.
A deterministic contact model was developed by Ma et al. [74] for predicting friction conditions in an aluminum extrusion process. The contact model includes a single roughness scale (tool roughness). In an aluminum extrusion process, the deforming workpiece material is soft and it deforms onto the tool roughness at high contact pressures and high temperature working conditions. These conditions results in a very high fractional contact area. However, the fractional contact area is typically lower in sheet metal forming processes. The roughness of both the contacting surfaces is expected to be important. Therefore, it is important to include both the tool and workpiece roughness scales to predict the friction conditions in the contact for deep drawing processes.

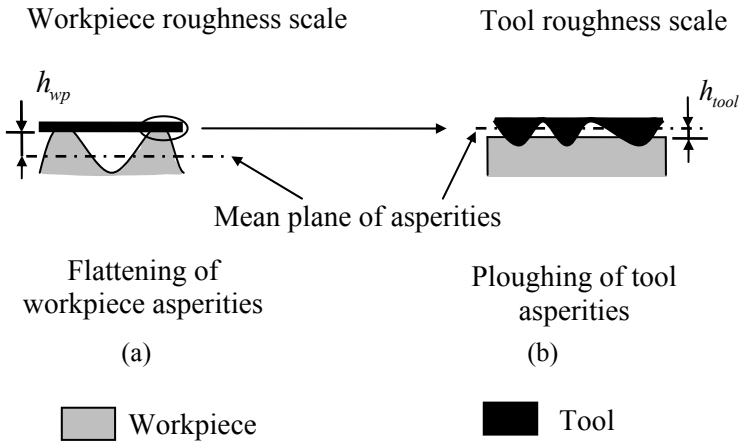

Figure 5.1: Contact between workpiece and tool at (a) Workpiece roughness scale (b) Tool roughness scale.

The multi-scale contact model is developed based on the work of [74] and [75] and is applied to SMF processes. The two scales are based on the roughness of the tool and workpiece surfaces. In the workpiece roughness scale, the workpiece is assumed to be rough and the tool to be smooth. The smooth tool flattens the encountered workpiece asperities as shown in Figure 5.1 (a).
At the largest length scale (workpiece roughness scale), a deterministic contact model (see Section 5.5) is used to calculate the flattening of workpiece surface due to normal loading.

At tool roughness scale, the tool is composed of micro contacts ploughing through the flattened plateaus on the workpiece asperity as shown in Figure 5.1 (b). The deterministic approach (see Section 5.3) is used to model the effect of size and shape of the ploughing tool asperities as described by Ma et al. [74]. The basic process in this deterministic contact and friction model for rough surfaces can be summarized as, (see Figure 5.2 and see Figure F.1 in Appendix F):

1. Input of representative workpiece and tool surfaces.
2. Deformation of the workpiece surface due to normal loading.
3. Contact patch identification of the workpiece surface.
4. Mapping of tool asperities onto the identified workpiece contact patches.
5. Calculation of tool indentation by force equilibrium.
6. Characterization of tool asperity shape.
7. Calculation of the coefficient of friction.

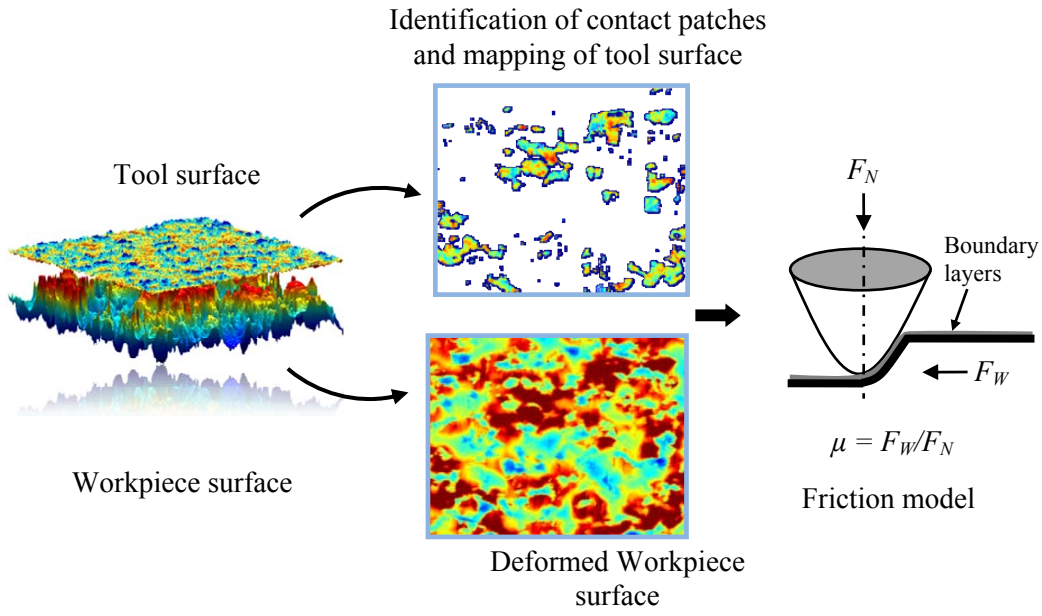

Figure 5.2: Multi-scale friction model framework.

5.3 Asperity characterization process

Traditionally in the contact model of Greenwood and Williamson [13], the asperities are modelled in a statistical approach. The model uses the statistical distribution of the given surface, (i.e. a probability density function of asperities) with a mean radius of the asperities. The important aspect of the statistical model is in finding the summits. Summits are important since in most cases - the contact is assumed to occur only on the summits. Typically, the summits are found by the height of a measurement point with the neighbouring summits. When the neighbouring asperities are lower than the point of

interest, it is termed as summit. A three-point rule (in the case of a line profile), five-point rule or nine-point rule (in the case of a surface profile) can be used to identify the summits as shown in Figure 5.3. The summit radius, R is found by calculating the local curvature using a finite difference approximation from the surface height data.

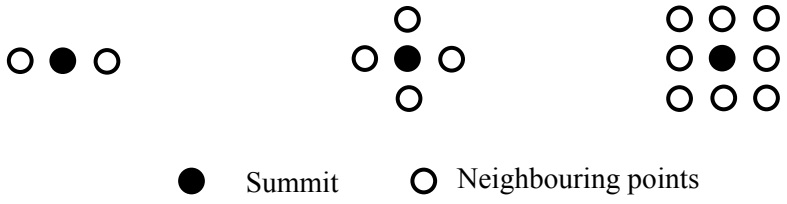

(a) Three-point summit rule (b) Five-point summit rule (c) Nine-point summit rule

Figure 5.3: Identification of summits in a given surface.

The summit-based models are suitable for contact conditions where low contact areas are formed. Figure 5.4 shows the fractional contact area of a Gaussian surface using the summit-based approach for the given surface separation. The surface separation is normalised by the standard deviation of the rough surface. The contact area for the summit based model is obtained by summing the contact area borne by the individual summits. For a given surface distribution $\phi(z)$, the fractional contact area for plastic deformation by means of summit based model is given as follows:

$$\alpha_{summit} = 2\pi R\rho \int_{h}^{\infty} (z-h)\phi(z)dz \tag{5.1}$$

The fractional contact area obtained by truncating the Gaussian surface is given as,

$$\alpha_{trunc} = \int_{h}^{\infty} \phi(z)dz \tag{5.2}$$

Pullen and Williamson [15] did experiments in a closed die where the material is confined. They found that the bulk material flow is not allowed for the plastically deforming summits when constrained. The fractional contact area (α_{PW}) according to [15] for the given nominal contact pressure and hardness of the material is given as,

$$\alpha_{PW} = \frac{P_{nom}}{P_{nom}+H} \tag{5.3}$$

It can be seen from Figure 5.4 (a) that the summit-based and truncation models show different characteristics. At high separation level, the summit-based model predicts a lower contact than actual truncated area of the surface. This is because the load is only shared by the summits, not by other parts of the surface. As the separation is further decreased (i.e. increasing load), the real contact area exceeds the nominal contact area. In the truncation-based method, the contact area grows by interfering with the neighbouring area. However, the summits grow independently. The coalescence of contact patches at negative separation

levels is not explained in Greenwood and Williamson's model [13]. In Figure 5.4 (b), the fractional contact area for the truncation-based model and Pullen-Williamson model is shown. If the asperities do not rise to conserve the volume during deformation, the contact area increases linearly. However, the asperities tend to rise when the volume is constrained. Pullen and Williamson's method shows a nonlinear increase of contact area with the increase in nominal contact pressure as seen in Figure 5.4 (b).

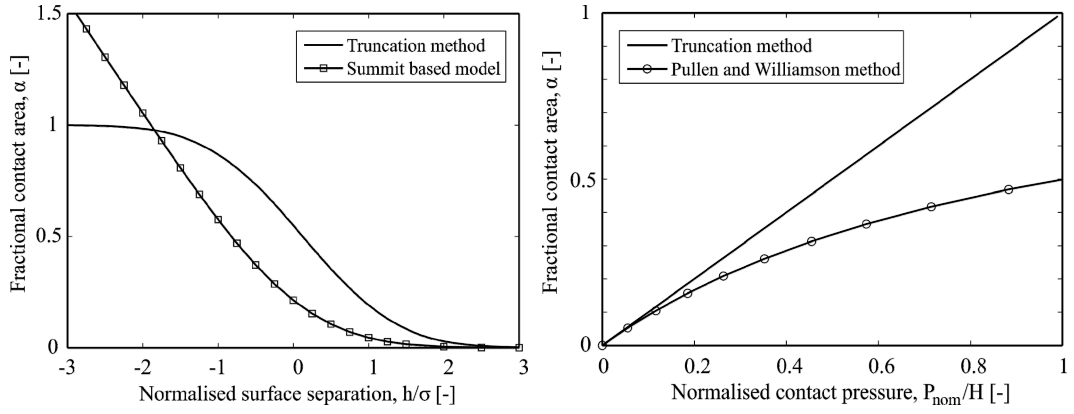

(a) (b)

Figure 5.4: Fractional contact area for a Gaussian surface using (a) summit based model and truncation method.and (b) with/without volume conservation.

Nayak's model [76] deals with coalescence of the contact area during deformation. Nayak considered the surfaces with contact patches and holes which interfere with one another as the load is increased. It can be clearly seen that the summit based models predicts untrue contact areas especially under high contact pressure conditions, as the summits grow independently of the neighbouring area. The statistical model of Nayak showed that the interference of contact patches should be considered. Nayak's method considers only the formation of contact patches, but do not give any idea about the shape of the asperities which is critical in modelling the friction. Hence, the deterministic approach of Ma [74] is used to describe the asperity geometry by means of using elliptical paraboloid shapes. The deterministic approach includes the coalescence of the contact patches. The asperities are characterized by finding the surface separation for a given contact pressure. The number of contact patches and the geometry of the contact patches are dependent on the contact pressure. Thus the coefficient of friction is dependent on the surface topography of the surface. For simplicity, only fully plastic deformation is considered in this chapter.

5.4 Deterministic approach

The surface is represented in a height matrix of pixels. As the contact load is increased, the surface separation reduces. For a known surface separation, the contact patches are located within the height matrix. The contact patches are identified by means of connected pixels. The properties of the contact patches for asperity characterization are better than the summits with constant parameters. The contacting pixels are digitized in the binary format.

Each contact patch is identified by means of connected pixels for a given surface separation. With image processing techniques, the connected pixels are identified by using a four-point connectivity criterion as shown in Figure 5.5.

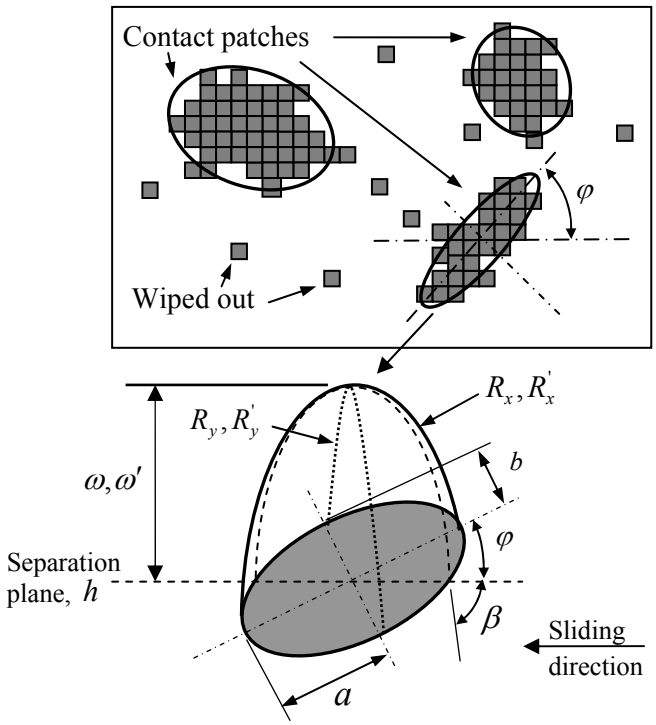

Figure 5.5: Identification and characterization of asperity shapes from Ma et al. [74].

After the contact patches have been identified, they are characterized as elliptical paraboloids using the volume and area of the contact patch. This gives a better description of the asperity compared to the conical or spherical shape according to Masen [75]. Using a volume conservation approach, it gives a greater control of the asperity description. The base area of the contact patch is described using ellipse with a major and minor radii, a and b, and the orientation of the ellipse with respect to sliding direction, φ. The properties of the contact patch are obtained by keeping the second central moments of the contact patch and ellipse equal. The curvatures of the elliptical paraboloid in major and minor direction is given as,

$$\kappa_x = 4\pi \frac{V}{A^2} \frac{b}{a} \tag{5.4}$$

$$\kappa_y = \kappa_x \left(\frac{b}{a} \right)^2 \tag{5.5}$$

The total volume of the contact patch is the volume of the measurement heights above the given separation plane summed over the micro-contacts.

$$V = p_x p_y \sum_{i=1}^{m} (z - h) \tag{5.6}$$

where $p_{x,y}$ is the pixel size of the measurement heights in x and y direction and m is the number of measurement heights in contact.
The area of the contact patch is given as,

$$A = \pi a b \tag{5.7}$$

The height of the asperity is determined from the volume and area of the contact patch so that the load and energy balance can be maintained according to [75]. Now the asperity can be fully characterized with an elliptical paraboloid shape as shown in Figure 5.5.

$$\omega = \frac{2V}{A} \tag{5.8}$$

5.5 Deterministic flattening model

A representative workpiece surface is taken from the DC06 steel sheet using a confocal microscope. After the input of the surfaces as shown in Figure 5.2, the deterministic flattening model is used to calculate the deformation of the workpiece surface by a flat tool for pure plastic conditions. During flattening, it is assumed that all the non-contacting asperities rise equally. The amount of rise of all non-contacting asperities is equal to the total flattened volume of the deformed asperities to maintain volume conservation. After deformation of the workpiece surface, the contact patches are identified at a given separation distance using the binary image processing techniques. Each contact patch is identified by a cluster of pixels connected to its edge. There are some isolated pixels which may be due to errors in the surface roughness measurement. Those pixels which do not form a contact patch are wiped out. The identified contact patches are characterized with elliptical paraboloids as described by Ma et al. [74] shown in Figure 5.5. During asperity shape characterization, the volume and the area of the contact patch are preserved. The force carried by an elliptical paraboloid is calculated as given by Masen et al. [75]. For deep drawing materials, the workpiece is softer than the tool. Hence, it is fair to assume that the workpiece asperity will be in full contact with the tool during sliding. For pure plastic conditions, the pressure carried by an asperity is equal to the hardness. The contact area, A_{wp} and force, $F_{N,wp}$ for an elliptical paraboloid asperity under pure plastic conditions is given as [9],

$$A_{wp} = 2\pi \sqrt{R_x R_y}\, \omega \tag{5.9}$$

$$F_{N,wp} = HA_{wp} \tag{5.10}$$

where, R_x - Radius of the paraboloid (workpiece asperity) in the major direction of the ellipse, ($R_x = 1/\kappa_x$)

R_y - Radius of the paraboloid (workpiece asperity) in the minor direction of the ellipse, ($R_y = 1/\kappa_y$)

ω - Height of the paraboloid (workpiece asperity) above the separation distance, h_{wp}

H - Hardness of the workpiece material

With an iterative procedure, the separation plane, h_{wp}, (as shown in Figure F.1 in Appendix F) is found. The nominal pressure, P_{nom}, carried by the given surface is the sum of the contribution from the individual asperities as follows:

$$P_{nom} = \frac{\sum_{i=1}^{n} F_N}{A_{nom}} \tag{5.11}$$

where, P_{nom} - Total applied pressure

A_{nom} - Nominal contact area

n - Total number of workpiece asperities in contact

The fractional contact area calculated from the asperity flattening model is shown in Figure 5.6 (a) in comparison with the summit-based models, i.e. without coalescence and no volume conservation. The fractional contact area is linear in the case of no volume conservation where the bulk material flow is allowed. The fractional contact area varies by a large amount for high pressure contact situations when volume conservation is considered. In Figure 5.6 (b), the surface separation for a given is shown. It can be seen that the surface deformation is less when volume conservation is allowed. This shows that additional energy is required to deform the surface when volume conservation is followed. The additional energy increases with the increase of contact pressure.

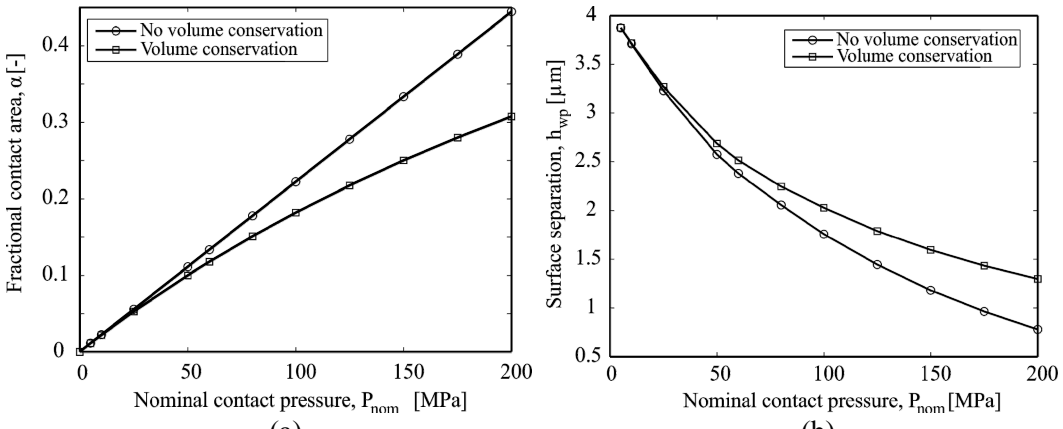

Figure 5.6: (a) Fractional contact area and (b) Surface separation for a surface with/without volume conservation.

5.6 Deterministic ploughing model

In this section, the indentation of the tool asperity into the flattened workpiece is explained. The deformed workpiece contact patches are mapped on the tool surface as shown in Figure 5.2. The surface heights of the contact patches are extracted from the given tool surface distribution. With the known tool surface height data of a contact patch, a paraboloid is constructed with an elliptical base of equal volume to the contact patches above the given tool indentation level ω', (see Figure 5.5). Thus each asperity of the tool coming into contact with the workpiece is uniquely characterized to calculate the friction forces. The tool separation plane, h_{tool} (as shown in Figure 5.1) is found by means of an iterative procedure. The total applied load should be carried by all the tool asperities (m is the total number of contacting tool asperities) which are in contact with the workpiece. For sliding contact conditions, it is assumed that only front half of the asperity is in contact under pure plastic deformation. The contact area, A_t, and load, $F_{N,t}$, carried by an elliptical paraboloid asperity under plastic conditions according to [75] is given as,

$$A_t = \pi \sqrt{R_x^{'} R_y^{'}}\, \omega^{'} \tag{5.12}$$

$$F_{N,t} = H_{ind} A_t \tag{5.13}$$

where, $R_x^{'}$ - Radius of the paraboloid (tool asperity) in the major direction of the ellipse

$R_y^{'}$ - Radius of the paraboloid (tool asperity) in the minor direction of the ellipse

$\omega^{'}$ - Height of the paraboloid (tool asperity) above the separation distance, h_{tool}

H_{ind} - Indentation hardness of the workpiece material

During indentation, the hardness depends not only on the bulk material properties but also on the contact geometry. Indentation tests [77] - [80] show that the hardness increases as the indentation size decreases, especially at the macro and nano indentations. This is known as indentation size effect. The indentation hardness depends on the shape of the geometry. The contact geometry of the asperity is characterized by its contact angle, β, as shown in Figure 5.5. The contact angle is dependent on the contact radius of the asperity and indentation depth. Gao [79] derived an indentation model for spherical and conical shapes based on Johnson's expanding cavity model [80]. For pure plastic conditions with no strain gradient effects, the indentation hardness for an asperity as given in equation (5.14). The calculated indentation hardness of the asperity for the contact angle is shown in Figure 5.7. The indentation hardness is high for the asperity with high attack angles. Consequently, the contact pressure carried by the asperity is also high.

$$H_{ind} = \frac{2}{3}\sigma_y \left[\frac{7}{4} + \ln\left(\frac{1}{3} \frac{E^*}{\sigma_y} \cot\beta \right) \right] \tag{5.14}$$

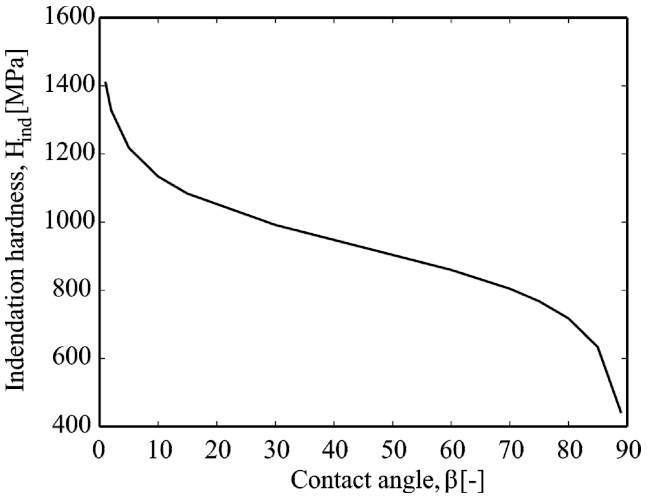

Figure 5.7: Indentation hardness depending on asperity geometry.

The effective attack angle, β, of an asperity is separately calculated for each asperity depending on the orientation of the elliptical base shape, φ, with respect to the sliding direction, as shown in Figure 5.5. Hokkirigawa and Kato [47] extended the application of the 2D slipline model of Challen and Oxley [10] to a 3D scenario by introducing a shape factor, ζ, which was determined experimentally. The effective attack angle of an asperity, β, was given by Ma et al. [74] as follows:

$$\beta = 2\arctan\left(\frac{\omega'}{\zeta a_{contact}}\right) \tag{5.15}$$

The effective contact area radius, $a_{contact,}$ of an ellipse with respect to the orientation of the elliptical paraboloid asperity in the sliding direction is given as,

$$a_{contact} = \frac{ab}{\sqrt{a^2 \sin^2 \varphi + b^2 \cos^2 \varphi}} \tag{5.16}$$

where, a - Major radius of tool asperity's elliptical base
b - Minor radius of tool asperity's elliptical base
φ - Orientation of the tool asperity with respect to sliding direction
ς - Shape factor for the tool asperity $(\varsigma = 0.8)$

Once the contact patches of the tool surface are formulated, the coefficient of friction, μ, is calculated from the geometry of the tool asperities. The contribution of the ploughing forces to the total friction force is dependent on the attack angle here represented by β.
An average effective attack angle, β_{avg}, is calculated by means of weighting the effective attack angle of an individual asperity with its contact area of the micro-contacts as follows, (see Ma et al. [74]):

$$\beta_{avg} = \frac{\sum_{i=1}^{m} \beta^i A_t^i}{\alpha A_{nom}} \tag{5.17}$$

where, β - Effective attack angle of the tool asperity with respect to sliding direction
α - Fractional contact area
m - Total number of tool asperities in contact

The coefficient of friction can be calculated from the arithmetic average attack angle of the asperities in contact with counter surface. Taking arithmetic average includes all the asperities irrespective of its size. However, a bigger contact patch contributes more to the friction force than the smaller patch. Hence the average weighted attack angle, β_{avg}, is determined from the area of the contact patch with respect to the real contact area, which is more meaningful than the simple arithmetic average value of the attack angles.

5.7 Surface roughness parameters

The properties of a given surface influence the attack angle of the asperities, which is critical to calculate the coefficient of friction. Influencing factors of a given surface for the friction prediction are studied in this section. Major influencing factors are surface roughness, surface lay and bandwidth parameter. Various tool surfaces have been digitally generated by using FFT techniques of Hu and Tonder [65] with different values for the roughness parameters. The bandwidth parameter (see equation (5.19)) for the digitally generated tool surfaces is matched to the real tool surface. The surface properties are listed in the Table 5.1. The pictures of the surface topography are given in Figure C.3 of Appendix C. The surface lay is defined by the ratio of autocorrelation length (ACL) of the surface in the *x* and *y* directions.

$$\gamma_{lay} = \frac{ACL_x}{ACL_y} \tag{5.18}$$

The bandwidth parameter is defined by the moments of power spectral density of the surface (m_0, m_2 *and* m_4) as,

$$\psi = \frac{m_0 m_4}{m_2^2} = \left(\frac{\sigma_z \sigma_\kappa}{\sigma_s^2} \right)^2 \tag{5.19}$$

where, σ_z - Standard deviation of the surface heights
σ_κ - Standard deviation of the surface curvatures
σ_s - Standard deviation of the surface slopes

Tool surface	Surface roughness, S_q [µm]	Surface lay γ_{lay} [-]	Bandwidth parameter ψ [-]
1	0.21	1.0	34
2	0.42	1.0	34
3	0.10	1.0	34
4	0.21	0.3	34
5	0.21	3.0	34
6	0.21	1.0	16
7	0.21	1.0	44

Table 5.1: Surface properties of tool used for the calculation.

The average weighted attack angle is calculated for surfaces by varying roughness levels. The attack angle shown in Figure 5.8 is calculated for the tool contact with various rough workpiece surfaces. For these calculations, workpiece surfaces are measured from six random spots measuring 1x1 mm with a spatial resolution of 1µm using a confocal microscope from the DC06 sheet metal at different spots. The properties of the measured workpiece surfaces are listed in Table 5.2. The pictures of the surface topography are given in Figure C.1 of Appendix C. The calculated attack angle of the different tool surfaces against the contact pressures is shown in Figure 5.8 (a). It can be seen that the attack angle is influenced by the surface topography of the tool surface and contact pressure. The formation of the tool asperity is influenced by the formation of the workpiece surface contact patches. The error bar in the figure shows the variation of the different workpiece surfaces. If a surface is rough, it has high peaks and deep valleys. The slope of the asperities is quite high for a rough surface. The rougher surface contains sharp contact patches (i.e. asperity with high attack angle) than a smooth surface when the surface is brought into contact. Figure 5.8 (a) shows the average attack angle for the tool surfaces 1, 2 and 3 as given in Table 5.1. The attack angle of the roughest surface (Surface S2) is the highest. The attack angle decreases with the contact pressure. This is due to the clustering of asperities at high contact pressure which produces blunt contact patches (i.e. asperity with small attack angle). If the surface is isotropic ($\gamma_{lay} = 1$), the sliding direction doesn't influence the formation of contact geometry. For anisotropic surfaces, the surface lay influences the attack angle. If the asperities are transversely oriented ($\gamma_{lay} < 1$), the attack angle is large. If the asperities are longitudinally oriented ($\gamma_{lay} > 1$), the attack angles are lower than the transverse orientation as shown in Figure 5.8 (b). Surface is composed of different asperities with different heights, slopes and curvatures. The bandwidth parameter is used to explain how the frequency spectrum of the surface heights is spread on the roughness profile. For a high bandwidth surface, the asperity curvature is higher than a low bandwidth surface even though the surface roughness is same. The high bandwidth surface has asperities with small radius which results in formation of sharp contact patches as shown in Figure 5.8 (c).

Workpiece surface	Surface roughness S_q [µm]	Skewness S_κ [-]	Kurtosis K [-]	Surface lay γ_{lay} [-]
1	1.78	0.34	2.35	1.1
2	1.75	0.29	2.40	1.1
3	1.58	0.03	2.49	1.0
4	1.72	0.22	2.33	1.0
5	1.69	0.09	2.63	1.1
6	1.59	0.33	2.62	1.0

Table 5.2: Surface properties of sheet material used for the calculation.

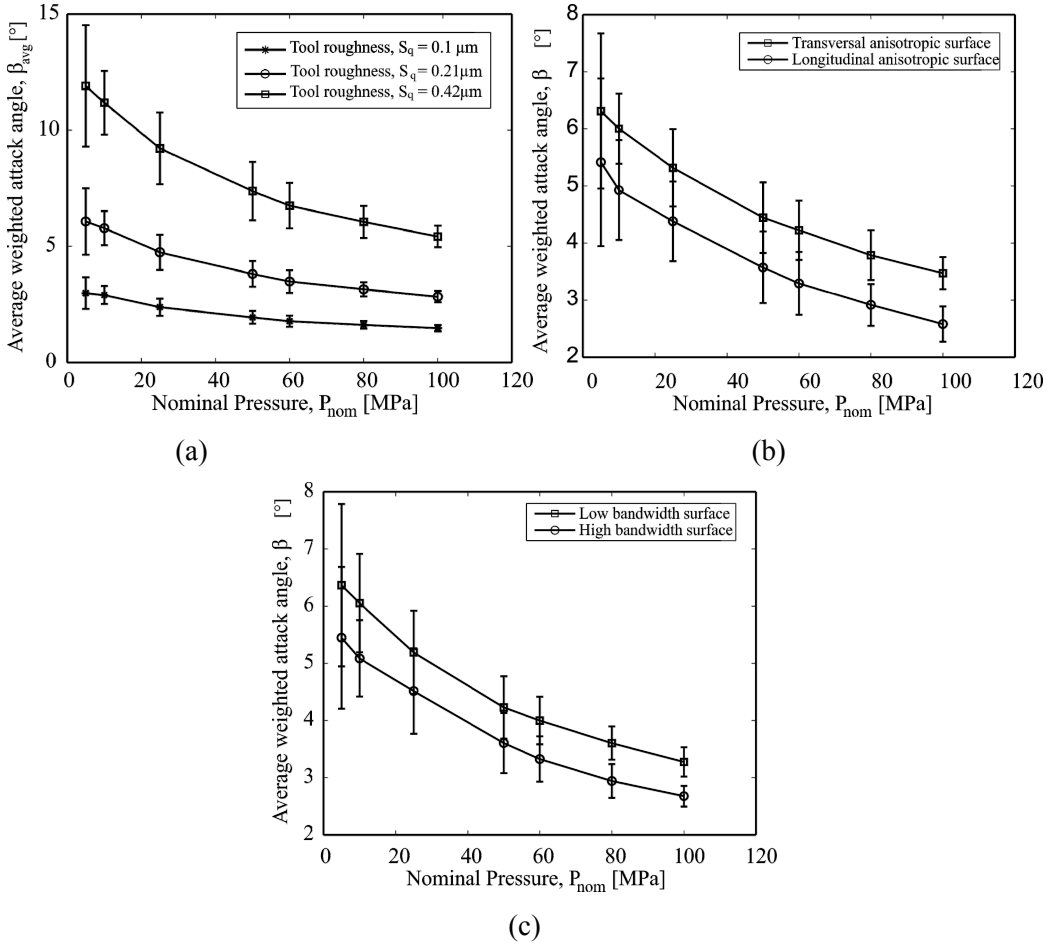

Figure 5.8: Average contact angle of the tool asperity with a workpiece for a given nominal contact pressure.

5.8 Friction model

The coefficient of friction, μ is calculated from Challen and Oxley's model [10] with the input parameters from Table F.1 (see Appendix F). The coefficient of friction is calculated with an interfacial friction factor, f_{hk}, for boundary layers formed by the lubricant and average contact angle of the tool asperities, β_{avg}. In the rubbing mode, when there is no wear (for $\beta_{avg} < 45°$), the coefficient of friction is given as

$$\mu = \frac{B\sin\beta_{avg} + \cos\left(\cos^{-1} f_{hk} - \beta_{avg}\right)}{B\cos\beta_{avg} + \sin\left(\cos^{-1} f_{hk} - \beta_{avg}\right)} \tag{5.20}$$

where,

$$B = 1 + \frac{\pi}{2} + \cos^{-1} f_{hk} - 2\beta_{avg} - 2\sin^{-1}\frac{\sin\beta_{avg}}{\sqrt{\left(1 - f_{hk}\right)}} \tag{5.21}$$

In the cutting mode (for $\beta_{avg} > 45°$), the coefficient of friction is given as

$$\mu = \tan\left(\beta_{avg} - \frac{\pi}{4} + \frac{\cos^{-1} f_{hk}}{2}\right) \tag{5.22}$$

5.9 Friction calculations with asperity deformation and ploughing model

For the parametric study, various tool surfaces for workpiece and tool as shown in Table 5.1 and Table 5.2 have been used. The calculated coefficient of friction is shown in Figure 5.9, Figure 5.11, Figure 5.12 and Figure 5.13 for various applied nominal pressures. The results are shown for six different workpiece spots with the standard deviation. The friction values are shown for various tool roughness (S_q), surface lay (γ_{lay}) and bandwidth parameter (Ψ) (see also Appendix C).

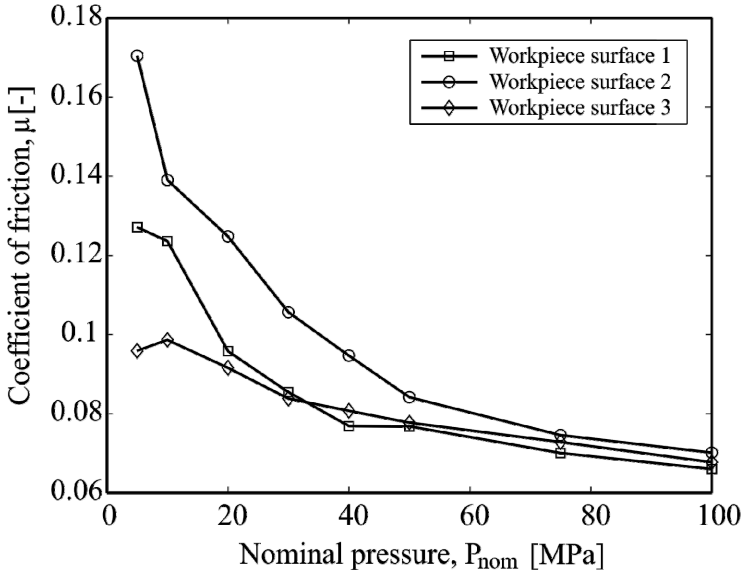

Figure 5.9: Calculated coefficient of friction with tool surface 1 for the workpiece surfaces 1, 2 and 3 (○, □ and ◊).

The variation of the coefficient of friction is shown in Figure 5.9 for three different workpiece surfaces (1, 2 and 3) with tool surface 1 which are found to be extremities in the calculated friction values. The friction decreases with a higher nominal contact pressure for all three workpiece surfaces. As thecontact pressure increases, the tool surface undergoes higher indentation. At high indentation levels, the tool asperities cluster together to form large and small numbers of blunt contact patches as shown in Figure 5.10 (b). This results in a lower coefficient of friction. While at low pressures, the tool asperities forms sharp contact patches resulting in high friction as seen in Figure 5.9 and Figure 5.10 (a).
It can also be seen that if the same tool surface is in contact with different workpiece surfaces, the coefficient of friction shows different values. The difference can be explained by the formation of tool-workpiece contact patches and indented asperity geometry. At low contact pressures, the variation of the coefficient of friction is high as seen in Figure 5.9. This variation in the friction decreases with the increase of the contact pressure. The degree of penetration of the tool asperities, ($D_p=\omega'/a_{contact}$), varies more at lower contact pressures than at higher contact pressures, as shown in Figure 5.10 (a). If the degree of penetration is high, sharp contact patches are formed. For workpiece surface 1 (symbol ○), the degree of penetration is the highest and it forms sharp contact patches resulting in higher friction. For workpiece surface 3 (symbol ◊), the degree of penetration is the least. Consequently, blunt contact patches are formed which results in lower friction. This shows that the two scale model is important to the friction prediction. The interaction between two rough surfaces is dominant when the contact pressure is low. For higher contact pressures, the roughness scales of the workpiece do not influence the friction conditions.

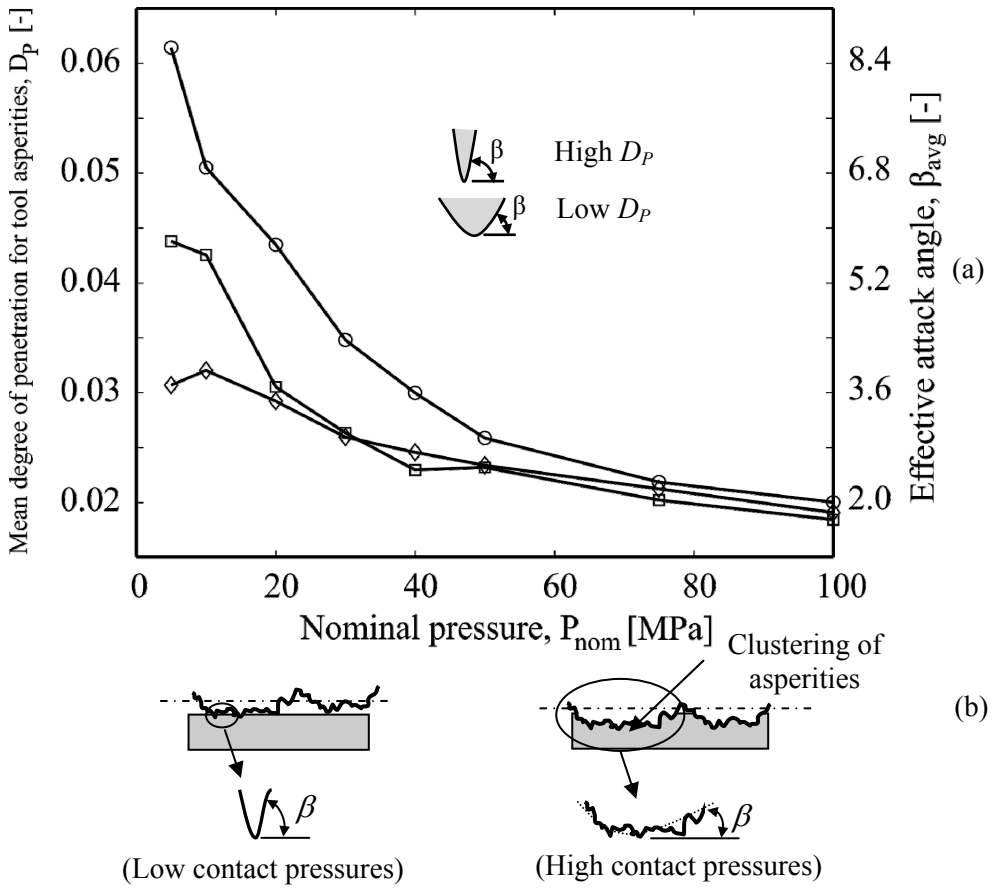

Figure 5.10: (a) Degree of penetration of tool asperities and effective attack angle for the given nominal pressure and (b) Formation of attack angles.

The calculated coefficient of friction is compared for three different tool roughnesses as shown in Figure 5.11. For rough tool surfaces, the asperities plough through the workpiece with a high attack angle. Hence the coefficient of friction is high. However for smooth tool surfaces, the asperities are blunt, which results in a low coefficient of friction.
In Figure 5.12, the coefficient of friction is shown for transverse and longitudinal lay. A transverse lay results in sharper contacts with respect to the sliding direction and results in a high friction force. A longitudinal lay results in blunt contacts and results in a low friction force.

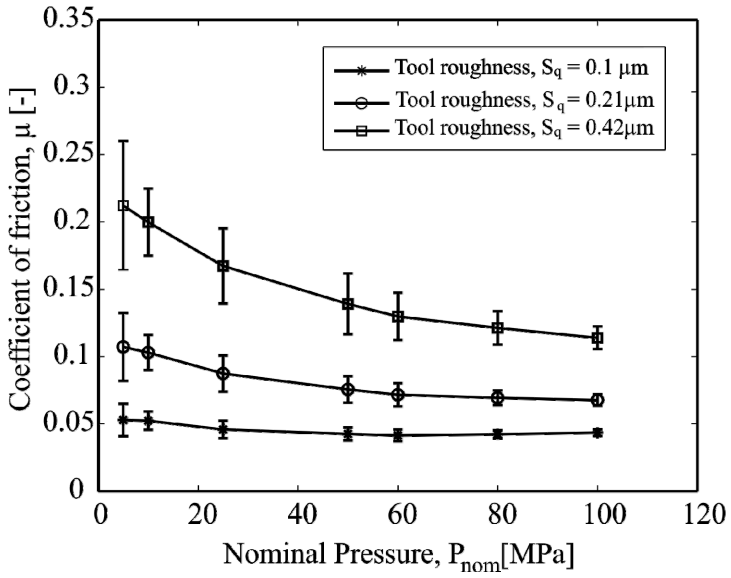

Figure 5.11: Calculated coefficient of friction at various nominal contact pressures with different workpieces (see Table 5.1) and tool surfaces (see Table 5.2).

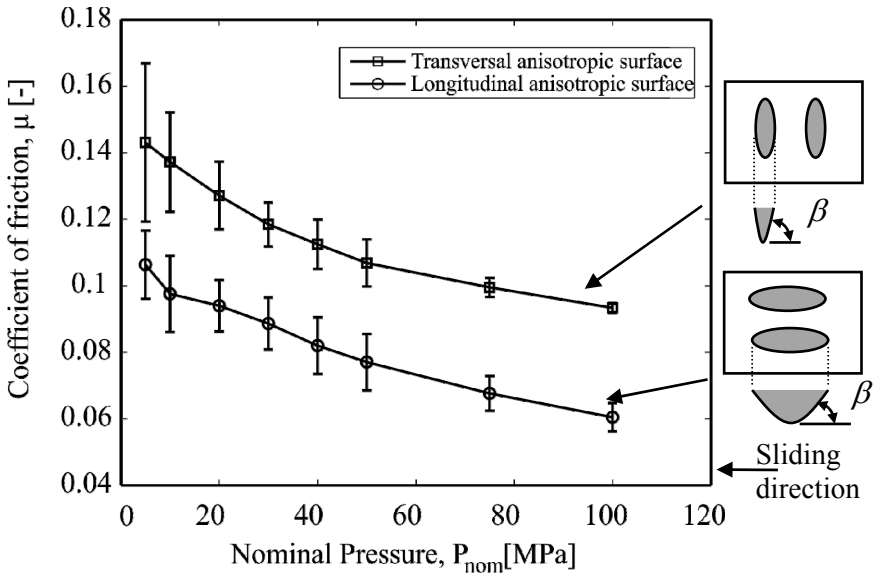

Figure 5.12: Calculated coefficient of friction as a function of nominal contact pressures for tool surfaces with longitudinal and transverse anisotropic lay.

In Figure 5.13, the results from the surfaces of low and high bandwidth parameters, Ψ, are shown. Low bandwidth surfaces (spiky surfaces) result in a higher coefficient of friction than high bandwidth surfaces (smooth surfaces).

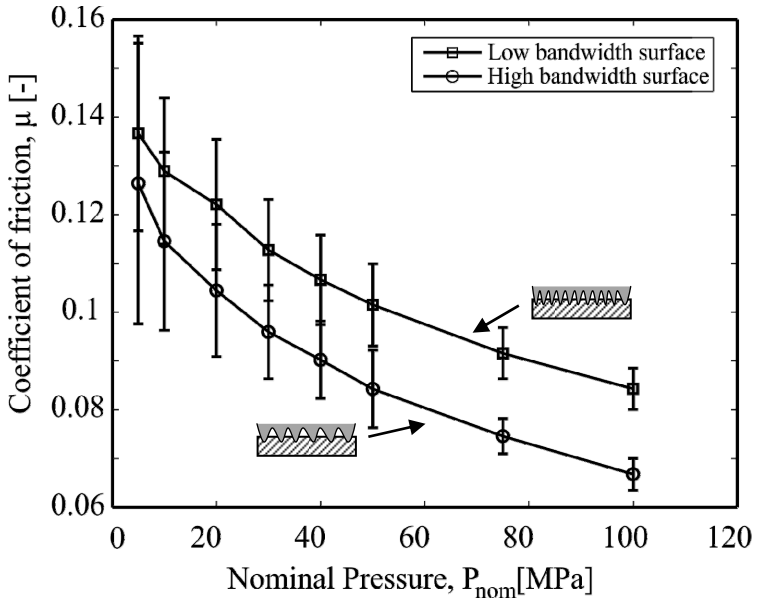

Figure 5.13: Calculated coefficient of friction as a function of nominal contact pressures with high and low bandwidth tool surfaces.

5.10 Influence of interfacial friction factor

Interfacial friction factor is influenced by the formation of the boundary layers at the surfaces. The boundary layers can be formed by either physical or chemical adsorption. The interfacial friction factor is given as

$$f_{hk} = \frac{\tau_{BL}}{k} \tag{5.23}$$

where τ_{BL} is the shear strength of the boundary layers during sliding and k is the shear strength of the bulk deforming material.
If the boundary layers can adhere to surface well, the shear strength is low. If the boundary layers fail, the shear strength increases and finally reaches the shear strength of the deforming surface if the lubricant fails completely. The shear strength of the boundary layers and its durability is typically determined from friction force measurements. The friction factor has major influence on the final coefficient of friction. In Figure 5.14, it can be seen that the coefficient of friction increases with the increase of the interfacial friction factor.

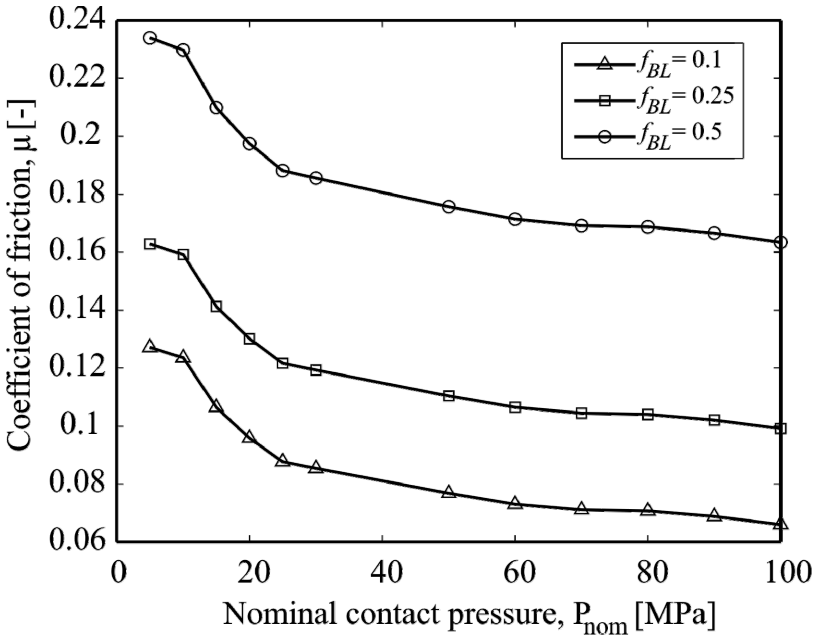

Figure 5.14: Influence of interfacial friction factor in the contact model.

5.11 Summary

A multi-scale contact model has been developed for the contact situations occurring in SMF processes for describing the friction based on the local contact conditions in the boundary lubrication regime. The model combines the surface deformation of the sheet material due to normal loading under pure plastic loading conditions with a detailed geometrical description of the tool asperities ploughing through the sheet surface. Results are shown for various combinations of tool and sheet material surfaces. It has been shown that the calculated coefficient of friction is strongly dependent on the micro-geometry of the tool and the sheet material, in particular at low values of the nominal contact pressure. At high nominal pressure, the coefficient of friction approaches to same value irrespective of the sheet material surface. Further it has been found that a tool surface of high roughness results in a higher coefficient of friction. A transverse surface lay results in a higher coefficient of friction than longitudinal surface lay. Also a low bandwidth tool surface (spiky surface) results in a higher coefficient of friction as compared to a high bandwidth surface. The coefficient of friction is also affected by the shear strength of the boundary.

Chapter 6
LOADING / RELOADING OF CONTACTING SURFACES

6.1 Introduction

In deep drawing processes, the sheet material surface undergoes repeated contacts with the tool surface. The contact pressure in the blank holder region varies according to the product/tool geometry. The contact pressure profile in the blank holder region of a cup drawing process from FEM simulation is shown in Figure 4.10. When the sheet material slides between the blank holder and die, the surface is subjected to a repeated loading process. The asperities will undergo different loading/reloading conditions, thereby influencing the deformation behaviour of the asperities. The coefficient of friction is affected by the local deformation behaviour. In this chapter, a friction model is developed based on the local deformation conditions with a contact model describing the elastic, elastic-plastic and plastic conditions during loading/reloading of the surfaces.

An asperity which is under contact undergoes three different modes of deformation with increasing load, i.e. elastic, elastic-plastic and plastic deformation. When an asperity undergoes elastic deformation, the deformation process is completely reversible. The asperity is restored to the original shape after the contact load is removed. When the load is increased to a critical point which is beyond the elastic regime, the onset of plasticity occurs. The plasticity occurs beneath the surface. While unloading the asperity, a part of the deformation zone remains plastic and the rest of the deformation recovers. The asperity geometry changes with the development of the plasticity. A finite element simulation is shown by Shankar et al. [81] (see Figure 6.1) for the deformation of hemispherical asperity with a rigid flat. Initially, a plastic deformation zone starts in a small contained region just beneath the centre of the asperity. The condition at the very apex of the asperity is a hydrostatic stress state since the pressure is infinite. The plastic deformation zone is surrounded by a hydrostatic core and the elastically deforming region as shown by Johnson [80]. With the further increase of load, the plastic region between the hydrostatic core and the elastic region grows. When a full plastic deformation stage is reached, the core and the elastic region are enveloped by the plastic region. A lot of attention has been paid to the contact model for the mixed modes of deformation at the single asperity level [13], [16], [83]-[87]. However, these models are not widely applied to calculate the coefficient of friction.

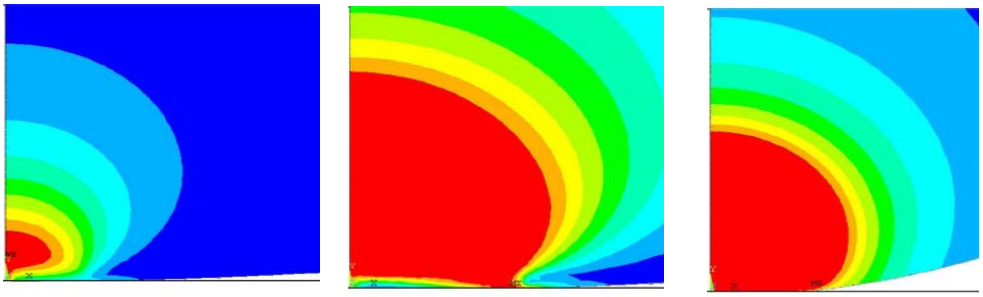

(a) (b) (c)

Figure 6.1: Development of plasticity in a hemispherical asperity with a rigid flat. (a) Inception of plasticity at the subsurface, (b) Plasticity reaching the surface and (c) Engulfing of the core and the surrounding elastic region.

Westeneng [18] described a friction model for full plastic deformation of the surface using a statistical approach for the deep drawing processes. In the deep drawing processes, the contact pressures are in a wide range. However, the full plastic deformation stage is reached when the contact pressures are high. In the die/punch rounding regions, the contact pressures are high (in the order of 100 MPa) but under the blank holder it is relatively low (10-50 MPa). At low pressures, the asperity can undergo mixed modes of deformation, i.e. elastic-plastic. Pure elastic deformation is negligible during the first contact between the blank holder and sheet material but can be important while reloading. Westeneng's model does not take elastic-plastic and reloading effects of the surface into account for the friction calculation. In the following Section 6.2, an elastic-plastic model for a single asperity contact is shown. The contact model is extended to multi-asperity contact situations as described in Section 6.3. With an asperity indentation model (as described in Section 6.6) and a boundary layer friction model (as described in Section 6.8), the coefficient of friction is calculated.

6.2 Elastic-plastic single asperity contact model

To begin with the contact model, the asperities are characterized by an elliptical paraboloid shape. The asperity shape is described by a major and minor axis radius with an elliptical base as described in Section 5.2. The major and minor axis radius of the paraboloid is denoted by R_x and R_y. The base contacting area of the ellipse is denoted by the semi-major and semi-minor contact radii, a and b.

6.2.1 Elastic contact

From Hertz's theory of elasticity, the elastic contact area and load are expressed in terms of interference of the asperity and its geometry. If the interference of the asperity, ω, is sufficiently small or the applied load is low, the asperity deforms under elastic conditions. The deformation is completely reversible in this case. The elastic contact area, A_e, for an elliptical paraboloid is given as

$$A_e = 2\pi R \frac{\alpha'\beta'}{\gamma'}\omega \tag{6.1}$$

The mean effective radius, R of the asperity is given as

$$\frac{1}{R} = \frac{1}{R_x} + \frac{1}{R_y} \tag{6.2}$$

According to Moes [82], the dimensionless parameters, α', β' and γ', for the elastic contact situations are given as

$$\alpha' = \kappa^{1/3}\left[\frac{2}{\pi}E(m)\right]^{\frac{1}{3}} \tag{6.3}$$

$$\beta' = \kappa^{-2/3}\left[\frac{2}{\pi}E(m)\right]^{\frac{1}{3}} \tag{6.4}$$

$$\gamma' = \kappa^{2/3}\left[\frac{2}{\pi}E(m)\right]^{-\frac{1}{3}}\frac{2}{\pi}K(m) \tag{6.5}$$

The elliptic integrals of the first and second kind, *E(m)* and *K(m)*, can be approximated as,

$$E(m) \approx \frac{\pi}{2}(1-m)\left[1 + \frac{2m}{\pi(1-m)} - 0.125\ln(1-m)\right] \tag{6.6}$$

$$K(m) \approx \frac{\pi}{2}(1-m)\left[1 + \frac{2m}{\pi(1-m)}\ln\left(\frac{4}{\sqrt{1-m}}\right) - 0.375\ln(1-m)\right] \tag{6.7}$$

where,

$$m = (1-\kappa^2);\ \kappa = \alpha'/\beta' \tag{6.8}$$

The asperity curvature ratio, λ, is defined as the ratio of principal curvatures in the major and minor directions of the asperity.

$$\lambda = \frac{R_x}{R_y} \tag{6.9}$$

An approximate relation between the asperity curvature ratio and ellipticity ratio of the asperity is given by Moes [82] as

$$\kappa \approx \left[1+\sqrt{\frac{\ln(16/\lambda)}{2\lambda}-\sqrt{\ln 4}+0.16\ln\lambda}\right]^{-1} \quad \text{for } 0<\lambda\le 1 \tag{6.10}$$

The contact load carried by an elliptical paraboloid asperity under elastic contact conditions is given as

$$F_{N,e}=\frac{4}{3}E^*\left(\frac{\omega}{\gamma'}\right)^{\frac{3}{2}}\sqrt{2R} \tag{6.11}$$

The mean contact pressure, P_m for the Hertzian contact of an elliptical paraboloid is given as

$$P_m=\frac{F_{N,e}}{A_e}=\frac{\sqrt{2}}{\pi}\frac{E^*}{\alpha'\beta'}\left(\frac{\omega}{R\gamma'}\right)^{0.5} \tag{6.12}$$

The critical interference at which the onset of plasticity occurs for the given asperity geometry and material properties is calculated from the maximum Hertzian contact pressure. The plastic deformation initiates when the maximum Hertzian contact pressure exceeds a contact pressure factor, K_v, according to Tabor [85]. The contact pressure factor is equal to 0.6 according to the von Mises yield criterion for the point contact situation. The contact pressure factor is related to hardness of the material and a hardness coefficient.

$$P_{\max}=K_vH;\ P_{\max}=2/3P_m \tag{6.13}$$

Chang, Etsion and Bogy [16], based on Tabor's approach, presented a static friction model using a statistical representation of surfaces. The CEB model treats the static friction as plastic yielding mechanism for the initial inception in the contact. Recently, Lin et al. [84] gave the hardness coefficient related to Poisson's ratio of the material from the von Mises yield criterion as,

$$K_v=0.4645+0.3141\nu_1+0.1943\nu_1^2 \tag{6.14}$$

The critical interference for the onset of plasticity is given from the equations (6.12), (6.13) and (6.14)

$$\omega_1=\frac{\pi^2}{2}(\alpha'\beta')^2\gamma' R\left(\frac{K_vH}{E^*}\right)^2 \tag{6.15}$$

6.2.2 Full plastic contact

If the load of the contacting asperity is increased substantially high, the deformation becomes irreversible and the contact operates in the full plastic regime. In the fully plastic regime, the contact pressure carried by the asperity is equal to the hardness of the material.

Then the contact load and contact area of the plastically deforming asperity are obtained by simply truncating the asperity as given by Abbott and Firestone [83]. For the elliptic paraboloids, the truncated height of the asperity is given as,

$$\omega = \frac{a^2}{2R_x} = \frac{b^2}{2R_y} \tag{6.16}$$

The contact area of the elliptical paraboloid asperity under full plastic conditions from (6.16) is given as

$$A_p = 2\pi\sqrt{R_x R_y}\,\omega \tag{6.17}$$

The plastic contact load of an elliptical paraboloid asperity is given as

$$F_{N,p} = 2\pi\sqrt{R_x R_y}\,\omega H \tag{6.18}$$

An accurate description for the interference to achieve full plastic deformation is not known. It is estimated by using Johnson's criteria for full plastic deformation. According to Johnson [23], full plastic deformation occurs when the contact load equals 400 times the load at first plastic yielding. The plastic contact load at first yielding is calculated by assuming again that the contact pressure equals the hardness of the material.

$$\frac{F_{N,p}^{trans}}{F_{N,e}^{trans}} = \frac{2\pi\sqrt{R_x R_y}\,\omega_2 H}{2\pi R\alpha'\beta'\gamma'^{-1}\omega_1 H} = 400 \tag{6.19}$$

After solving Equation (6.19), the transition interference for the full plastic deformation is given as

$$\omega_2 = C_A \frac{\sqrt{\lambda}}{1+\lambda}\frac{E(m)}{K(m)}\omega_1 \tag{6.20}$$

where C_A is the ratio of contact area at the given load to the critical contact area for the first plastic yield. For the contact problem of a deformable sphere and a rigid flat, the fully plastic regime starts at $C_A = 160$.
For spherical steel contacts, the transition can be further simplified as

$$\omega_2 = 80\omega_1 \tag{6.21}$$

6.2.3 Elastic-plastic contact

The analysis of Johnson [23] shows that the fully plastic deformation starts at a larger load (400 times higher than the initial yielding load) with respect to the initial inception of the plasticity. Francis [86] showed that the fully plastic regime starts when the contact area is about 110 times higher than the contact area at the initial yielding. This suggests that the

range of elastic-plastic deformation is extensive between the initial yielding and full plastic yielding. Zhao et al. [87] proposed an elastic-plastic contact model (ZMC model) by providing a smooth transition between the elastic-plastic and fully plastic contact areas. Zhao et al. used a cubic polynomial expression using the transition interference to join the two asymptotes for the contact area as shown in Figure 6.2. The relative interference is defined as,

$$\delta = \frac{\omega - \omega_1}{\omega_2 - \omega_1} \tag{6.22}$$

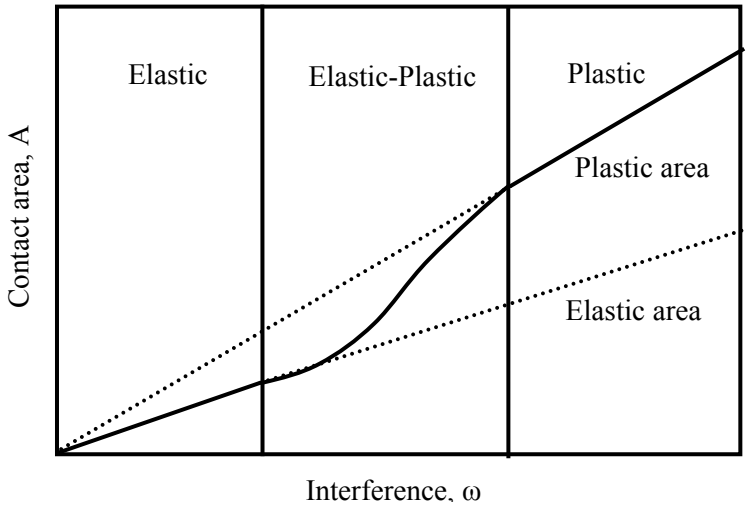

Figure 6.2: Schematic representation of ZMC model.

The contact area during elastic-plastic deformation after scaling is then described as

$$A_{ep} = A_e + \left(A_p - A_e \right)\left(-2\delta^3 + 3\delta^2 \right) \tag{6.23}$$

The elastic-plastic contact load is obtained from the mean contact pressure and the contact area during elastic-plastic deformation is described as

$$F_{N,ep} = A_{ep}\left[H - H\left(1 - \frac{2}{3} K_v \right) \frac{\ln \omega_2 - \ln \omega}{\ln \omega_2 - \ln \omega_1} \right] \tag{6.24}$$

6.3 Unloading of single asperity contact

In deep drawing processes, the coefficient of friction is not influenced by loading and further influenced by repeated loading. When an asperity is deformed at a contact pressure and again subjected to (re)loading at a lower contact pressure, the major deformation mode of asperity is elastic. The reason is that plastic deformation has already happened in the first

loading stage. Reloading will influence the contact area and contact load carried by the deforming asperity. In the elastic deformation mode, the contact load carried is less than the plastic load at the same contact area. Otherwise, the contact area will be higher at the same load during reloading than the initial loading. Since friction is influenced considerably by the contact area, reloading effects are important to the friction prediction. During unloading of the asperity, the asperity geometry will change depending on the deformation mode as shown in Figure 6.3. In the following section, a model will be shown for the reloading of the asperity. The residual interference and radius of the asperity are changed after the initiation of plastic deformation due to asperity flattening. The residual interference, ω_{ul}, and residual radius, R_{ul}, after unloading of the asperity are found with the following assumptions.

1. The deformation of the asperity is perfectly elastic when subjected to the initial contact load.
2. The curvature ratio, ($\lambda=R_x/R_y$), of the asperity remains unchanged after unloading.
3. The initial eccentricity of the asperity, ($e^2=1-b^2/a^2$), remains unchanged after unloading.

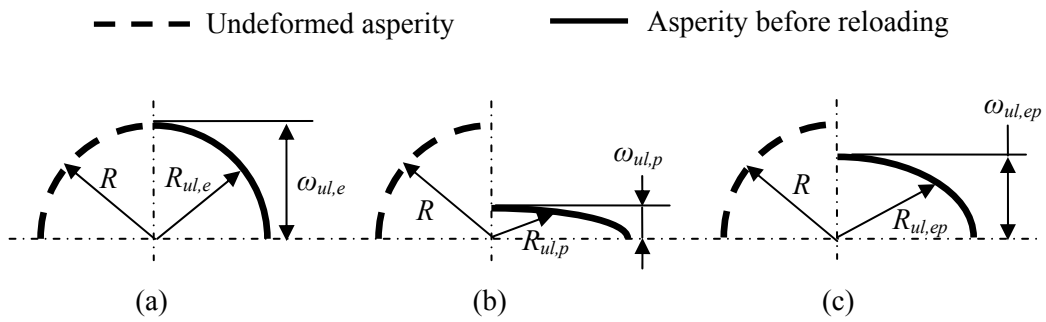

Figure 6.3: Representation of asperity deformation for (a) elastic (b) fully plastic and (c) elastic-plastic.

Assumption 1 is valid if the contact loads do not exceed the previous load. Assumptions 2 and 3 show that the initial geometric ratios of the asperities remains the same. Local friction conditions and stress states at the asperity influence the change of geometric ratios. However, the total contact area is unaffected due to this assumption which is important for the friction model.

6.3.1 Elastic unloading

During elastic deformation of asperity, the contact area and load are calculated according to the Hertzian theory. Once the contact load is removed the asperity deformation is completely reversible, as shown in Figure 6.3 (a). During reloading, the asperity remains elastic and still deforms in the same mode. While unloading the asperity, the residual interference and asperity geometry remains unchanged.

$$\omega_{ul,e} = \omega \; ; \; A_{ul} = 0 \; ; \; R_{ul,e} = R \tag{6.25}$$

6.3.2 Elastic-plastic unloading

During unloading of the elastic-plastic contact, a significant amount of elastic recovery takes place depending on the degree of plastic deformation. The residual geometry and interference are also changed after the unloading process due to plastification as shown in Figure 6.3 (c). When the contact load is removed from the asperity, the plastic deformation has already happened. Hence when reloaded to the same contact load, N_{ep}, the whole deformation process is elastic as mentioned before. The residual radius, $R_{ul,ep}$, and residual interference, $\omega_{ul,ep}$, after unloading are calculated by solving the two equations (6.26) and (6.27) such that the deformation will be elastic upon reloading.

$$F_{N,ep} = \frac{4}{3} E^* \left(\frac{\omega_{ul,ep}}{\gamma'} \right)^{\frac{3}{2}} \sqrt{2R_{ul,ep}} \tag{6.26}$$

$$A_{ep} = 2\pi R_{ul,ep} \frac{\alpha'\beta'}{\gamma'} \omega_{ul,ep} \tag{6.27}$$

6.3.3 Fully plastic unloading

During unloading from plastic deformation mode, the elastic recovery of the asperity is small. Hence the radius of the asperity becomes very large and also the residual interference is small as shown in Figure 6.3 (b). Even then, during reloading of the asperity the contact load and contact area should be according to the elastic deformation mode. The residual radius, $R_{ul,p}$, and residual interference, $\omega_{ul,p}$, after unloading are found by solving the two equations (6.28) and (6.29) for the maximum plastic load that occurred earlier, $F_{N,p}$.

$$F_{N,p} = \frac{4}{3} E^* \left(\frac{\omega_{ul,p}}{\gamma'} \right)^{\frac{3}{2}} \sqrt{2R_{ul,p}} \tag{6.28}$$

$$A_p = 2\pi R_{ul,p} \frac{\alpha'\beta'}{\gamma'} \omega_{ul,p} \tag{6.29}$$

6.4 Reloading of single asperity contact

In deep drawing processes, a substantial amount of sliding takes place between the blank holder and sheet material. During sliding, the contact load varies at a certain asperity. In this section, a single asperity contact model is shown for loading/reloading conditions with a rigid flat contact as described in the earlier sections. During the first loading, the asperity will undergo different modes of deformation. With the subsequent loading at the same contact load, the asperity deformation is assumed to be elastic. Being in the elastic deformation mode during reloading, the asperity will follow Hertzian deformation laws.

The numerical results of the loading and reloading deformation process are shown in Figure 6.4. The input values for the material parameters used in the calculation are given in Table F.1 (see Appendix F) and the asperity radius is taken as 10 μm. A plot of non-dimensional interference and non-dimensional load for a given surface is shown in Figure 6.4. The interference and load in Figure 6.4 are normalized by their critical values at which the transition from elastic to plastic regime occurs. Non-dimensional interference, $\omega/\omega_1=1$, means that plastic deformation starts where the reloading behaviour is different from the loading behaviour. It can be seen that the reloading curves at different interferences have the same slope i.e. contact stiffness. The reloading curve is non-linear, which is similar to the indentation experiments on micro and nano scale indentations by Oliver and Pharr [88] and [89]. One important observation from the indentation experiments is that the shape of the indentation after reloading is different and the material recovers elastically. The impression with the spherical indentation in metals resulted in a larger radius than the indenter. During the experiments, the material is loaded and unloaded a few times before the force-displacement behaviour becomes completely reversible. A limited amount of plasticity occurs in few loading cycles. This can be due to material creep during loading and unloading cycles. However, for highly elastic materials like silica and sapphire there is no difference in the unloading cycles. Since the loading/reloading paths do not vary from a large magnitude within the few loading cycles, the effects are not taken in to account in this model.

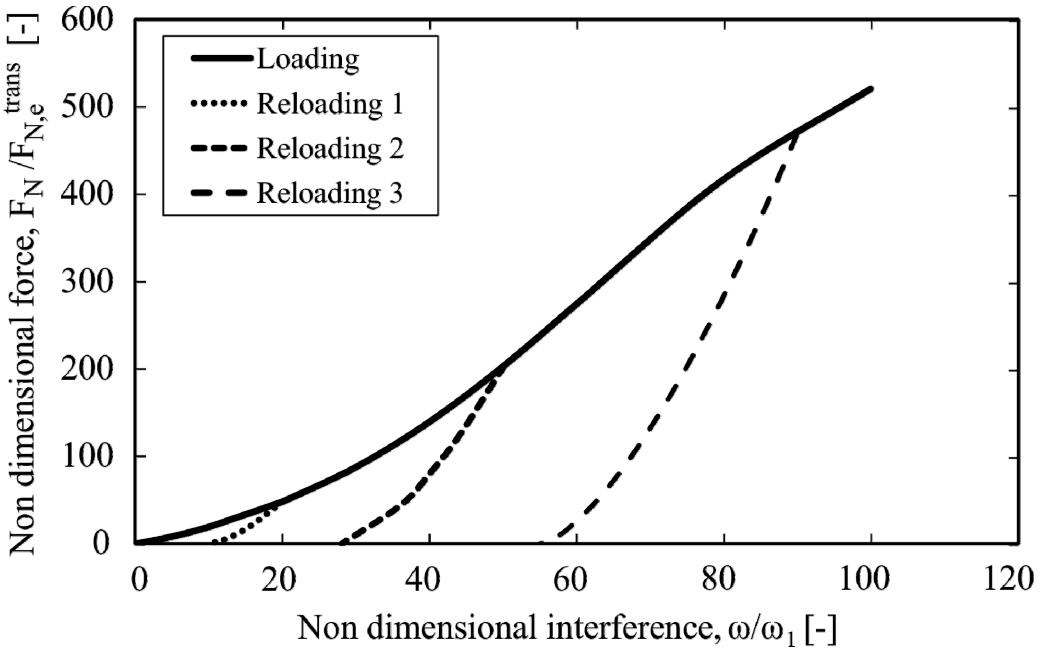

Figure 6.4: Force displacement curve for loading/reloading for a single asperity contact.

In Figure 6.5, the contact area development is shown during loading/reloading of the single asperity contact. The contact area is normalized by the critical contact area at which the transition from elastic to elastic-plastic deformation occurs. The contact area during loading

follows the corresponding deformation mode. During reloading, the contact area is linear which is calculated according to the elastic deformation mode.

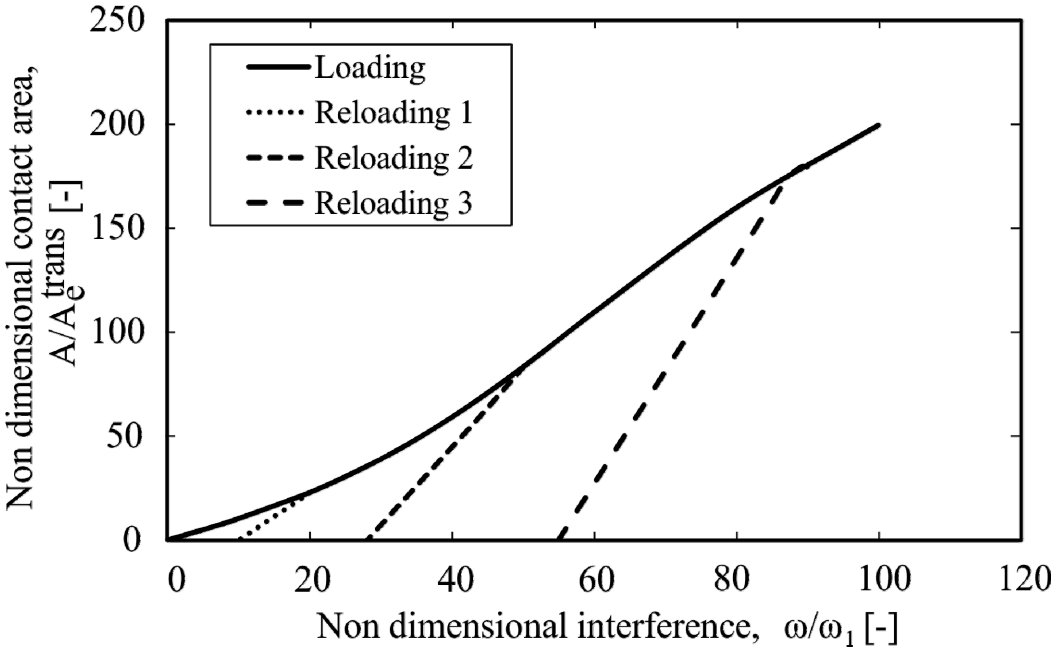

Figure 6.5: Calculated Load-interference relationship for a single asperity contact with a rigid flat.

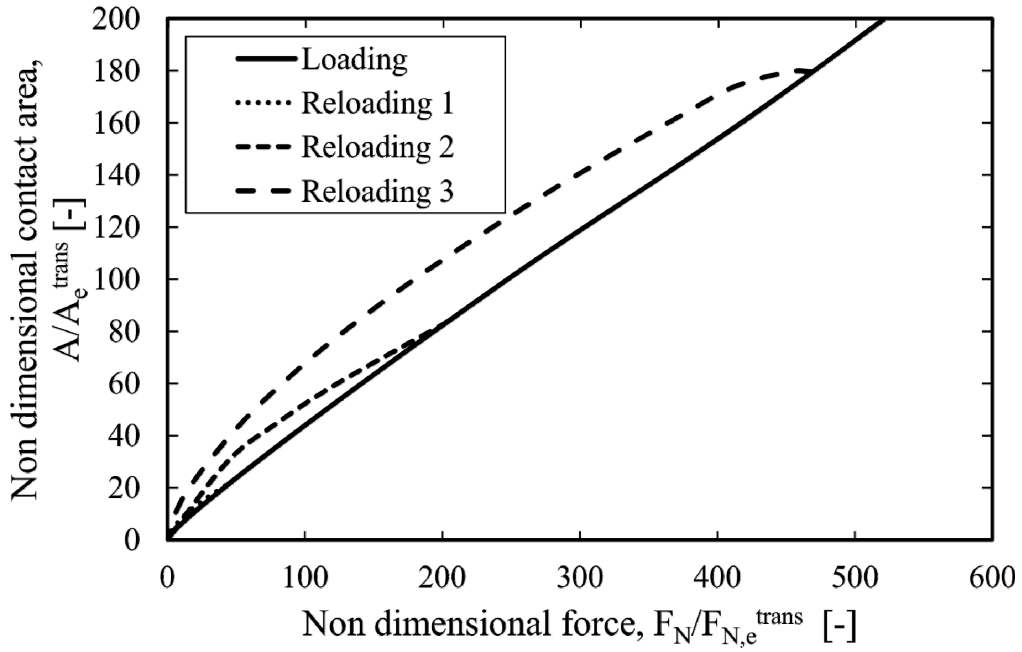

Figure 6.6: Calculated load area relationship for a single asperity contact with a rigid flat.

In Figure 6.6, the contact area development during loading and reloading is shown as a function of the non-dimensional contact load. While reloading at lower loads, the contact area is larger than during the first loading. This is due to the fact that the asperity radius became larger after unloading and also due to elastic conditions. When an asperity deforms elastically, the contact load is lower than the plastic conditions for the same interference level. Hence, the asperity has to deform more for the same contact load.
In Figure 6.7, the change of contact radius is shown during the loading process. For elastic deformation i.e. $0 < \omega/\omega_1 < 1$, the residual remains unchanged. As the plasticity progresses with the increased load the asperity radius increases which can also be seen in indentation experiments of [88] and [89]. The asperity radius continues to increase with the contact load and becomes flattened with a larger radius. In practice, the asperity reaches infinite for large plastic deformation conditions. Next, the influence of the asperity radius is compared in the figure. The reference radius of the asperity, R_0, is taken as 10 μm. When the asperity radius is reduced ($R/R_0 = 0.1$), there is more plastic deformation as the smaller asperities deforms plastically. The non-dimensional residual radius of the asperity is higher than the reference asperity. When the asperity radius is increased ($R/R_0 = 2$), the asperity deforms more in the elastic-plastic regime and the elastic recovery is greater. The residual radius will be much closer to the original radius of the asperity after unloading.

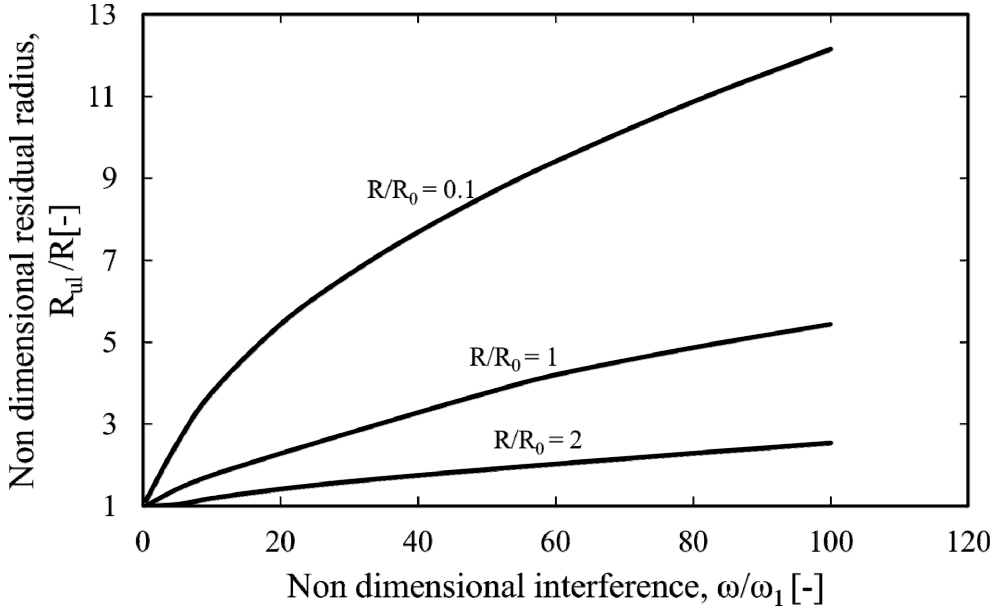

Figure 6.7: Calculated interference residual radius of the asperity after unloading.

6.5 Reloading of surfaces

The asperity loading/reloading model explained in the previous section is used in a multi-asperity contact situation. A typical surface from DC06 sheet material (see Appendix C) is used for reloading of the surfaces. The asperities are characterized by elliptical paraboloids for the given load as described in Section 5.2. In Figure 6.8, the development of nominal

contact pressure is shown with the approach of the surface. At the beginning of the approach (i.e. high surface separation), there are only a few asperities in contact and the contact pressure is low. When the surface separation is decreased further, the contact pressure increases rapidly as there are large numbers of asperities comes into contact where the mean plane of the surface lies. When the surface separation is decreased, the asperities will merge with the neighbouring asperities. Larger asperities are formed when the surface separation is low. The figure also shows the reloading path when the surface is unloaded after a certain contact pressure is reached.

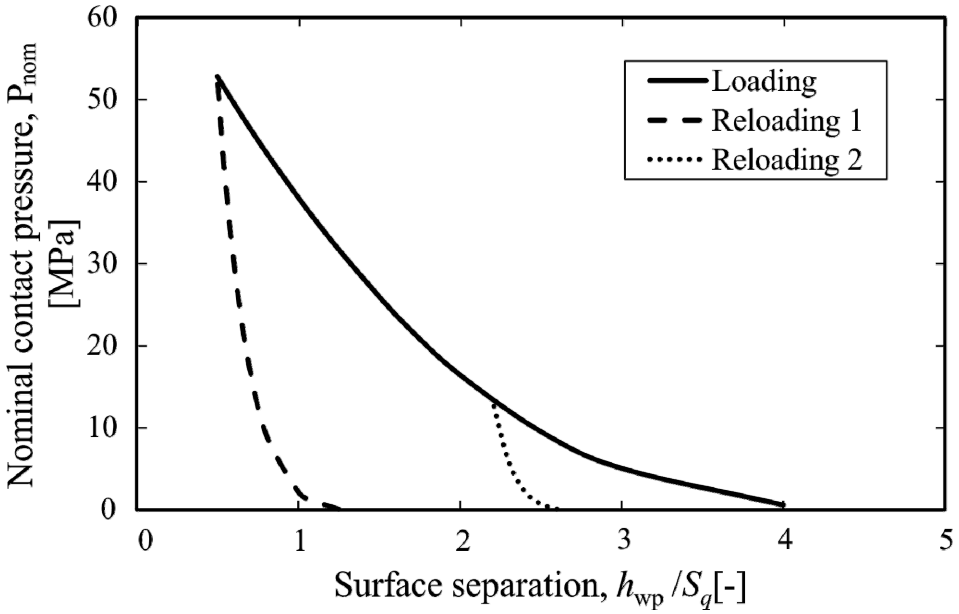

Figure 6.8: Calculated nominal contact pressure during loading/reloading of the surface.

The fractional contact area during loading and reloading is shown in Figure 6.9. During loading, the contact area increases as the surface separation increases. When the surface is reloaded the contact area is larger, since the asperities are elastically deforming (as shown for the single asperity contact, see Figure 6.6). The fractional contact area during reloading will increase steeply if there is a large plastic deformation of the surface during the initial loading. Smaller asperities undergo complete plastic deformation since the contact pressures are high. Larger asperities undergo elastic-plastic deformation and a considerable part of the asperity deformation is recovered.

The plot of contact area of the asperities is shown for the given DC06 surface in Figure 6.10. The surface is subjected to a maximum contact pressure of P_{nom} = 50 MPa and reloaded. During loading, the bigger contact patches undergoes elastic-plastic deformation, while some smaller contact patches undergoes large plastic deformation. Minor (smaller) contact patches are not found during the reloading at the same contact pressures (P_{nom} = 5, 25 MPa) when compared the contact area at P_{nom} = 50 MPa. This is due to large amount of plastic deformation experienced by smaller asperities. The residual interference of these smaller asperities is lower than the separation during the reloading. Meanwhile, the large contact patches shows increased contact area during reloading at P_{nom} = 5 and 25 MPa. This

means the large asperities supports the contact load elastically by increasing its contact area. It can be seen that the area of the major (bigger) contact patches while reloading are larger than at the first loading for the same load.

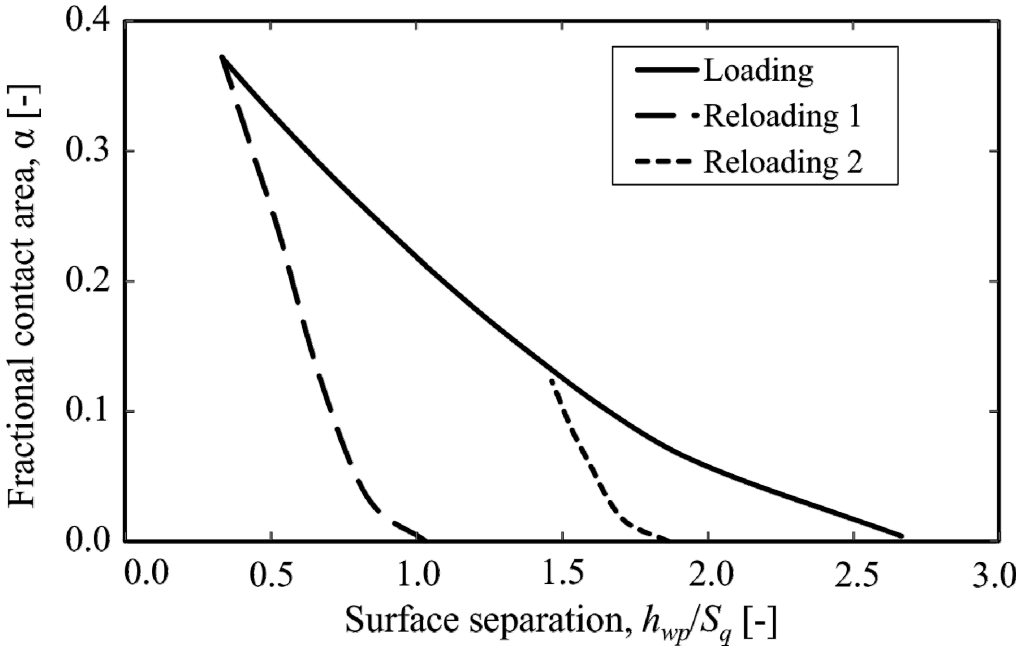

Figure 6.9: Calculated fractional contact area development during loading/reloading.

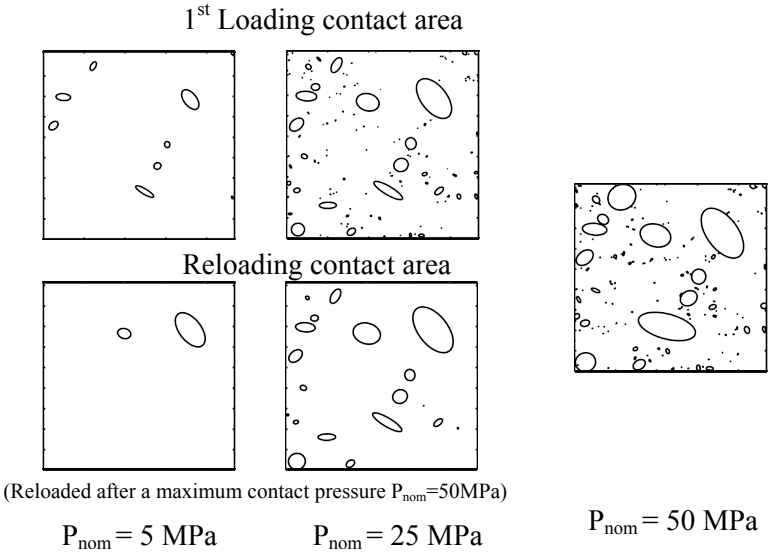

Figure 6.10: Contact area development for the surface during loading/reloading for a maximum P_{nom} = 50MPa.

6.6 Elastic plastic ploughing contact model

The coefficient of friction is caused by interfacial shear and ploughing effects. For friction modelling, the geometry of the indented tool asperities into the deformed contact patches of the workpiece is important. With the indented geometry of the tool asperity, the coefficient of friction can be calculated using Challen and Oxley's model [10] for ploughing and cutting deformation modes with an interfacial friction factor. In elastic-plastic contact situations, the frontal part of the asperity carries the tangential load during sliding. Under complete elastic conditions, the asperity indents and the material fully recovers after the indenter passed as shown in Figure 6.11. In the elastic-plastic deformation mode, the contact area changes from a complete elliptic area to a semi-elliptic area according to Masen [19]. For fully plastic conditions, the asperity indents and there is no elastic recovery after the indenter has passed. The front half of the asperity will be in contact during ploughing. In elastic-plastic situations, there is elastic recovery depending on the degree of plastification. The contact pressure and area follow from the asperity geometry for the given indentation depth. When there is a plastic deformation, the total deformation is permanent and the contact pressure equals the indentation hardness of the material. The indentation hardness is size and shape dependent. For an elliptical paraboloid asperity, the contact area under ploughing conditions assuming only front half of the asperity makes contact is given as,

$$A_t = \pi \sqrt{R_x^{'} R_y^{'}}\, \omega^{'} \tag{6.30}$$

The contact load for indentation at fully plastic conditions is given as,

$$F_{N,t} = H_{ind}\, A_t \tag{6.31}$$

Similar to the flattening model, the contact load and area for an asperity is calculated for elastic and elastic-plastic deformation with the equations (6.1), (6.11), (6.23) and (6.24). The transition points from elastic to fully plastic conditions are found with the equations (6.15) and (6.20).

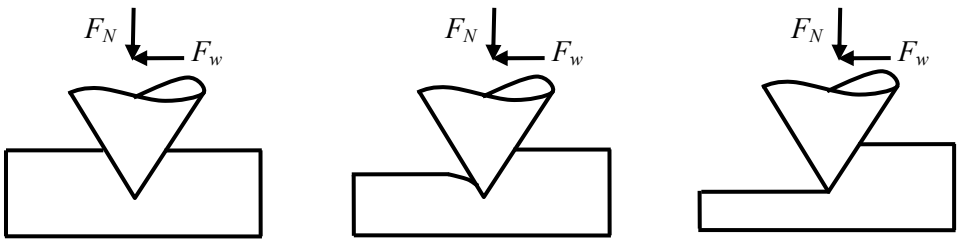

Figure 6.11: Indentation of tool asperity at (a) elastic (b) elastic-plastic and (c) plastic deformation modes.

6.7 Contact analysis of rough surfaces

Depending on the shape and size of the asperities, the indentation may operate in the three modes of deformation. In this section, the contact model is subjected to the analysis of how the contact pressure and surfaces influences the transition from elastic to fully plastic indentations. For this analysis, numerical generated tool surfaces are used as shown in Section 5.6 (see Table 5.1).
In Figure 6.12, influence of contact pressure on the Surface 1 (see Table 5.1) is shown. The plot shows the transition of the asperities from elastic to fully plastic indentation. Non-dimensional indentation depth is the ratio of the indentation depth, ω' to the contact radius of the elliptical base. When the non-dimensional indentation depth is small, the asperity indentation is small or asperity contact radius is large. In this case, the asperity indents in completely or partly elastic manner. As the non-dimensional indentation depth increases, the asperity becomes sharper. The asperity indents plastically. In Figure 6.12, the asperity deformation mode is shown for different nominal contact pressures. From the plot, it can be seen that the indentation of asperities cannot be considered to operate only in the fully plastic mode as discussed in the Chapter 5 and model of Westeneng [18]. When the contact pressure is increased the number of asperities in contact increases and also they merge together to form bigger contact patches. The indentation depth to contact radius ratio of the asperity decreases. The bigger asperities operate in the elastic-plastic indentation mode while the smaller asperities undergo plastic deformation. Although the number of asperities operate in plastic indentation mode is large, they carry less percentage of the total load. The bigger asperities (i.e. low $\omega'/\sqrt{(ab)}$ ratio) operate in the elastic-plastic indentation mode. The percentage of the load carried by the pure elastic mode is negligible.

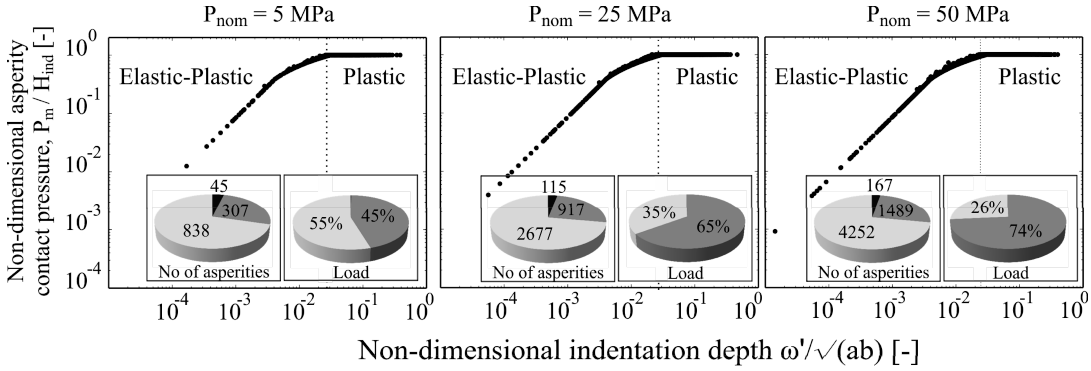

Figure 6.12: Influence of contact pressure on asperity indentation mode (■ - Elastic, ■ - Elastic-plastic, ■ - Plastic).

It is shown in Section 5.9, that the surface roughness of the tool influences the coefficient of friction. The surface roughness indicates how the shape of the asperities is distributed. If the surface is rough, the asperities are sharp. In Figure 6.13, the influence of surface roughness on the asperity indentation mode is shown. If the surface is smooth, the number of asperities in contact is high. The asperities undergo mixed modes of deformation. The majority of the asperities operate in the elastic-plastic mode. When the surface roughness

increases, the elastic-plastic indentation of the asperities are diminishing. For the roughest surface (S_q = 0.4 μm), there are large number of asperities in plastic mode of indentation.

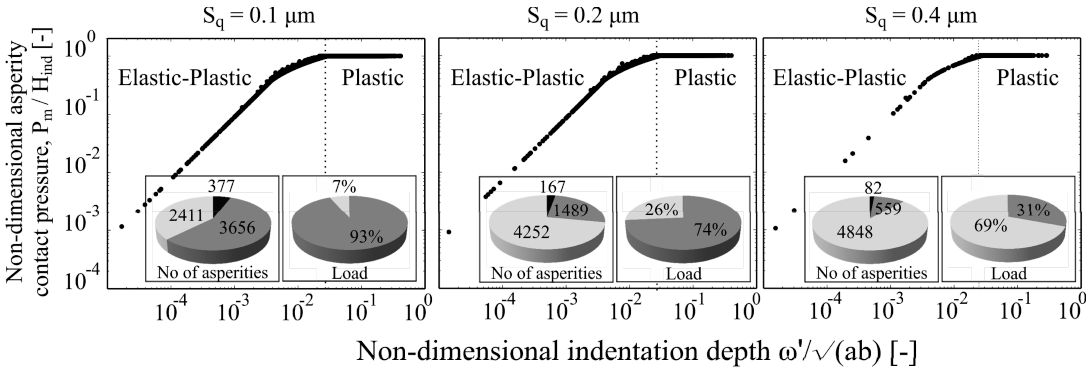

Figure 6.13: Influence of surface roughness on the asperity indentation mode (■ - Elastic, ■ - Elastic-plastic, ■ - Plastic).

In Figure 6.14, the influence of bandwidth parameter of the surface is shown. For a low bandwidth surface, the surface has sharper asperities than the high bandwidth surface. A low bandwidth surface (spiky surface) undergoes more plastic indentation than the high bandwidth surface (smooth surface). It can be seen that there is an influence of the bandwidth parameter on the transition in deformation mode from the percentage of the load carried in elastic-plastic indentation mode but relatively less when compared with other factors. However, the influence of bandwidth parameter on the coefficient of friction is important which is mainly due to the geometry of the asperities as shown in Figure 5.13.

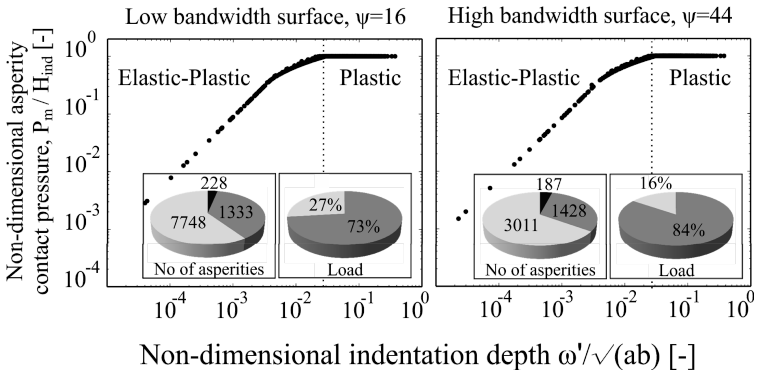

Figure 6.14: Influence of bandwidth parameter on asperity indentation transition (■ - Elastic, ■ - Elastic-plastic, ■ - Plastic).

6.8 Interfacial friction factor

The effect of shear stress between the contacting surfaces is usually expressed by the interfacial friction factor, f_{hk}. The friction factor is dependent on the properties of the boundary layers formed on the surface and the indenter geometry. The friction factor is defined as the ratio of the local shear strength to the shear strength of the deforming material. The local shear strength is dominated by the boundary layers if the contacting surface is flat (i.e. no ploughing). While ploughing, there is a rupture of the boundary layers. Hence, the boundary layers degrade at the local asperity scale during ploughing. Torrance et al. [90] accounted for the degradation of the boundary layers by adding a term called fractional defect of the boundary layers, f_d. The interfacial friction factor at the interface is given as

$$f_{hk} = \frac{\tau_{BL}(1 - f_d) + k f_d}{k} \tag{6.32}$$

The friction factor f_{hk} = 1 means that there are no boundary layers and the surface is chemically clean. The shear strength of the surface is equal to the shear strength of the bulk material. Kopalinsky and Black [91] studied the influence of metallic sliding during indentation. The experiment was done using a hard wedge, representing an upscaled asperity under boundary lubricated conditions. The main objective of the experiment is to study the effect of forces and stresses in wave-wedge formation from initial indentation to steady state sliding. They estimated the friction factor to be around f_{hk} = 0.68 for wedge indentation using slipline analysis. Hokkirigawa and Kato's [47] experiments on steel also show that the interfacial friction factor for ploughing and cutting modes are between 0.5 and 0.9 depending on the degree of penetration. This shows that under the local asperity conditions, the boundary layer properties are degraded. The influence of the degradation factor on the coefficient of friction is shown in Figure 6.15 for the contact between two surfaces. The coefficient of friction is calculated for three different rough surfaces of DC06. The error bar shows the variation due to the different surface measurements of the sheet material surface. To achieve the high friction factor estimated by [90] and [91] for local asperity conditions, the degradation factor (f_d) can be in the range of 0.5-0.7. The coefficient of friction increases with degradation of the boundary layers as shown in Figure 6.15.

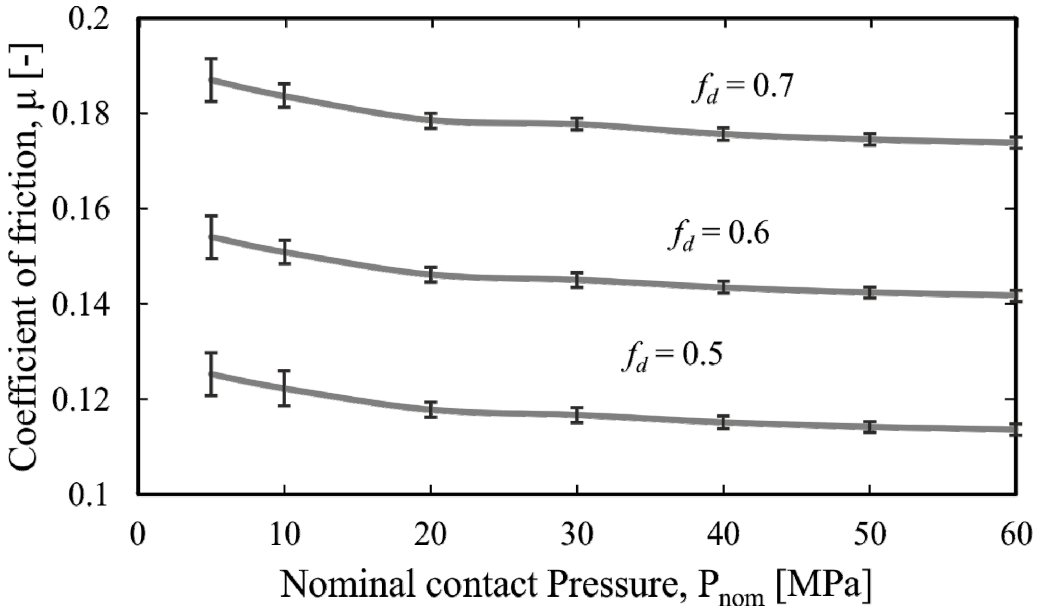

Figure 6.15: Influence of boundary layer degradation.

6.9 Evolution of friction conditions during reloading of surfaces

The coefficient of friction is calculated with the asperity deformation model explained in Section 6.5 and the ploughing model explained in Section 6.6. The coefficient of friction (shown in Figure 6.16) during loading and reloading is calculated with the contact models described before. During loading, the coefficient of friction decreases with the increase of contact pressure. This is due to clustering of tool asperities which plough through the workpiece surface. The asperities cluster together and forms blunt contact patches. This results in lowering of friction with the contact pressure. This trend of friction is dominant for the deformation dependent mechanism, i.e. ploughing. During reloading for the same contact pressures, the larger contact area is formed (see Figure 6.6 and Figure 6.10). This results in clustering of asperities which reduces the coefficient of friction. For the same maximum contact pressure (P_{nom} = 30 MPa), there is no difference in the friction as the original contact pressure is reached.

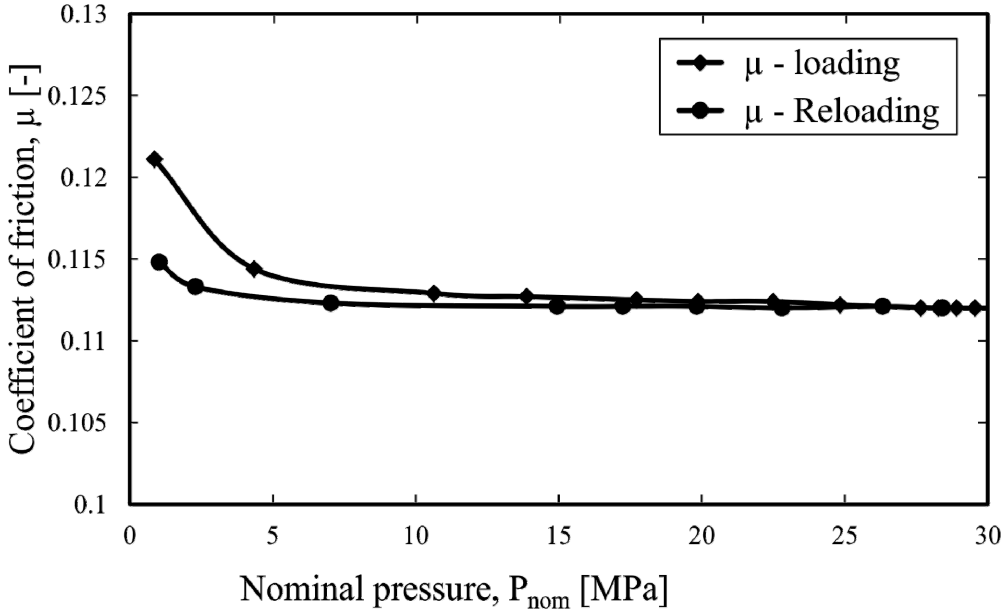

Figure 6.16: Coefficient of friction during loading/reloading.

6.10 Summary

In this chapter, a single asperity contact model has been shown for the contact occurring between a rigid flat and an asperity. In deep drawing processes, the deformation of the asperity is affected by its geometry as well as the loading/reloading conditions. The single asperity model describes different modes of deformation – elastic, elastic-plastic and plastic modes. The asperity geometry is characterized deterministically with elliptical paraboloid shapes. It has been shown already in Chapter 5 that the deterministic approach is better in terms of description of the asperity geometry. The contact model is extended to elastic-plastic contact situations for both asperity deformation and ploughing.

Loading and reloading of the asperity is considered with a simple approach. The asperity is assumed to deform completely in elastic mode during reloading if the previous load is not exceeded. After unloading, the geometry of the asperity changes depending on the deformation mode. The unloaded geometry of the asperity is calculated using the elastic deformation principles. After unloading, the original asperity geometry (curvature ratio and ellipticity of the asperity base) is assumed to be same. Results have been shown for loading and reloading of the asperity. The single asperity model is extended to multi-asperity contact situations. While reloading, the contact area and load differs from the first loading behaviour. A contact analysis of numerically generated tool surfaces is done for different surface roughness, contact pressure and bandwidth parameter. The results show that the surface roughness related factors influence the transition of indentation from elastic to fully plastic conditions.

To calculate the coefficient of friction, the indented geometry is used to calculate the attack angles during ploughing. At the very local contact conditions of ploughing, the boundary

layer properties of the lubricant fail due to high contact pressures or flash temperatures. A boundary layer degradation factor is used in the slipline model of Challen and Oxley to better the friction calculation. The friction factor increases with the degradation of boundary layers. Further, the contact model has been applied to loading and reloading of the surfaces. The coefficient of friction is calculated for loading and reloading of surfaces. While reloading, the coefficient of friction is reduced due to the change in the asperity geometry.

Chapter 7
RESULTS AND VALIDATION OF THE FRICTION MODEL

7.1 Introduction

In this chapter, the developed contact model is compared with the experimental results. The experiments are performed under laboratory conditions since the friction at the local contact conditions is difficult to measure in the actual deep drawing processes. In the actual deep drawing operation, sheet material is pulled over the die. The friction tester simulates the same condition by sliding the sheet material over the stationary tool with constant contact pressure and sliding velocity. The friction model calculates the coefficient of friction with the measured workpiece and tool surfaces, material properties of the sheet material and given contact pressure. The experiments are performed in the boundary lubrication regime. Finally, the measured friction values are compared with the calculated values to check the validity of the friction model.

7.2 Experimental Setup

The rotational friction tester (RFT) developed at Tata Steel is used to measure the coefficient of friction which occurs between the sheet and tool material. A schematic representation of the friction tester is shown in Figure 7.1. The RFT can be used in different ways to study the friction dependency on various contact pressures, sliding conditions and lubrication conditions. The RFT consists of a rotating platform where the sheet material material is placed. The tool is represented by three flat notches which contact the rotating sheet material with a hydraulic actuator. Three flat notches are machined to the same height level, which ensures that the pressure is evenly distributed over the three notches. The allowable deviation should be smaller than the surface roughness of the sheet material. For this purpose, notches are carefully polished. As the notches are flat to a high accuracy, the contact pressure is evenly distributed over the surface of the notch. The contact pressure can be varied by the choice of notch sizes and hydraulic pressure. The elastic deformation of the tool is reduced by making the punches relatively thick and stiff. A computer controlled, brushless servo motor with low inertia reduction gear drives the specimen holder, which allows a greater flexibility for position and speed control.

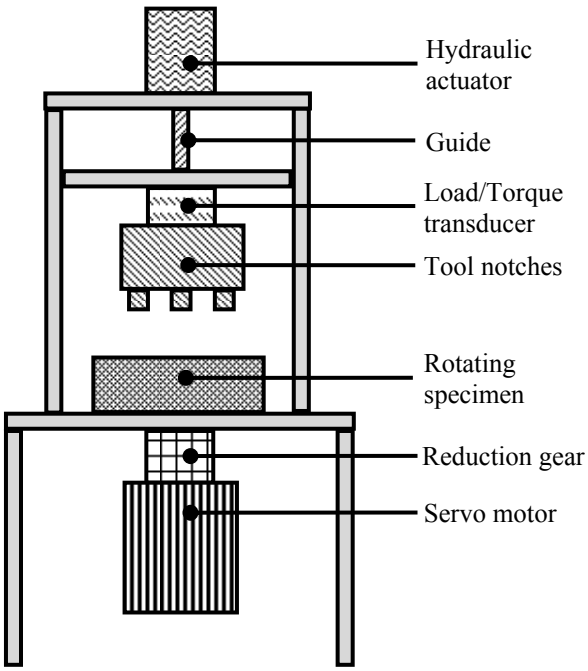

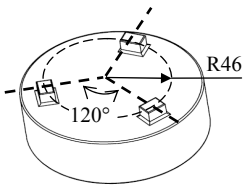

RFT Tool

Rotational frictional tester	
Pressure	5-60 MPa
Sliding velocity	10 mm/s
Mean contact area of notch	52.3mm^2
Mean radius of notch centre	46 mm

Figure 7.1: Schematic representation of Rotational friction tester.

7.2.1 Sheet material specimen

The sheet material material chosen here is uncoated DC06 EDT (Electrical discharged textured) cold rolled steel material which is typically used for deep drawing processes in the automotive industry. The sheet material is cut to a size of 120x120mm and cleaned with acetone and alcohol to remove any surface contaminants. A typical deep drawing oil, Quaker N6130, is applied on the sheet material surface. This lubricant is a conservation oil with deep drawing lubrication properties. The experiments are performed at room temperature conditions. The lubricant has a dynamic viscosity of 55 mPa·s at 22° C. The lubricant is controlled to an amount of 0.6 g/m^2 during oiling of the sheet material by using a mass balance. The sheet material specimen has a roughness in the order of S_q = 1.7 μm. A low amount of lubrication compared to the surface roughness and relatively low sliding velocity indicates that there will be no hydrodynamic lubrication effects. The experiments are therefore performed in the boundary lubrication regime.

7.2.2 Tool Specimen

The tool is made of three square notches made from uncoated tool steel material of grade DIN 1.2510. The notches are finely ground to a roughness, S_q = 0.08 μm by a lapping process so that there is a complete contact with the sheet material. The tool is supported in a central pivot system which will ensure uniform distribution of the load. The dimensions of the square notches are 8x8 mm. The notches are placed at a regular interval of 120° in a circular pattern of mean radius 46 mm to the centre of notch.

7.2.3 Testing procedure

The lubricated sheet material is placed on the rotating platform and clamped firmly. The tool specimen comes into contact with the sheet material and the pressure is applied by the hydraulic actuator system. The nominal contact pressure between the sheet material and tool is applied in the range of 5-60 MPa. The applied load and frictional torque is measured by means of transducers. The sliding velocity of the rotational friction tester is kept constant at 10 mm/s, corresponding to the boundary lubrication regime. Before the test, the tools are cleaned to remove any lubricant present. Experiments are performed in duplicate to measure the variation within the tests. A typical measurement for the coefficient of friction is shown in Figure 7.2. The figure shows the measured coefficient of friction for a rotational movement of 120°. The coefficient of friction remains constant over the sliding distance, except for the initial static friction which is higher.

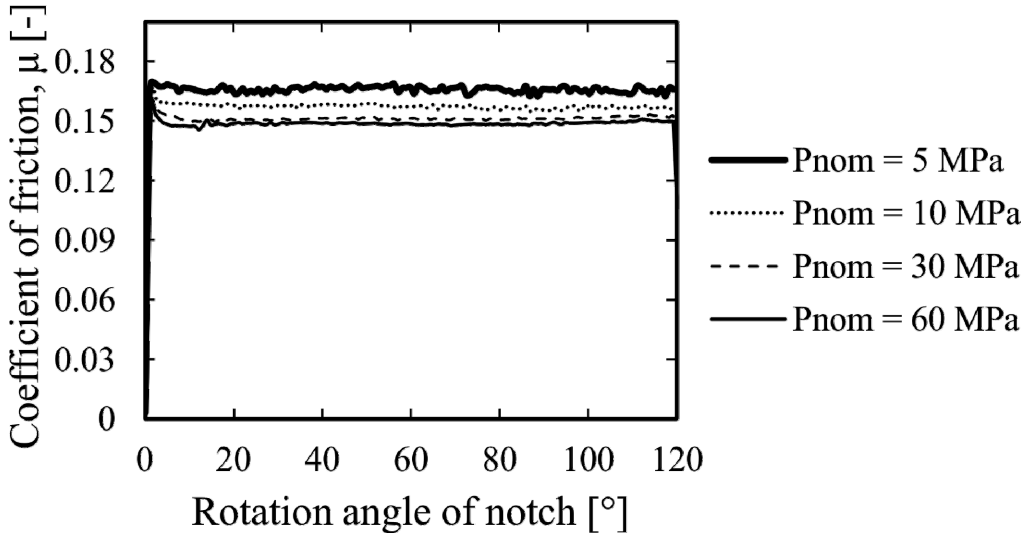

Figure 7.2: Typical friction measurement for different nominal pressure from RFT.

7.3 Results

The mean coefficient of friction is obtained for various contact pressures using the RFT as shown in Figure 7.3. The mean coefficient of friction is calculated within the rotation angle of 20-100° to neglect initial static friction and tail end measurement errors. The coefficient of friction has been also calculated using the contact model explained in Chapter 6 for three different measured surfaces of DC06 sheet material and measured RFT tool surfaces. The input material parameters for the contact model is given in Table F.1 (see Appendix F). The measured surfaces are shown in Figure C.1 and Figure C.2 of Appendix C. The error bars shown in the calculated coefficient of friction indicates the variation with respect to the different sheet material and tool surfaces used. The interfacial friction factor is adjusted by the boundary degradation factor to correlate with the experimental results. The friction

factor, f_{hk} at the local asperity is found to be 0.6 which is also reasonable from the single asperity results of [47], [90] and [91] for ploughing and cutting modes of deformation (f_{hk} = 0.5-0.9) in steel under lubricated conditions. The model predicts the trend of the friction with the contact pressure with a high degree of accuracy.

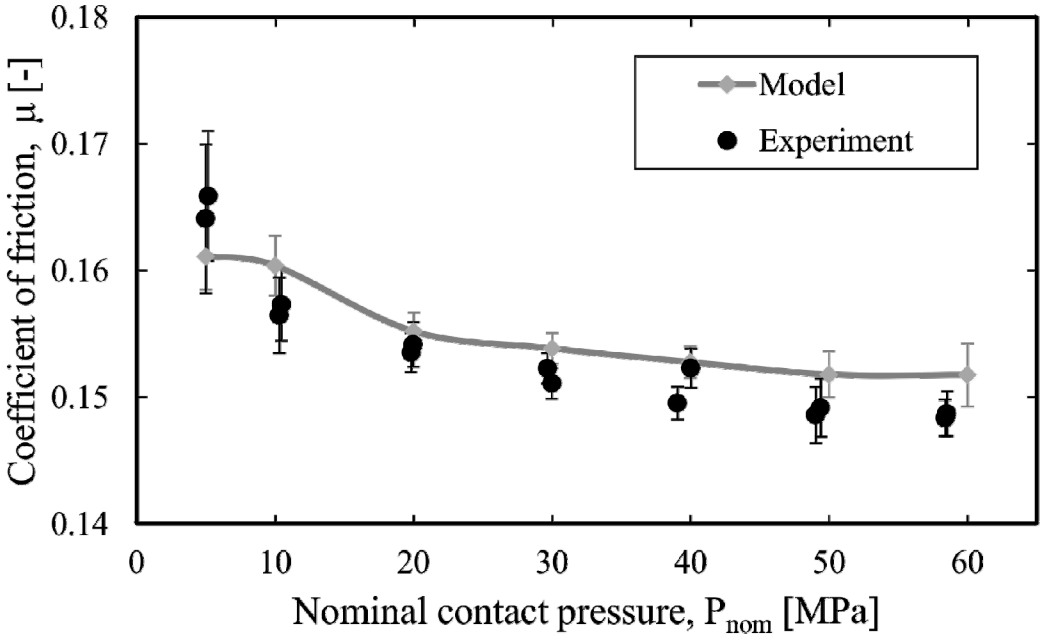

Figure 7.3: Comparison of the coefficient of friction with the experiment and model.

7.4 Application of the friction model to a cup drawing process

In Chapter 4, a pressure profile under the blank holder region of a cup drawing FE simulation (see Figure 4.9) is shown in Figure 4.10. The nominal contact pressure for three different drawing depths (10, 20 and 25 mm) is used to calculate the coefficient of friction with the developed model. For a better understanding of the different effects in the friction model, the coefficient of friction is calculated in different scenarios as follows,

- Comparison of Westeneng's statistical model and deterministic model only with normal loading as discussed in Section 7.4.1.
- Influence of lubrication effects in statistical model with normal loading and stretching as discussed in Section 7.4.2.

7.4.1 Comparison of statistical and deterministic model

The coefficient of friction calculated using the statistical model and deterministic model is compared in Figure 7.4. The statistical model of Westeneng in the low contact pressure ranges predicts an increase of friction as the contact pressure increases. At very high

pressures, the coefficient of friction decreases with the increase in contact pressure as shown in Figure 7.5.

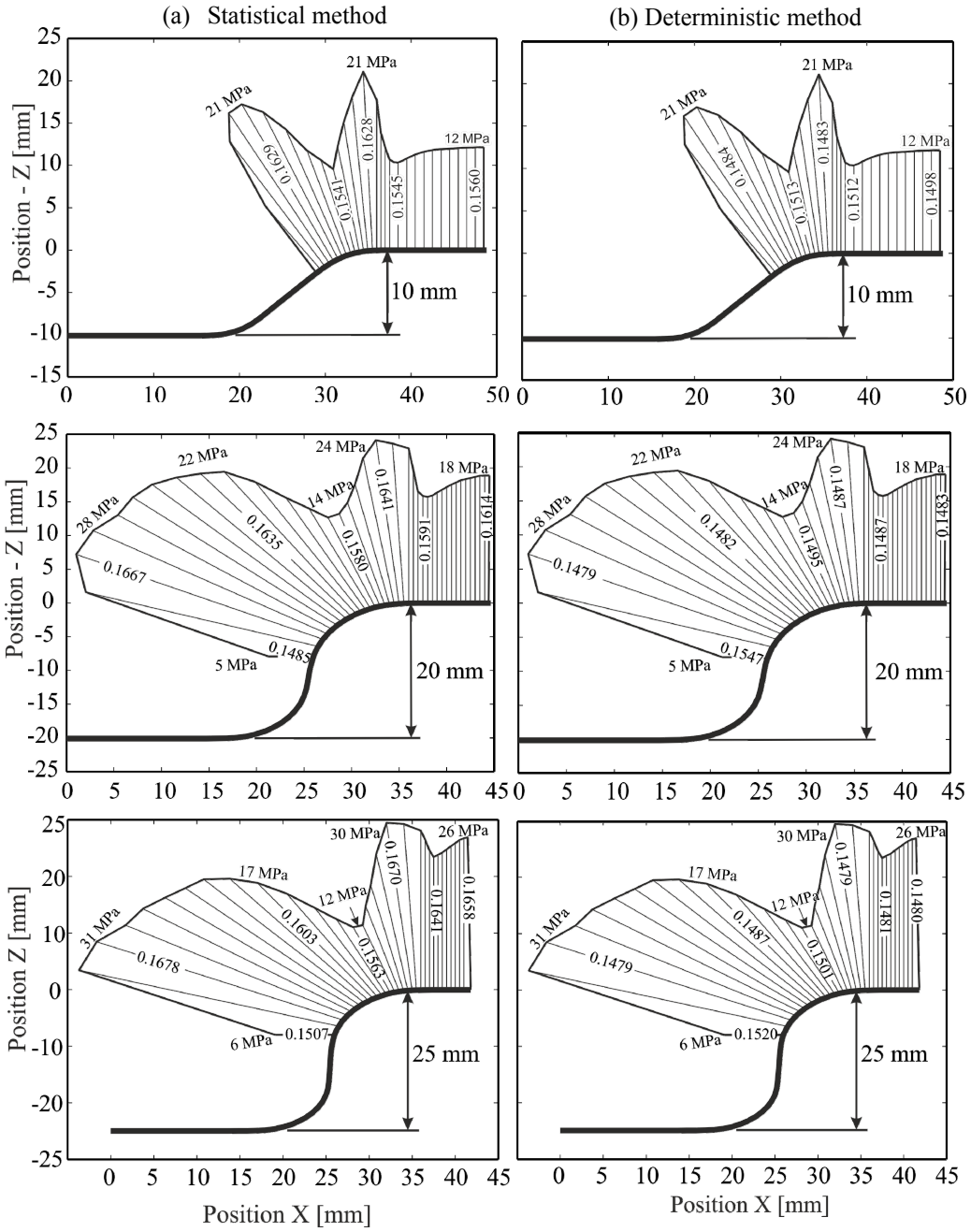

Figure 7.4: Comparison of statistical and deterministic friction model.

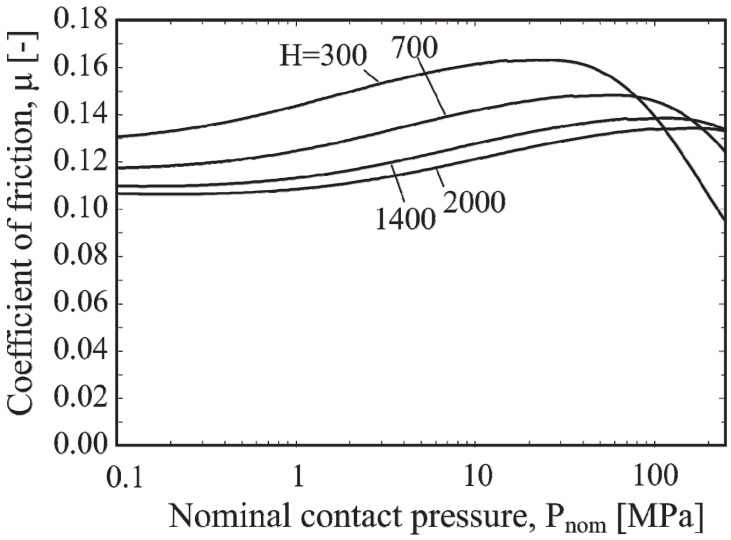

Figure 7.5: Coefficient of friction calculated using statistical model for different hardness of the sheet material (from Westeneng [18]).

The deterministic model predicts that the coefficient of friction generally decreases as the contact pressure increases. This is in accordance with the experiments. The incorrect trend of friction observed in the statistical method is due to the load-independent contact model for the tool indentation (i.e. no consideration of merging of asperities) and full plastic deformation mode.
With the deterministic model, the following friction conditions are found with cup drawing simulations. The contact pressure in the blank holder region is low and the coefficient of friction is high. When the sheet material passes over the die rounding region, the contact pressure peaks and the friction is low. At the exit of the die rounding region, the coefficient of friction increases due to decreasing contact pressures. This is commonly observed for all the stages of the deep drawing operation. At the beginning of the drawing operation, the coefficient of friction is high and reduces as the drawing depth increases, due to the change in the contact pressure conditions. The previously developed statistical model [18] predicts an opposite trend for the cup drawing simulations as shown in Figure 7.4.

7.4.2 Influence of hydrodynamic lubrication

The hydrodynamic lubrication model is coupled here with the statistical method only. In the contact model, the asperity flattening due to normal loading and stretching are considered. When the results from only normal loading (see Figure 7.4 (a)) and normal loading with stretching (see Figure 7.6) are compared, an increase in the coefficient of friction is observed. The statisitical model shows that the coefficient of friction increases with the increase in fractional area which is due to the increase in number of tool summits.

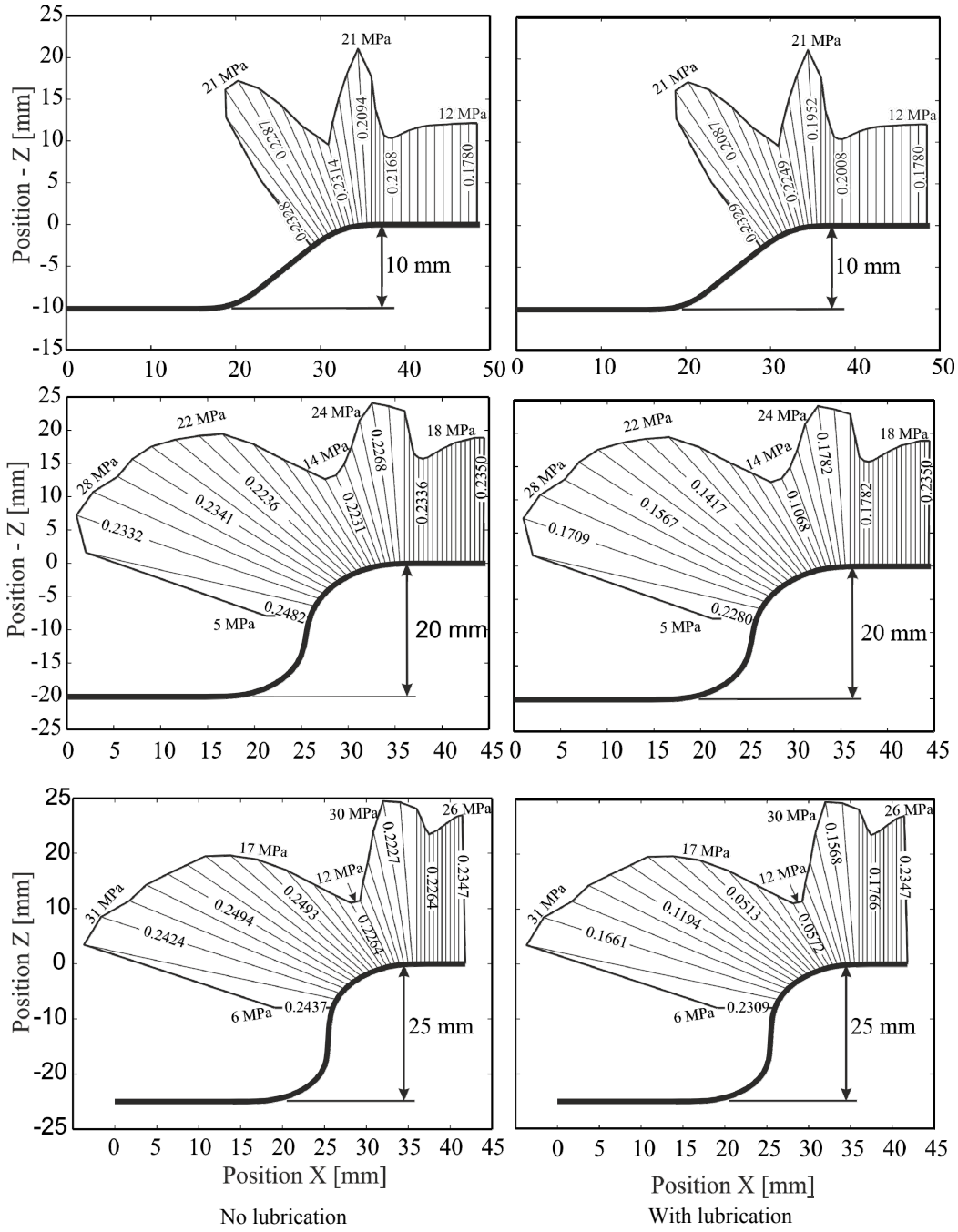

Figure 7.6: Influence of hydrodynamic lubrication on friction.

The illustration here is to show only the effect of mixed lubrication during the forming process. At the beginning of the drawing operation, there is not enough lubricant pressure generation (see Figure 4.10) and the system operates predominantly in a boundary lubrication regime. As the deep drawing operation progresses, the lubricant pressure is

gradually generated and the system reaches mixed lubrication around the die rounding region, as seen in Figure 4.10. Hence the coefficient of friction reduces due to the load shared by the lubricant, as shown in Figure 7.6.

7.5 Summary

The coefficient of friction depends mainly on the interaction between the surfaces, material properties and environmental conditions. A friction model has been developed considering these interactions. This chapter focused the friction measurement in laboratory conditions and validation of the friction model. Experimental results are obtained using the RFT as a function of contact pressure in the boundary lubrication regime. The contact model is applied with input parameters from the surfaces used in experiments and material parameters. The capability of the friction model to predict the coefficient of friction is demonstrated with the experiments. The coefficient of friction is found to agree with the experimental results by using an estimated value for the interfacial friction factor which is within the range of the experiments and the nominal values prescribed in the literature. The model predicts the friction behaviour well within this range of contact pressure using the asperity deformation and ploughing mechanism under boundary lubrication conditions.
Finally, the developed model is applied to a cup drawing simulation. The input parameters for predicting the coefficient of friction is obtained from the material parameters and process conditions from FE simulation. The statistical and deterministic approaches are compared for the friction conditions. The statistical method predicts the increase of the coefficient of friction as a function of contact pressure. The deterministic method predicts better contact conditions than the statistical method which is already shown to be consistent with the experimental results. The effect of mixed lubrication on the coefficient of friction is also shown with the statistical model. The coefficient of friction decreases due to mixed lubrication near the die rounding region. The friction model predicts the contact conditions in the boundary and mixed lubrication regimes well.

Chapter 8
CONCLUSIONS AND RECOMMENDATIONS

8.1 Introduction

In this thesis, a model has been developed to describe the contact and friction behaviour in deep drawing processes. The coefficient of friction is calculated with the following friction mechanisms: shear of the boundary layer, shear of the lubricant and ploughing. In this final chapter, the important conclusions of the research work are outlined along with the recommendations for further research.

8.2 Overview of the developed model

The coefficient of friction which is necessary for the finite elements calculations in deep drawing processes is found out from:

- The contact model describing asperity deformation of the soft sheet material surface and indentation of hard tool asperities in to the sheet material.
- Hydrodynamic lubrication effects between the sheet material and tool surfaces during sliding.
- Ploughing of indented tool asperities through the sheet material during sliding.
- Boundary layer properties specific to the metal-lubricant combinations for deep drawing processes.

For the contact model, both a statistical and a deterministic representation of the surfaces have been used. In the initial phase of the research, the friction model with hydrodynamic effects is developed from the existing contact model of Westeneng [18]. Later, the limitations of using a statistical representation of the surface led to the development of the contact model with a deterministic approach. The surface lay, bandwidth spectrum and asperity geometry for the contact models are better represented in the new deterministic approach than in the statistical representation.

8.3 Conclusions

This section outlines the most important conclusions from the research performed.

Chapter 2 : Contact and friction in deep drawing processes

In this chapter, a literature survey on the mechanisms which influence the contact and friction behaviour is discussed. In deep drawing processes, shear in the boundary layers,

shearing of lubricant film and ploughing of tool asperities are found to be the important mechanisms. A brief introduction to the modelling approach of the influencing mechanisms is given. Analysis of the typical surfaces from the deep drawing materials shows that the asperity geometry will influence the frictional behaviour.

Chapter 3 : Determination of the boundary layer shear strength

In this chapter, the shear of the boundary layer generated by the lubricant used in deep drawing processes is obtained from the experiments. In literature, the boundary layer shear strength is calculated from the frictional force measured from the experiments and the contact area calculated from the Hertz contact theory as reported in [26], [60], [61] and [62]. The Hertz contact theory is valid only for smooth surfaces and elastic deformation. Hence experiments are performed to determine the shear strength of the boundary layers on the materials used in deep drawing processes. The results are found to be in accordance with the model of Timsit and Pelow [26] when using the Hertz contact area. In this research, the shear strength of boundary layers is calculated with the contact area from BEM calculations for elastic-plastic conditions. The shear strength is found to be nearly independent of the contact pressure which is different from what is reported in the literature. In short, the results show that the shear strength at the local conditions is high and almost independent of the nominal contact pressure.

Chapter 4 : Modelling mixed lubrication for deep drawing processes

In the model of Westeneng [18], the friction conditions are assumed to be in the boundary lubrication regime. However, hydrodynamic effects occur in deep drawing processes due to the asperity deformation process by normal loading and bulk strain. A mixed lubrication model is developed and coupled with the asperity deformation model which also takes in to account of the applied lubrication amount. The influence of surface lay can be incorporated in the mixed lubrication model with flow factors. Further, the mixed lubrication model is applied to a cup drawing process.
The coefficient of friction is found to reduce when hydrodynamic lubrication effects occur. The calculations show that mixed lubrication occurs near the die rounding region. At the beginning of the deep drawing operation, the system operates in the BL regime and transists to the ML regime with increased drawing depth. For a low amount of lubricant (< 1 g/m^2), the system will operate in the BL regime and transits to the ML regime for a higher amount of lubricant (> 1 g/m^2). In the case of severe asperity deformation processes (in particular due to high strain), the system operates predominantly in the ML regime. Further, a transverse surface lay decreases the coefficient of friction, while a longitudinal surface lay increases the coefficient of friction.

Chapter 5 : Deterministic contact and friction model – fully plastic deformation mode

The asperities are represented by a constant mean radius of the asperities and summit density in the statistical representation. In contrast, the asperity geometry changes with surface deformation. A deterministic contact model is used to describe the friction behaviour for the fully plastic deformation condition. According to the calculation results, the coefficient of friction decreases as contact pressure increases, due to merging of asperities. With the deterministic contact model, the anisotropic nature of surface roughness of the surfaces on the frictional behaviour is shown. The coefficient of friction is dependent

on the surface roughness, surface lay and bandwidth parameter. The friction model shows that the coefficient of friction increases in line with the increase of surface roughness, surfaces having a transverse lay and low bandwidth surfaces (spiky surface). The coefficient of friction is strongly dependent on micro-geometric details at low contact pressures. This means that the surface topography has a considerable influence on the coefficient of friction. The sensitivity on the coefficient of friction due to microgeometric details decreases as the contact pressure increases.

Chapter 6 : Loading / reloading of contacting surfaces

During surface deformation, mixed modes of deformation (i.e. elastic-plastic) will occur. In this chapter, the deterministic contact model is extended to elastic-plastic conditions for both the asperity deformation and indentation model. The loading/reloading of the surfaces is included in this approach. The contact analysis of rough surfaces shows that transition from elastic to fully plastic conditions is affected mainly by the surface roughness and contact pressure. The coefficient of friction is shown to reduce when the surface is subjected to reloading at lower contact pressures than the original preload. The influence of the shear strength of the boundary layers is considered to be critical to the friction model. With prolonged sliding, the shear strength of boundary layers increases which can be due to the degradation of boundary layers at the small scale (i.e. asperity level).

Chapter 7 : Results and validation of the friction model

In this chapter, the friction model is subjected to validation by the rotational friction tester. The coefficient of friction has been measured at a low sliding velocity and a low amount of lubricant to ensure that the system is operating under boundary lubrication. The contact model from Chapter 6 is used with the surface roughness measurements from tool and sheet material as an input. The model shows good agreement with the friction experiments. Further, the coefficient of friction calculated using the statistical and deterministic contact model is compared with a cup drawing process. The statistical model shows an increasing friction as a function of contact pressure under deep drawing contact conditions. However, the experiments show a decreasing trend in friction. The deterministic contact model predicts the similar trend of friction in accordance with the experiments. The mixed lubrication model is also applied to a cup drawing processes. The coefficient of friction reduces near the die rounding region due to the mixed lubrication conditions.

8.4 Recommendations

a. Shear in the boundary layer

In this work, experiments were done on a dedicated sliding friction tester for a limited range of pressures with a cylindrical pin (of radius 5 mm). At this moment, the boundary layer friction factor is assumed to be constant in the friction model, which is in agreement with the experiments over the limited range of contact pressures in the experiments. However, additional experiments are necessary to find the relation for the shear strength as a function of contact pressure and tip size in a larger range, as they are present in deep drawing processes. Further, the detailed modelling of the shear in boundary layers is important for the friction model. A chemically formed boundary layer and base material are

typically present on the surface in the boundary lubrication regime. A schematic overview of the surface layers is represented in Figure 8.1. The contacting asperities will penentrate the boundary layer and unreacted base material, depending on the magnitude of contact pressure. For the friction model, the shear stresses can be more accurately modelled by a two layer model (boundary layer and base material layer) as the formation and depletion of the layers is a continuous process. It is also necessary to model the dynamics of adsorption and desorption of the boundary layer. The adsorption rate can be explained by the Arrhenius equation with the activation energy of the material and temperature. The depletion of the boundary layers can be described with a suitable wear model. From the adsorption and desorption rate of the boundary layers, the probability of the asperity contact with the boundary layers contact can be found for the given conditions. Now, the total frictional force contribution can be calculated separately for the boundary layers and base material for the given asperity shape and contact conditions (contact pressure).

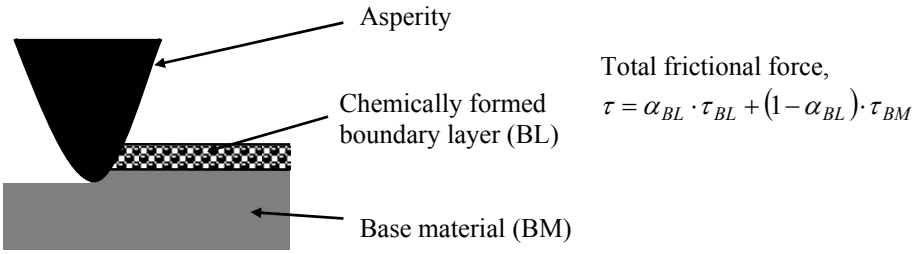

Figure 8.1: Boundary layer modelling.

b. Extension to 2D situations

In this work, the mixed lubrication model treats the hydrodynamic flow as 1D flow i.e. along the radial direction of the axi-symmetric cup drawing process. However, the 2D lubricant flow occurs for other product shapes. Therefore the hydrodynamic lubricant flow must be accounted with the 2D Reynolds equation. Furthermore, asperity flattening due to normal loading and uni-axial stretching conditions has been used in this work. However, a biaxial stress state typically occurs in deep drawing processes. FE methods can be used to describe a relation for the asperity flattening process with biaxial stress states. In FE method, it is difficult to discretize the surface and also the local deformations will be largely affected by the contact formulation. Hence the problem can be reduced to the single asperity scale with simpler shapes such as spherical asperity. FE simulations can be done for different asperity sizes with biaxial stress states to build a relation for asperity flattening. The contact area from the calculation results can be used in the micro-model for multi-asperity conditions. This can be done by formulating function fits of the single asperity results. Alternatively, BEM offers an advantage over the FE method in terms of discretizing the rough surface and contact formulations. Hence a feasibility check on BEM is also advised.

c. Experimental validation

In Chapter 7, the friction model has been validated using RFT experiments. The friction model predicts the trend of the friction well with the experiments by the choice of an approximate interfacial friction factor. The chosen friction factor f_{hk} = 0.6 lies within the appropriate range of values for a boundary lubrication regime. More experiments are needed to verify the friction model with different surface roughness properties to find out whether this friction factor is acceptable. With the experimental setup used, the friction can be measured only due to normal contact pressure. An experimental setup (for example a linear friction tester in which a strip of sheet material is subjected to bulk strain [1]) with simultaneous normal loading and bulk deformation on flat contacts is necessary to validate the contact area development and friction conditions. The contact area development due to bulk strain can be measured with a confocal microscope. The measurement could be done either by an in-situ setup with a glass tool or after experiments by measuring the same area before and after surface deformation.
The friction model can also be checked with FE simulations of simple deep drawing products like U-bend, cup drawing, etc. In a real deep drawing experiment, the effects of friction can be seen on the punch-force displacement characteristics as well as thinning/thickening of sheet materials. These effects can be compared using this advanced friction model and the Coulomb friction model on FE simulations.

d. Effect of sliding

The progression of sliding affects the coefficient of friction. Due to sliding, repeated contact occurs which can cause the surfaces of the sheet material to change continuously. In, Chapter 4, surface deformation of the sheet material is considered with contact pressure and bulk strain. In Chapter 6, it is assumed that elastic recovery will occur for reloading conditions if the contact load does not exceed a previously experienced load. However, the ploughing occurs continuously over the already deformed surface. The development of surface roughness with the sliding cycle is not considered. This causes continuous plastic deformation on the deformed plateaus of the sheet material. This phenomenon can be included by considering the influence of sliding distance on surface deformation.

e. Deterministic characterization of asperities

Severe plastic deformation can occur in deep drawing processes due to bulk strain and high contact pressures near the die/punch rounding regions. This can result in large fractional contact areas ($\alpha > 0.5$) in certain areas of the deep drawing processes (due to high bulk strain, certain regions like die/punch rounding). Under these conditions, the current method to determine and model the contact patches will run in to limits. In such conditions, a single contact patch should be identified by multiple elliptical paraboloids in order to have an accurate representation of the micro-geometry.

APPENDICES

Appendix A

Mixed lubrication model – Flow factor method

To describe the lubrication between the sliding surfaces, the Reynolds equation is used to calculate the flow between them. The Reynolds equation is valid for smooth surfaces. However, the fluid flow occurs between the rough surfaces in lubricated contacts. Patir and Cheng [40] developed a method to correct the flow of the fluid between the rough surfaces by numerical flow simulations. The correction flow factors are separately found for the pressure and velocity driven flows to be used along with the standard Reynolds equation:

$$\frac{\partial}{\partial x}\left(\phi_x \frac{{h_{\text{lub}}}^3}{12\eta_{\text{lub}}}\frac{\partial P_{nom}^{\text{lub}}}{\partial x}\right)=\frac{U_1+U_2}{2}\frac{\partial h_{\text{lub}}}{\partial x}+\frac{U_1+U_2}{2}R_q\frac{\partial \phi_s}{\partial x}+\frac{h_{\text{lub}}}{2}\frac{\partial (U_1+U_2)}{\partial x} \tag{A.1}$$

where, ϕ_x and ϕ_s are the flow factors due to surface roughness on the lubricant flow for Poiseuille and Couette flow. Patir and Cheng's method [40] is suitable only for nominally separated surfaces (i.e. full film lubrication contacts). Wilson and Marsault [33] gave a revised form of Patir and Cheng's flow factors for the high fractional contact such as that occurs in metal forming situations, as given below.
The non-dimensional film thickness is given as

$$H_{\text{lub}} = h_{\text{lub}} / R_q \tag{A.2}$$

If the non-dimensional film thickness is $H_{lub} > 3$, the full film lubrication occurs. When $H_{lub} < 1$, there is not enough lubricant to cause hydrodynamic flow and the tribo-system will operate in BL. In between these limits, the tribo-system will operate in ML.
The threshold film at which the lubricant will be completely trapped in the valleys is given as

$$H_{\text{lub}}^{c} = 3\left(1-\left(\frac{0.4746}{\gamma_{lay}}+1\right)^{-0.25007}\right) \tag{A.3}$$

The flow factor for the pressure driven flow is given as

$$\phi_x = \left(\frac{1}{H_{\text{lub}}}\right)^3\left[a_2\left(H_{\text{lub}}-H_{\text{lub}}^{c}\right)^2+a_3\left(H_{\text{lub}}-H_{\text{lub}}^{c}\right)^3\right] \tag{A.4}$$

where

$$a_2 = 0.051375 \ln^3(9\gamma_{lay}) - 0.0071901 \ln^4(9\gamma_{lay}) \quad \text{(A.5)}$$

$$a_3 = 1.0019 - 0.17927 \ln \gamma_{lay} + 0.047583 \ln^2 \gamma_{lay} - 0.016417 \ln^3 \gamma_{lay} \quad \text{(A.6)}$$

The flow factor for the velocity driven flow is given as

$$\phi_s = b_0 + b_1 H_{\text{lub}} + b_2 H_{\text{lub}}{}^2 + b_3 H_{\text{lub}}{}^3 + b_4 H_{\text{lub}}{}^4 + b_5 H_{\text{lub}}{}^5 \quad \text{(A.7)}$$

where

$$b_0 = 0.12667 \gamma_{lay}{}^{-0.6508} \quad \text{(A.8)}$$

$$b_1 = \exp\left(-0.38768 - 0.44160 \ln \gamma_{lay} - 0.12679 \ln^2 \gamma_{lay} + 0.042414 \ln^3 \gamma_{lay}\right) \quad \text{(A.9)}$$

$$b_2 = -\exp\left(-1.1748 - 0.39916 \ln \gamma_{lay} - 0.11041 \ln^2 \gamma_{lay} + 0.031775 \ln^3 \gamma_{lay}\right) \quad \text{(A.10)}$$

$$b_3 = \exp\left(-2.8843 - 0.36712 \ln \gamma_{lay} - 0.10676 \ln^2 \gamma_{lay} + 0.028039 \ln^3 \gamma_{lay}\right) \quad \text{(A.11)}$$

$$b_4 = -4.706e^{-3} + 1.4493e^{-3} \ln \gamma_{lay} + 3.3124e^{-4} \ln^2 \gamma_{lay} - 1.7417e^{-4} \ln^3 \gamma_{lay} \quad \text{(A.12)}$$

$$b_5 = 1.4734e^{-4} - 4.255e^{-5} \ln \gamma_{lay} - 1.057e^{-5} \ln^2 \gamma_{lay} + 5.0292e-6 \ln^3 \gamma_{lay} \quad \text{(A.13)}$$

Appendix B

Surface roughening

Roughening occurs in deep drawing processes due to bulk strain. The straining of the sheet material leads to grain rotations on the surface, resulting in surface roughening. The magnitude of surface roughening is affected by the bulk strain on the surface. The free surface tends to roughen more than the constrained surface. A simple model has been developed under free surface conditions based on the geometrics with the volume conservation as shown in Figure B.1. The surface deformation in a bulk deformation process is characterized by two stages depending on the strain. The grains deform at low strains and hence the smoothening of the surface takes place during the first stage. When the strain increases, the critical shear strength between the grains is reached and the grain starts to rotate. The grain rotation causes the surface to roughen. Here, the surface is represented by the assumed geometry of the grain as shown in the figure.

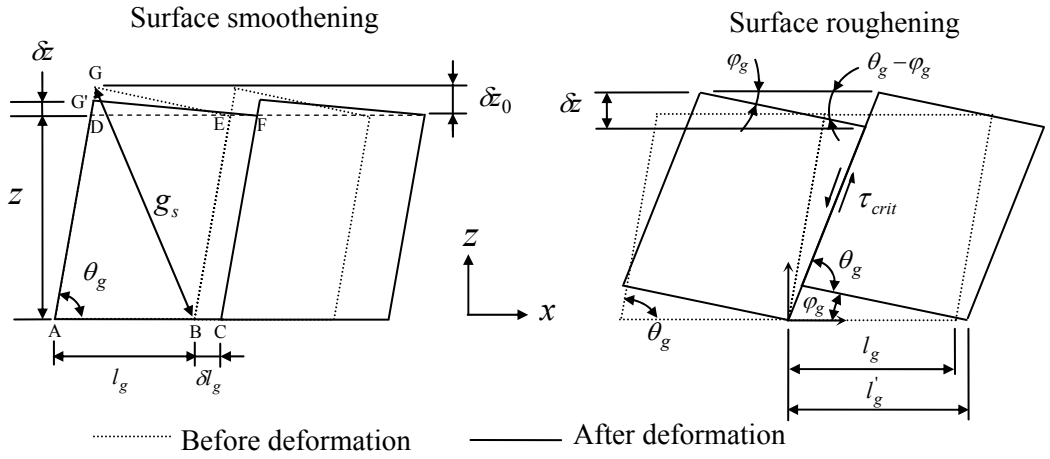

Figure B**.1:** Surface smoothening and roughening process due to bulk strain.

The grain is characterised by the grain size, g_s, and the grain orientation, θ_g. The height of the grain in the z-direction is given as

$$z = g_s \sin(\theta_g / 2) \tag{B.1}$$

The length of the grain in x-direction is given as

$$l_g = z\left(\frac{1}{\tan\theta_g} + \frac{1}{\tan\theta_g/2}\right) \tag{B.2}$$

The surface roughness, R_a is the arithmetic average of the peaks and the valleys of the surface. The initial roughness of the surface is obtained as

$$R_a = \delta z_0 / 2 \tag{B.3}$$

During deformation, the grain deforms to the applied strain and the volume is conserved. From this assumption, the change in the height of the grain can be calculated from the geometry. From the volume conservation,

Area of ΔGDE = Area of Δ G'DF – Area of □ BCEF (B.4)

$$\frac{1}{2}\left(l_g + \delta l_g\right)\delta z = \frac{1}{2} l \delta z_0 - z \delta l_g \tag{B.5}$$

$$\delta z = \frac{l_g \delta z_0 - 2 z \delta l_g}{\left(l_g + \delta l_g\right)} \tag{B.6}$$

The surface roughness at smoothening stage is given by

$$R_a = \frac{\delta z}{2} = \frac{l_g \delta z_0 - 2 z \delta l_g}{2\left(l_g + \delta l_g\right)} \tag{B.7}$$

During roughening, the grains will rotate along the grain boundary. The applied strain during rotation is calculated as

$$\varepsilon = \ln \frac{l_g'}{l_g} \tag{B.8}$$

$$\varepsilon = \ln\left(\frac{\sin\theta_g}{\sin\left(\theta_g - \varphi_g\right)}\right) \tag{B.9}$$

The change in the height difference between the peak and valley is given as

$$\delta z = l_g \sin\varphi_g \tag{B.10}$$

The change in roughness after grain rotation is calculated from equations (B.9) and (B.10):

$$R_a = \frac{\delta z}{2} = \frac{l_g \sin\left(\theta_g - \sin^{-1}\left(\frac{\sin\theta_g}{e^{\varepsilon}}\right)\right)}{2} \tag{B.11}$$

Appendix C

In this appendix, the surface topography of the DC06 sheet material and tool are given.

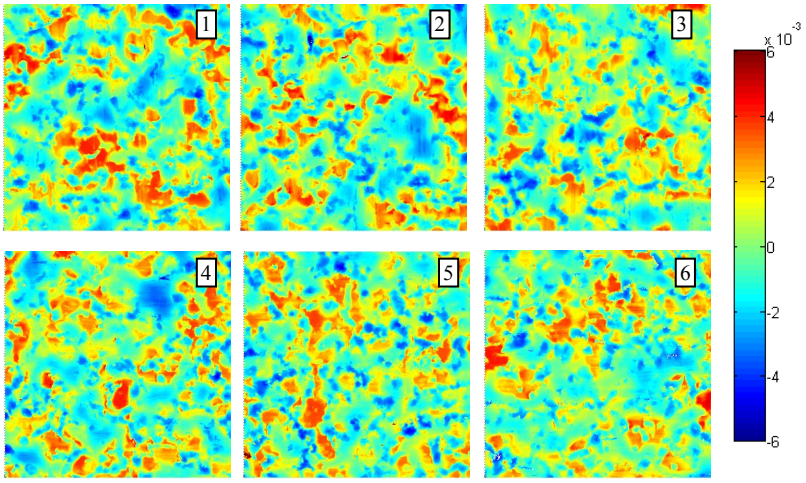

Surface roughness, S_q=1.7µm All surfaces are 1x1 mm^2

Figure C.1: Surface topography of DC06 sheet material measured at different spots with a confocal microscope.

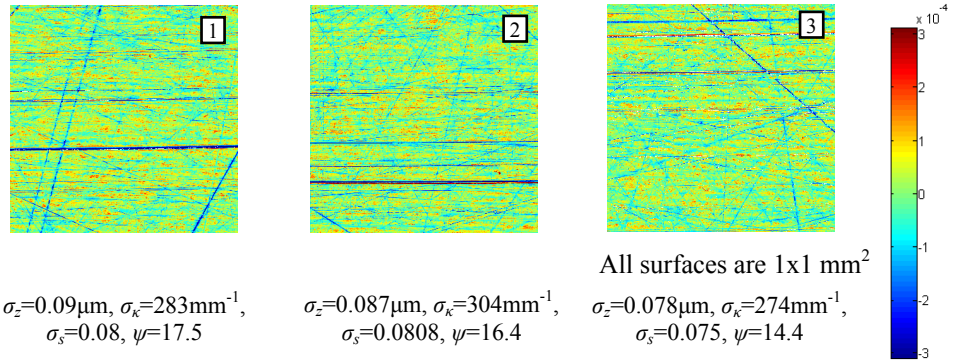

All surfaces are 1x1 mm^2

σ_z=0.09µm, σ_κ=283mm^{-1}, σ_s=0.08, ψ=17.5

σ_z=0.087µm, σ_κ=304mm^{-1}, σ_s=0.0808, ψ=16.4

σ_z=0.078µm, σ_κ=274mm^{-1}, σ_s=0.075, ψ=14.4

(See Equations C.1-C.9 for the definitions of surface properties)

Figure C.2: Surface topography of tool surfaces measured with a confocal microscope.

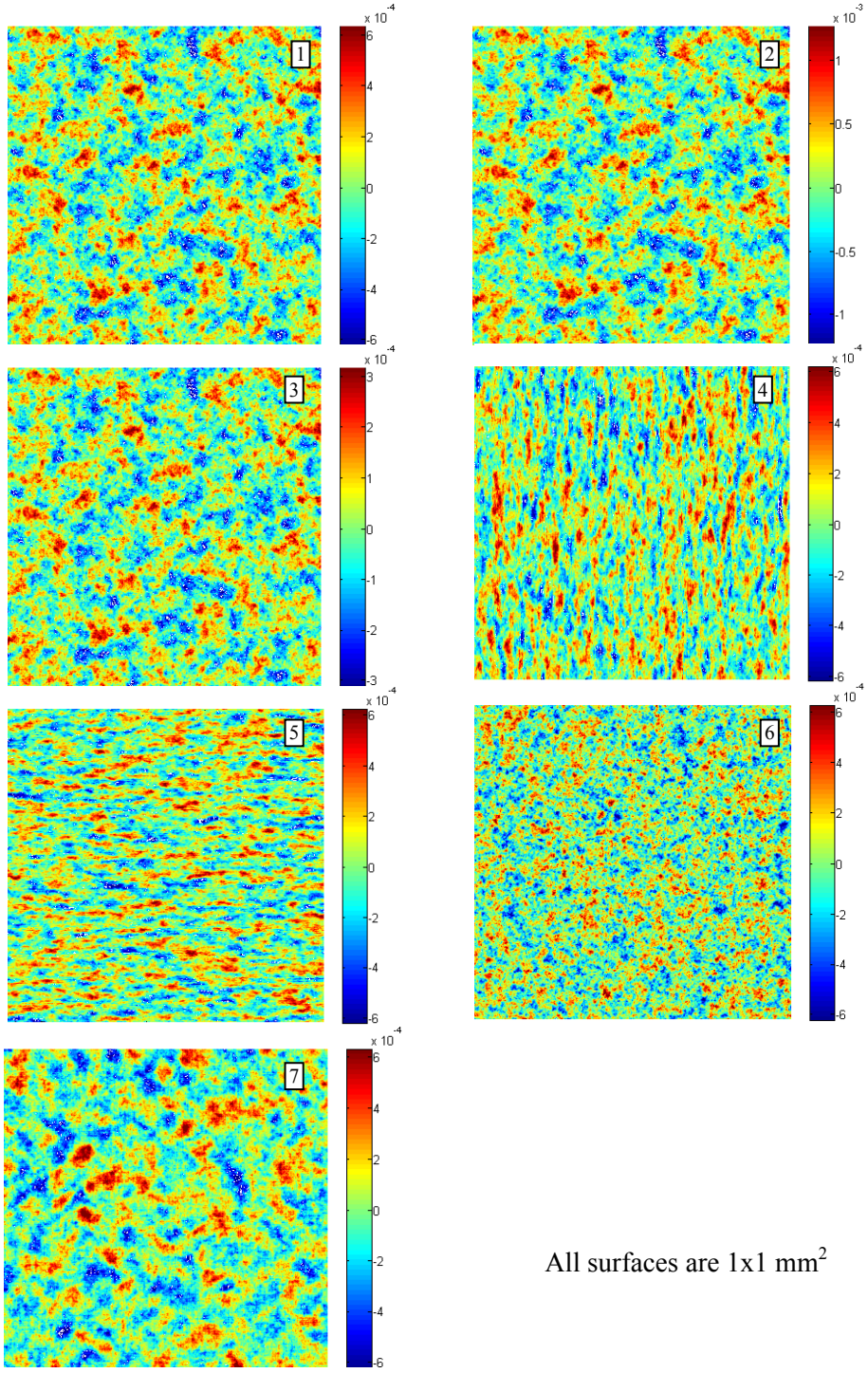

Figure C.3: Numerically generated rough surfaces using the technique of Hu and Tonder [65].

Surface roughness parameters

A surface is composed of asperities of height z, and N is the total number of measurement heights/pixels. The pixel sizes in the x and y directions of the surface are respectively p_x and p_y. In the statistical approach, the summits are typically found by the height of a measurement point with the neighbouring summits. When the neighbouring asperities are lower than the point of interest, then it is termed as summit. A three-point rule (in case of line profile), five-point or nine-point rule (in case of surface profile) can be used to identify

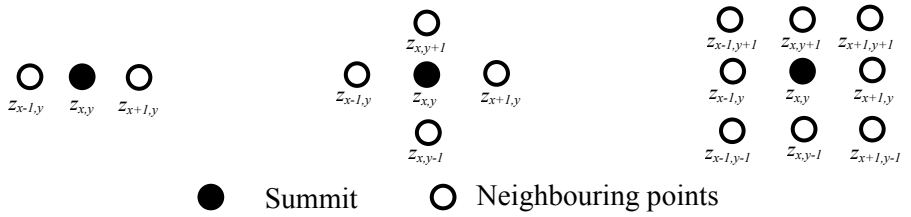

(a) Three point summit rule (b) Five point summit rule (c) Nine point summit rule

Figure C.4: Identification of summits in statistical approach.

the summits as shown in Figure C.4.
The standard deviation of the surface heights is given as

$$\sigma_z = \sqrt{\frac{1}{N}\sum_{i=1}^{N} z(i)^2} \qquad (\mathbf{C}.1)$$

The slope of the summit/asperity of the given surface can be found from the height data of the neighbouring asperities using the finite difference method. The slope of the summit/asperity at the position (x,y) in both directions is given as

$$s_x = \left|\frac{z(x,y) - z(x+1,y)}{p_x}\right|;\ s_y = \left|\frac{z(x,y) - z(x,y+1)}{p_y}\right| \qquad (\mathbf{C}.2)$$

The equivalent slope of a summit/asperity is given as,

$$s = \frac{s_x + s_y}{2} \qquad (\mathbf{C}.3)$$

If n is the total number of summits/asperities, the standard deviation of the slopes is given as

$$\sigma_s = \sqrt{\frac{1}{n}\sum_{i=1}^{n} s(i)^2} \qquad (\mathbf{C}.4)$$

The curvature of the summit/asperity at the position (x,y) of the given surface is found as

$$\kappa_x = \left| \frac{z(x-1,y) - 2z(x,y) + z(x+1,y)}{{p_x}^2} \right|; \quad \kappa_y = \left| \frac{z(x,y-1) - 2z(x,y) + z(x,y+1)}{{p_y}^2} \right| \qquad (\mathbf{C}.5)$$

The equivalent curvature of a summit/asperity is given as

$$\kappa = \frac{\kappa_x + \kappa_y}{2} \qquad (\mathbf{C}.6)$$

The summit radius, R is found by calculating the local curvature in both directions using a finite difference approximation from the surface height data as given below.

$$R = \left[\frac{\kappa_x + \kappa_y}{2} \right]^{-1} \qquad (\mathbf{C}.7)$$

If n is the total number of summits/asperities, the standard deviation of the curvatures is given as

$$\sigma_\kappa = \sqrt{\frac{1}{n} \sum_{i=1}^{n} \kappa(i)^2} \qquad (\mathbf{C}.8)$$

The auto-correlation length of the surface profile with N number of heights is

$$ACF = \frac{\sum_{x=1}^{N} z(x) z(x+1)}{N} \qquad (\mathbf{C}.9)$$

The bandwidth parameter of the surface from the power spectral density of the surface is given as

$$\psi = \left(\frac{\sigma_z \sigma_\kappa}{{\sigma_s}^2} \right)^2 \qquad (\mathbf{C}.10)$$

The surface roughness lay gives the orientation of the asperities with respect to the sliding direction. The surface lay parameter, γ_{lay} is calculated from the auto-correlation length in both x and y directions as

$$\gamma_{lay} = ACF_x / ACF_y \qquad (\mathbf{C}.11)$$

Appendix D

Hertz contact theory and BEM validation

Line contact

Consider a cylinder is in contact with a flat plate as shown in Figure D.1. Hertz considered the contact between two smooth cylinders in contact with the assumptions as follows,

- Surface deforms elastically.
- Cylinder in contact with the flat surface is smooth.
- Contact area and width are smaller than the actual dimensions of the cylinders.

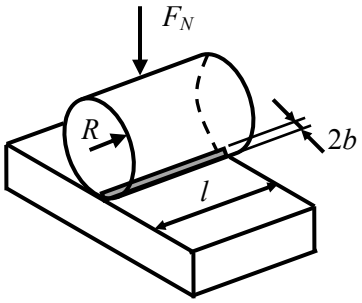

b	Half width of the contact
l	Length of the contact
R	Radius of the cylinder
F_N	Applied normal load
E_1, E_2	Elastic modulus of cylinder and flat surface
υ_1, υ_2	Poisson's ratio of cylinder and flat surface

Figure D.1: Line contact between a cylinder and flat surface.

According to the Hertz contact theory of elastic solids, the half contact width is given as,

$$b = 2\sqrt{\frac{2F_N}{\pi E^* l}} \text{ , where } E^* = \left(\frac{E_1}{1-\nu_1{}^2} + \frac{E_2}{1-\nu_2{}^2} \right) \tag{D.14}$$

The mean and maximum contact pressure is given as

$$P_m = \frac{F_N}{A} = \frac{F_N}{2bl} \; ; \; P_{\max} = \frac{4}{\pi} P_m \tag{D.15}$$

Boundary Element Method (BEM)

The boundary element method (BEM) [22] employs a discretization scheme of the surface (boundary) into elements to calculate the surface deformation. BEM offers reduced dimensionality of the problem and computational effort when compared with the finite elements since it discretizes only the boundary and not the whole volume. Boundary integral formulation of the problem is solved by converting it into algebraic equations. BEM discretizes the surface into a uniformly sized array of elements. The patches which are in contact are assumed to have a uniformly distributed pressure over the element. From the direct formulation of the boundary elements using the equilibrium conditions and stress-strain relations, a solution is found for the given initial and boundary conditions by a

suitable convergence method. Elastic displacements of the surface are calculated according to Love [92]. When the stresses exceed the Von Mises yield criterion, the plasticity deformation of the contact patches occur. The validation of the BEM is done to verify with the analytical contact models for the elastic contact. The smooth cylinder (no surface roughness) of different radii is used to calculate the mean contact pressure and real contact area. The results are compared with the Hertz contact theory. BEM agrees well with the Hertz line contact model for the given load and geometry of the cylinder, as shown in Figure D.2.

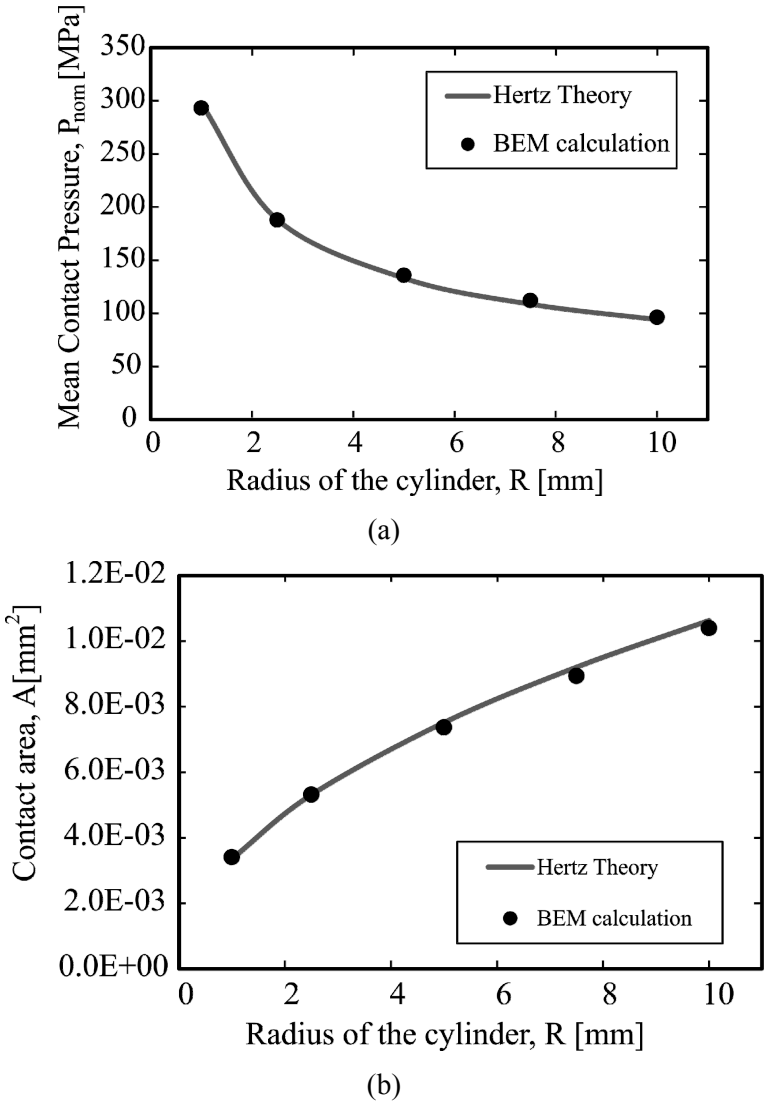

Figure D.2: Comparison of BEM calculations with Hertz contact theory for a smooth cylinder on the rigid flat surface for (a) Mean contact pressure and (b) Contact area.

Appendix E

In this appendix, the algorithm for the mixed lubrication model is presented.

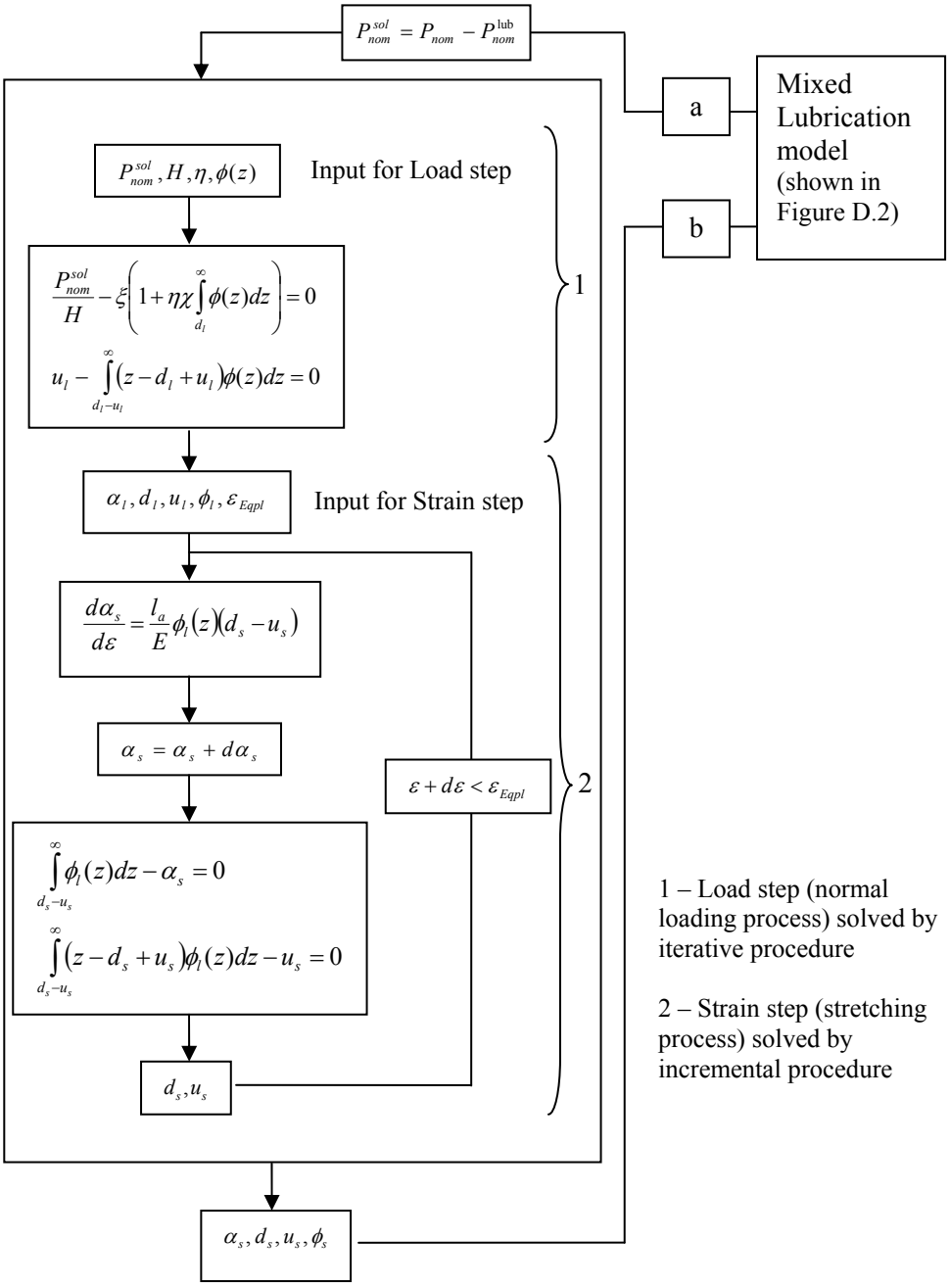

Figure E**.1:** Asperity flattening model.

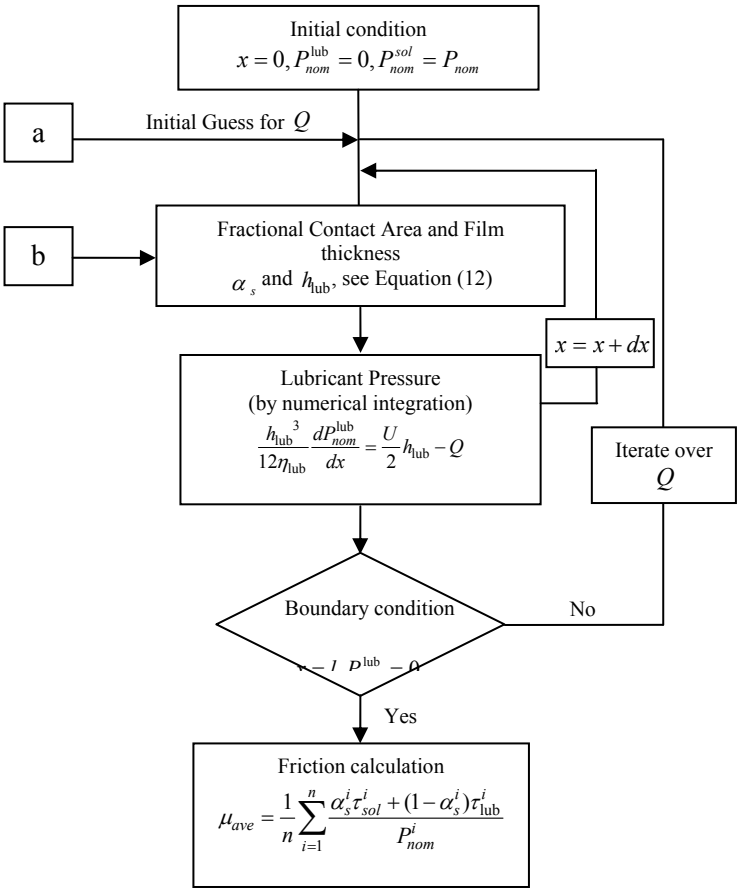

Figure E.**2:** Mixed lubrication model.

Expressions for the parameters used in the asperity deformation model of Westeneng [18].

$$\xi = \left(\int_{d_l - u_l}^{d_l} (z + u_l - d_l)\phi(z)dz + \int_{d_l}^{\infty} (z - d_l)\phi(z)dz \right) \cdot \frac{\left(\int_{d_l - u_l}^{d_l} (z + u_l - d_l)\phi(z)dz + \int_{d_l}^{\infty} (z - d_l)\phi(z)dz \right)}{\left(\int_{d_l - u_l}^{d_l} (z + u_l - d_l)^2 \phi(z)dz + \int_{d_l}^{\infty} (z - d_l)^2 \phi(z)dz \right)} \quad \text{(E.1)}$$

$$\chi = \frac{\int_{d_l}^{\infty} (z - d_l)\phi(z)dz}{\int_{d_l}^{\infty} \phi(z)dz \cdot \left(\int_{d_l - u_l}^{d_l} (z + u_l - d_l)\phi(z)dz + \int_{d_l}^{\infty} (z - d_l)\phi(z)dz \right)} \quad \text{(E.2)}$$

Table of input parameters for the model.

Parameters	Values
Sliding Velocity, U [mm/s]	0.1 - 100
Contact length, l [mm]	80
Lubricant Viscosity, η_{lub} [Pas]	0.06
Strain, ε [-]	0 ~ 0.1, 0.3*
Nominal Pressure, P_{nom} [MPa]	10, 50
	* Increasing linearly from X = *0~l*

Table E**.1:** Input parameters for the ML model.

Parameters	Values
Workpiece Hardness, H [MPa]	1400
Persistence parameter, η [-]	1
Density of tool asperities, ρ [mm^{-2}]	$2 \cdot 10^3$
Mean Radius of tool asperities, R [μm]	0.2

Table E**.2:** Input parameters for the asperity deformation model.

Appendix F

In this appendix, the algorithm for the friction model is given.

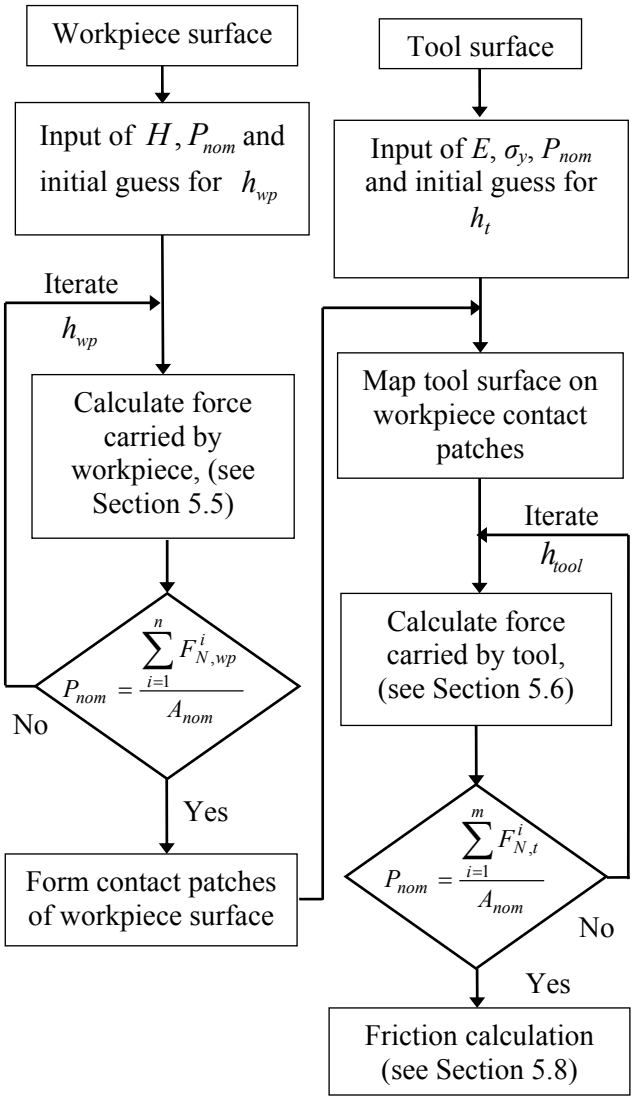

Figure F.1: Flowchart for the friction model.

Parameters	Values
Elastic modulus, E [GPa]	210
Hardness, H [MPa]	450
Yield strength, σ_y [MPa]	160
Poisson's ratio, υ [-]	0.3

Table F.1: Input parameters for the asperity deformation model.

REFERENCES

[1] ter Haar, R. (1996), Friction in sheet metal forming, the influence of (local) contact conditions and deformation, PhD thesis, University of Twente, The Netherlands, ISBN: 90-900-9296-X.

[2] Emmens, W.C. (1997), Tribology of Flat contact and its application in deep drawing, PhD thesis, University of Twente, The Netherlands, ISBN: 90-365-1028-7.

[3] Wilson, W.R.D. (1991), Friction models for metal forming in the boundary lubrication regime, Journal of Engineering Materials and Technology, 113 (1), 60-68.

[4] Oliveira, M.C., Alves, J.L. and Menezes, L.F. (2008), Algorithms and strategies for treatment of large deformation frictional contact in the numerical simulation of deep drawing process, Archives of Computational Methods in Engineering, 15, 113-162.

[5] Czichos, H. (1978), Tribology: a systems approach to the science and technology of friction, lubrication and wear, Series I, Elsevier Scientific Publishing company, The Netherlands, ISBN: 0-444-41677-5.

[6] Hertz, H. (1882), Über die Berühring fester elastischer Körper, Journal für die Reine und Angewandte Mathematik, 92, 156-171.

[7] Schey, J.A. (1983), Tribology in Metalworking – Friction, Lubrication and Wear, ASM, Metal parks, Ohio, US, ISBN: 0-87-170155-3.

[8] Bowden, F.P. and Tabor, D. (1954), The friction and lubrication of solids, Oxford University press, UK, ISBN: 0-19-850777-1.

[9] Johnson, K.L., Kendall, K. and Roberts, A.D. (1971), Surface energy and the contact of elastic solids, Proceedings of Royal Society, London Series A, 324, 301-313.

[10] Challen, J. and Oxley, P. (1979), An explanation of the different regimes of friction and wear using asperity deformation models, Wear 53, 229–243.

[11] Stribeck, R. (1902), Die wesentlichen Eigenschaften der Gleit und Rollenlager, Zeitschrift des Vereins Deutscher Ingenieure, 46(36,38),1432-1438.

[12] Hersey, M.D. (1966), Theory and Research in Lubrication: Foundation for future developments,John Wiley and Sons, New York, ISBN: 0-47-137346-X.

[13] Greenwood, J.A. and Williamson, J.B.P. (1966), Contact of nominally flat surfaces, Proceedings of the Royal Society of London, Series A, Mathematical and Physical sciences, 295, 300–319.

[14] Halling, J., Arnell, R. D. and Nuri, K. A. (1988), The elastic-plastic contact of rough surfaces and its relevance in the study of wear, Proceeding of the Institution of Mechanical engineers, Part C: Journal of Mechanical engineering science, 202 (4), 269-274.

[15] Pullen, J. and Williamson, J.B.P. (1972), On the plastic contact of rough surfaces, Proceedings of the Royal Society of London, Series A, Mathematical and Physical sciences, 327, 159–173.

[16] Chang, W.R., Etsion I. and Bogy, D.B. (1988), Static friction coefficient model for metallic rough surfaces, Journal of Tribology, 110, 57-63.
[17] Halling, J. and Nuri, K. (1991), Elastic-plastic contact of rough surfaces considering ellipsoidal asperities of work hardening multi-phase materials, Tribology International, 24 (5), 311-319.
[18] Westeneng, A. (2001), Modelling of contact and friction in deep drawing processes, PhD thesis, University of Twente, The Netherlands, ISBN: 90-365-1549-1.
[19] Masen, M.A. (2004), Abrasive tool wear in metal forming processes, PhD thesis, University of Twente, The Netherlands, ISBN: 90-365-2061-4.
[20] Jamari, (2006), Running-in of rolling contacts, PhD thesis, University of Twente, The Netherlands, ISBN: 90-365-2314-1.
[21] Ma, X. (2011), Surface quality of aluminium extrusion products, PhD thesis, University of Twente, The Netherlands, ISBN: 978-90-77172-72-8.
[22] de Rooij, M.B. (2011), Handout Solids and surfaces, University of Twente, The Netherlands, Version 1.4 (2010-2011).
[23] Johnson, K.L. (1985), Contact mechanics, Cambridge University press, UK, ISBN: 0-521-34796-3.
[24] Wilson, W.R.D. and Sheu, S. (1988), Real area of contact and boundary friction in metal forming, International Journal of Mechanical science, 30 (7), 475-489.
[25] Sutcliffe, M.P.F., (1988), Surface asperity deformation in metal forming processes, International Journal of Mechanical science, 30 (11), 847-868.
[26] Timsit, R.S. and Pelow, C.V. (1992), Shear strength and tribological properties of stearic acid films –Part II On Gold coated glass, Journal of Tribology, 114, 159-166.
[27] Akhmatov, A.S. (1966), Molecular physics of boundary friction, Israel program for Scientic transactions.
[28] Blok, H. (1970), The postulate about the constancy of scoring temperature, Interdisciplinary approach to the lubrication of concentrated contacts, NASA sp-237, Washington D.C.
[29] Hamrock, B.J., Schmid S.R., and Jacobson B.O. (2004), Fundamentals of fluid film lubrication, Second edition, Marcel Dekker Inc., USA, ISBN: 0-82-475371-2.
[30] Sheu, S. and Wilson, W.R.D. (1994), Mixed lubrication of strip rolling, ASLE transactions, 37 (3), 483-493.
[31] Wilson, W.R.D. and Walowit, J.A. (1971), An isothermal hydrodynamic lubrication theory of strip rolling with front and back tension, Proceedings of Tribology Convention, Mechanical engineering publications, London, 169-172.
[32] Wilson, W.R.D. and Chang, D. (1996), Low speed mixed lubrication of bulk metal forming process, Journal of Tribology, Transactions of the ASME, 118, 83-89.
[33] Wilson, W.R.D. and Marsault, N. (1998), Partial hydrodynamic lubrication with large fractional contact area, Journal of Tribology, Transaction of the ASME, 120 (1), 16-20.
[34] Le, H.R. and Sutcliffe, M.P.F. (2006), A multi-scale model for friction in cold rolling of aluminium alloy, Tribology Letters, 22 (1), 95-104.
[35] Lo, S.W. and Yang, T.S. (2006), A microwedge model of sliding contact in boundary/mixed lubrication, Wear, 261, 1163-1173.
[36] Hersey, M.D., (1914), The laws of lubrication of horizontal journal bearings, Journal of Washington academy of sciences, 4,542-552.

[37] Schipper, D.J. (1988), Transitions in the lubrication of concentrated contacts, PhD thesis, University of Twente, The Netherlands, ISBN: 90-900-2448-4.
[38] Johnson, K.L., Greenwood, J.A. and Poon, S.Y. (1972), A simple theory of asperity contact in elastohydrodynamic lubrication, Wear, 19, 91-108.
[39] Christensen, H. (1969), Stochastic models for hydrodynamic lubrication of rough surfaces, Proceedings of the Institution of Mechanical Engineers, 184, 1013-1026.
[40] Patir, N. and Cheng, H.S (1978), An average flow model for determining effects of three-dimensional roughness on partial hydrodynamic lubrication, Journal of Lubrication technology, 100, 12-17.
[41] Ahmed, R. and Sutcliffe, M.P.F (2001), An experimental investigation of surface pit evolution during cold-rolling of stainless steel strip, Journal of Tribology, Transactions of the ASME, 123(1), 1-7.
[42] Helenon, F. Vidal Salle, E. and Boyer, J.C. (2004), Lubricant flow between rough surface during closed-die forming, Journal of materials processing technology, 153 (1-3), 707-713.
[43] Klimczak, T. and Jonasson, M. (1994), Analysis of real contact area and change of surface texture on deep drawn steel sheets, Wear, 179, 129-135.
[44] Roizard, X., Raharijaona, J., von Stebut J. and Belliard, P. (1999), Influence of sliding direction and sliding speed on the micro-hydrodynamic lubrication of aluminium mill-finish sheets, Tribology International, 32, 739-747.
[45] Lo, S.W., Zhou, B.Q., Fang, C.F. and Lu, Y.S. (2004), In-situ observation of microwedge effect on liquid lubrication, Journal of Tribology, Transaction of ASME, 126 (4),690-696.
[46] Wihlborg, A. and Gunnarsson, L. (2000), A friction study of uncoated EBT steel sheets in a bending under friction test, Wear, 237 (1), 129-136.
[47] Hokkirigawa, K. and Kato, K. (1988), An Experimental and Theoretical Investigation of Ploughing, Cutting and Wedge Formation During Abrasive Wear, Tribology International, 21, 51-57.
[48] Kienzle, O. and Mietzner, K. (1967), Atlas Umformter Metallischer Oberflachen, Springer-Verlag, Berlin.
[49] Osakada, K. and Oyane, M. (1971), On the roughening of free surfaces in deformation processes, Bulletin JSME, 14 (68), 171-177.
[50] Atala, H.F. and Rowe, G.W. (1975), Surface roughness changes during rolling, Wear, 32, 249-268
[51] Thomson, P.F. and Nayak, P.U. (1979), The effect of plastic deformation on the roughening of free surfaces of sheet metal, International Journal of Machine Tool and Design and Research, 20 (1), 73-86.
[52] Guangnan, C., Huan, S., Shiguang, H. and Baudelet, B. (1990), Roughening of the free surfaces of metallic sheets during stretch forming, Materials science and engineering, Series A, 128 (1), 33-38.
[53] Lubbinge, H., ter Haar, R. and Schipper, D. J. (1996), The Influence of Plastic Bulk deformation on Surface Roughness and Frictional Behavior during Deep Drawing Processes, Tribology Series, 31, 705-711.
[54] Wichern, C.M, De Cooman B.C. and Van Tyne C.J. (2004), Surface roughness changes on a hot dipped galvanized sheet steel during deformation at low strain levels, Acta Materialia, 52 (5), 1211-1222.

[55] Wichern, C.M., De Cooman B.C. and Van Tyne C.J. (2005), Surface roughness changes on a hot dipped galvanized sheet steel as a function of deformation mode, Journal of Materials Processing Technology, 160 (3), 278-288.
[56] Lee, W. (1996), Surface Roughening in Metal Forming Processes, PhD Thesis, Northwestern University.
[57] Hardy, W. and Doubleday, I. (1922), Boundary lubrication – The Paraffin series, Proceedings of Royal society, London, Series A (102), 550-574.
[58] Langmuir, I. (1920), The mechanism of the surface phenomena of flotation, Transactions of the Faraday society, 15, 62-74.
[59] Bowden, F.P. and Leben, L. (1940), The friction of lubricated metal, Philosophical transactions of the Royal Society of London, 239, 1-27.
[60] Briscoe, B.J. and Evans, D.C.B. (1982), The shear properties of Langmuir-Blodgett layers, Proceedings of the Royal society of London, Series A(333), 99-114.
[61] Timsit, R.S. and Pelow, C.V. (1992), Shear strength and tribological properties of Stearic acid films (Part I) on glass and aluminium-coated glass, Journal of Tribology 114, 150-158.
[62] Briscoe, B.J. Scruton, B. and Willis, F.R. (1973), The shear strength of thin films, Proceeding of Royal society of London, Series A (333), 99-114.
[63] Briscoe, B.J. and Tabor, D. (1978), Shear properties of thin polymeric films, Journal of adhesion, 9, 145-155.
[64] Briscoe, B.J., and Tabor, D. (1973), Rheology of thin organic films, ASLE transactions, 17 (3), 158-165.
[65] Hu, Y.Z. and Tonder, K., (1992), Simulation of 3-D Random Rough Surface by 2-D Digital Filter and Fourier Analysis, International Journal of Machine Tools and Manufacture, 32, 83-90.
[66] Ovcharenko, A., Halperin, G. and Etsion, I. (2008), In situ and real time optical investigation of junction growth in spherical elastic-plastic contact, Wear, 264, 1043-1050.
[67] Hol J., Cid Alfaro M.V., de Rooij M.B. and Meinders T., (2012), Advanced friction modelling for sheet metal forming, Wear, 286-287, 66-78.
[68] Sutcliffe M.P.F. (1988), Surface asperity deformation in metal forming processes, International Journal of Mechanical Sciences, 30, 847-868.
[69] Hill, R. (1950), The mathematical theory of plasticity, Clanderon press, Oxford, UK, ISBN: 0-19-850367-9.
[70] Wilson, W.R.D. and Marsault, N. (1998), Partial hydrodynamic lubrication with large fractional contact areas, Journal of Tribology, Transactions of the ASME, 120 (1), 16-20.
[71] Almqvist, A., Fabricius, J., Spencer A. and Wall, P. (2011), Similarities and difference between the flow factor method by Patir and Cheng and Homogenization, Journal of Tribology, 133(3), 031702, 1-5.
[72] Kane, M. and Bou-Said, B. (2004), Comparison of Homogenization and direct techniques for the treatment of roughness in incompressible lubrication, Journal of Tribology, 126 (4), 733-737.
[73] Bayada, G., Ciuperca, I. and Jai, M. (2006), Homogenized elliptic equations and variational with oscillating parameters: Application to the study of thin flow

behaviour with rough surfaces, Nonlinear analysis: Real world applications, 7 (5), 950-966.
[74] Ma, X., de Rooij, M.B. and Schipper, D.J. (2010), A load dependent friction model for fully plastic contact conditions, Wear, 269 (11-12) 790-796.
[75] Masen, M.A., de Rooij, M.B. and Schipper, D.J. (2005), Micro-contact based modelling of abrasive wear, Wear, 258 (1-4), 339-348.
[76] Nayak, P. (1973), Random Process Model of Rough Surfaces in Plastic Contact, Wear, 26, 305–333.
[77] Tabor, D. (1986), Indentation hardness and its measurement: Some cautionary comments, in Microindentation Techniques in Materials Science and Engineering, ASTM STP 889, edited by P.J. Blau and B.R. Lawn (ASTM Press, Philadelphia, PA), 129-159.
[78] Swadener, J.G., George, E.P. and Pharr G.M., (2002), The correlation of the indentation size effect measured with indenters of various shapes, Journal of the Mechanics and Physics of Solids, 50, 681-694.
[79] Gao, X.L. (2006), New expanding cavity model for indentation hardness including strain-hardening and indentation size effects, Journal of Material Research, 21(5), 1317-1326.
[80] Johnson K.L. (1970), The correlation of indentation experiments, Journal of the Mechanics and Physics of Solids, 18 (2), 115-126.
[81] Shankar S. and Mayuram M.M. (2008), A Finite Element Based Study on the Elastic-Plastic Transition Behavior in a Hemisphere in Contact With a Rigid Flat, Journal of Tribology, 130 (044502), 1-6.
[82] Moes, H. (2000), Lubrication and Beyond, University of Twente, The Netherlands, University of Twente Lecture notes code 115531.
[83] Abbott, E.J. and Firestone, F.A. (1933), Specifying surface quality – A method based on accurate measurement and comparison, Mechanical Engineering, 55, 569-572.
[84] Lin, L.P. and Lin, J.F. (2005), An elasto plastic microasperity contact model for metallic materials, Journal of Tribology, 127, 666-672.
[85] Tabor, D. (1951), The Hardness of metals, Oxford University press, UK, ISBN: 0-19-850776-3.
[86] Francis, H.A. (1976), A phenomenological analysis of plastic spherical indentation, Journal of Engineering material technology, 98, 272-281.
[87] Zhao, Y., Maietta, D.M. and Chang, L. (2000), An asperity micro-contact model incorporating the transition from elastic deformation to filly plastic flow, Journal of Tribology, 122 , 86-93.
[88] Oliver, W.C. and Pharr, G.M. (2003), Measurement of hardness and elastic modulus by instrumented indentation: Advances in understanding and refinements to methodology, Journal of Material Research, 19 (1), 3-20.
[89] Oliver, W.C. and Pharr, G.M. (2003), An improved technique for determining hardness and elastic modulus using load and displacement sensing indentation experiments, Journal of Material Research, 7 (6), 1564-1583.
[90] Torrance, A.A., Galligan, J. and Liraut, G. (1997), A model of the friction of a smooth hard surface sliding over a softer one, Wear, 212, 213-230.

[91] Kopalinsky, E.M. and Black, A.J. (1995), Metallic sliding friction under boundary lubricated conditions: Investigation of the influence of lubricant at the start of sliding, Wear, 190, 197-203.

[92] Love, A.E.H. (1929), The stress produced in a semi-infinite solid by pressure on part of the boundary, Philosophical Transactions of Royal Society of London, Series A, London, 228, 377-420.

List of Publications

Journal papers

Karupannasamy, D.K., Hol, J., de Rooij, M.B. Meinders, T. and Schipper, D.J. (2012), Modelling mixed lubrication for deep drawing processes, Wear, 294-295, 296-304.

Karupannasamy, D.K., de Rooij, and Schipper, D.J. (2013), Multi-scale friction modelling for rough contactsunder sliding conditions, Wear, Available online from 14th October 2013, http://dx.doi.org/10.1016/j.wear.2013.09.012.

Karupannasamy, D.K., Hol, J., de Rooij, M.B. Meinders, T. and Schipper, D.J., A friction model for deep drawing processes under loading/reloading conditions, In preparation.

Conference proceedings

Karupannasamy, D.K., de Rooij, M.B. and Schipper, D.J. (2012), Deterministic model for ploughing under rough contacts, Proceedings of NordTrib conference, Trondheim, Norway.

Hol, J., Karupannasamy, D.K. and Meinders, V.T. (2012), Multi-scale friction modeling for manufacturing processes: The boundary layer regime, Procedings of 5th International Conference of Tribology in Materials and Processing, June 4-8, 2012, Notre Dame, US.

Karupannasamy, D.K., de Rooij, M.B. and Schipper, D.J. (2013), Friction modelling for sheet metal forming processes under loading and reloading contact conditions, Proceedings of World Tribology Congress, ISBN: 978-88-90818-50-9, Turin, Italy.